Semicrystalline morphology, intracrystalline chain diffusion and mechanical modulus of selected aliphatic polyesters

Dissertation

zur Erlangung des
Doktorgrades der Naturwissenschaften (Dr. rer. nat.)

der
Naturwissenschaftlichen Fakultät II
Chemie, Physik und Mathematik

der Martin-Luther-Universität
Halle-Wittenberg,

vorgelegt von Herrn

Qiang Yu

Gutachter:

1. Prof. Dr. Thomas Thurn-Albrecht

2. Prof. Dr. René Androsch

3. Prof. Dr. Dario Cavallo

Tag der öffentlichen Verteidigung: 12.02.2025

Contents

Chapter 1

Introduction

Plastic is an indispensable material in modern life. The products made of plastic are nearly everywhere, e.g. smart phones, keyboards, water bottles, plastic bags. In this work, unless otherwise specified, the terms "plastic" and "polymer" are interchangeable. The detailed definition of polymer can be found in Chapter 2. From a great invention facilitating significantly our lives to a material giving rise to significant environmental problems, it took plastic only around 100 years. The "first plastic" (Bakelite) was invented in 1907 by Leo Baekeland [1]. Many commodity plastics, e.g. High Density Polyethylene (HDPE) and Polypropylene (PP) were launched in the 1950s [2, 3]. The production and consumption of plastic began to soar in the 1970s after more and more single-use or disposable articles of plastic were invented, e.g. PET bottles [4] and bags [5] because the material has the advantages of low cost, low density, good deformability and chemical resistance. The service life of disposable articles is rather short [6], it is, then, a challenge for plastic waste management, which does not develop as fast as plastic technology. Even nowadays, a lot of plastic waste is mismanaged, which becomes plastic pollution and appears nearly 'everywhere' as well [7].

This work does not aim to provide solutions to the environmental issues caused by plastic pollution but rather focuses on a material study of a specific type of polymers able to mitigate plastic problems, aliphatic polyesters. Please refer to Chapter 2 for the definition of polyesters and aliphatic polyesters. Before further introducing state of the art related to this work, I want to briefly rationalize how aliphatic polyesters may alleviate the plastic problems.

Currently, plastic is poorly managed at the end of life. According to United Nations Environment Programme (2022), globally, 46 % of plastic goes into landfill (disposing garbage by burying it under soil or earth), 22 % is mismanaged, 17 % is incinerated, and 15 % is collected for recycling, with less than 9 % actually recycled. This implies that only 9% of plastic waste is considered to follow the circular economy. The circular economy is an effort to mimic the loop-closing attributes of nature in anthropogenic systems [8] and is viewed as a sustainable use of plastic. In comparison with products made of commodity plastics, the products made of aliphatic polyesters

provide more options at their end of life for the circular economy [9]. Due to the presence of ester groups along the backbone, aliphatic polyesters can be chemically recycled through not only thermolysis (mainly used for commodity plastic waste) but also solvolysis, which results in high-quality monomers possible for new synthesis of polymers [10]. Similar to chemical recycling, it is also possible to depolymerize aliphatic polyesters by microorganisms and enzymes into monomers [11], which is realized under milder and cleaner conditions. This recycling process is being studied and explored. More practically, aliphatic polyesters can be composted or organic recycled into biomass, CO_2, water, etc., under aerobic conditions, or into biomass, CH_4, CO_2, water, etc., under anaerobic conditions [12]. The emitted CO_2 can be again integrated into aliphatic polyesters through synthesis, as many of them are either fully bio-based or partially bio-based [13]. The emitted CH_4 is burned and converted into energy and CO_2 to close the loop for the circular economy of aliphatic polyesters [14]. In addition, aliphatic polyesters can also reduce slightly the impact of mismanaged plastic waste on our environment due to their biodegradability and non-toxic degradable product [15, 16]. However, the mismanagement of plastic waste should be, in general, avoided or minimized regardless of polymer type. Even if the waste is made of aliphatic polyesters, it does not degrade at all, or does not degrade properly if mismanaged. It can lead to the same environmental consequences as the waste made of commodity plastics, e.g. threatening the local ecological system [17,18], or even extra environmental consequence: fast generation of CH_4 [19]. The gas is more than 28 times as potent as CO_2 at trapping heat in the atmosphere, according to EPA (Environmental Protection Agency). The same is true for landfills, which should be minimized, as they do not follow the circular economy but pose environmental issues [20, 21]. Aliphatic polyesters should not go into landfills, as there is normally no facility next to the sites to collect or burn CH_4, which is generated under anaerobic conditions [22].

Now that aliphatic polyesters show great potential to improve the circular economy of plastic by increasing recycling rates and reducing the amount of waste going to landfills [23, 24], why are aliphatic polyesters, which accounts for less than 1 % of total plastic, according to European Bioplastics Market Data (2017), not yet widely used to replace commodity plastics? There are still many challenges for the replacement of commodity plastics with aliphatic polyesters [14, 25, 26], among which the slightly inferior mechanical properties to those of commodity plastics draw my attention. Aliphatic polyesters normally exhibit deficiencies in the combination of modulus and elongation at break, e.g. HDPE has a higher elongation at break and modulus than PCL (Polycaprolatcone), PP has a similar elongation at break as PBS (Poly Butylene Succinate) but much higher modulus. These mechanical deficiencies lead to hesitation from the industrial perspective [27]. For instance, the industry prefers "drop-in replacement," as it is safe and low cost for the replacement, but it is not possible for aliphatic polyesters due to the deficiency. Different applications, initially covered by HDPE alone, might require different aliphatic polyesters processed differ-

ently in different production lines, if HDPE is partially replaced, which increases the complexity of manufacturing and cost. I was, therefore, motivated by the mechanical difference between aliphatic polyesters and commodity plastics to study two critical factors influencing the mechanical properties (mechanical modulus): semicrystalline morphology and Intra-crystalline Chain Diffusion (ICD). The detailed descriptions of semicrystalline morphology and ICD can be found in Chapter 2.

It is mostly accepted that above the glass transition temperature (T_g), the crystallinity of semicrystalline polymers determines their mechanical modulus [28]. A linear dependence of logarithmic mechanical modulus on crystallinity is often reported [28, 29]. As most studies focus only on one polymer, PE, it is difficult to vary the crystallinity (X_c) independently without changing crystalline layer thickness (d_c), i.e. the higher the crystallinity is, the greater d_c is, and vice versa. Therefore, there were also studies modeling the modulus of semicrystalline polymers by both X_c and d_c as critical parameters [30, 31]. However, Wang and co-workers [32] showed the mechanical modulus is not influenced by d_c, but rather the crystallinity alone. It is also known that the mechanical modulus of semicrystalline polymers is influenced by phase transitions and relaxation processes. The presence or absence of α_c-relaxation due to ICD has a significant influence on the mechanical modulus between T_g and melting temperature (T_m) [33, 34].

In contrast to the question "What determines the mechanical modulus", "What determines the morphology of semicrystalline polymers" is still a long-standing question without consensus [35, 36], although several theoretical models have been proposed. The famous Hoffman and Lauritzen (HL) kinetic model assumed the growth of crystals is controlled by the secondary nucleation rate, the crystal with the highest growth rate (the highest nucleation rate) dominates the morphology (d_c) [37]. Saddler and co-workers developed the kinetic model based on rough growth surfaces and the kinetic restrictions resulting from pinning [38, 39]. Stepanow proposed another kinetic model based on chain dynamics [40]. This model takes crystal thickening into account (the crystal thickening was claimed to have a weak dependence on pressure) while the other two above-mentioned kinetic models do not. In multistage models, it is assumed that the crystal thickness is a result of reorganization processes taking place during or after crystallization. Different processes have been suggested to be responsible for reorganization, namely intracrystalline chain diffusion (ICD) related to an α_c relaxation (in some references, different terms can be found, which also refer to ICD, e.g. chain sliding diffusion) [41–43], size-dependent stability of different crystal phases [44] or a mesophase with lower order [45, 46]. However, all these models do not distinguish between crystal-mobile polymers that have an α_c-relaxation and crystal-fixed polymers that display no α_c-relaxation.

Our group recently proposed that this distinction is essential for the formation of the semicrystalline morphology [47], and showed that the competition between crystal growth and crystal reorganization determines the semicrystalline morphology. Thanks to the quantitative access to the ICD via dedicated solid-state nuclear mag-

netic resonance (NMR) techniques, we were able to quantify this relation and showed that the ratio $\tau_{\mathrm{lc}}/\tau_{\mathrm{c}}$ is the decisive parameter [48]. Here, τ_{lc} is the layer crystallization time, the time during which the crystal grows on average by one molecular layer, as circled in red in Figure 1.1, which is the product of crystal layer thickness (assumed to be around 5Å) and inverse of the growth rate of spherulite (μ) measured by polarized optical microscope (cf. Chapter 3). $\langle\tau_{\mathrm{c}}\rangle$ is the so-called jump correlation time measured by NMR (cf. Chapter 3). Starting from polymers with slow ICD ($\langle\tau_{\mathrm{lc}}\rangle \ll \langle\tau_{\mathrm{c}}\rangle$), over medium ICD ($\langle\tau_{\mathrm{lc}}\rangle \approx \langle\tau_{\mathrm{c}}\rangle$) to fast ICD ($\langle\tau_{\mathrm{lc}}\rangle \gg \langle\tau_{\mathrm{c}}\rangle$), the average crystalline layer thickness (d_{c}) increases. The different regimes also result in different features in the semicrystalline morphology [47].
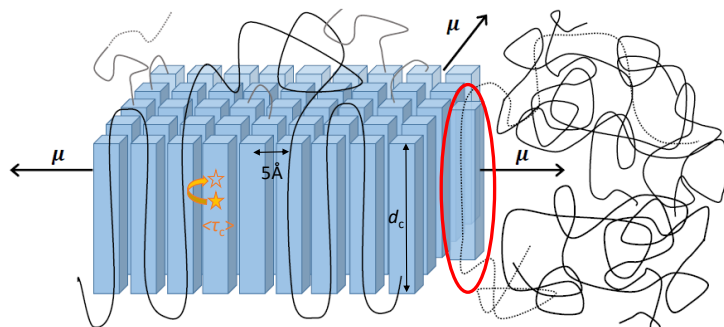
Figure 1.1: Schematic view of the lateral crystal growth of a semicrystalline polymer with the relevant parameters: a growth rate of μ, the helical jump correlation time $\langle\tau_{\mathrm{c}}\rangle$, the crystalline layer thickness d_{c}, the blue columns referring to different crystal layers with spacing of around 5Å. The red circle shows a molecular layer. The figure is adapted from the reference [49].

Crystal-fixed polymers such as PCL (Polycaprolactone) with slow ICD form crystals with a rather uniform crystal thickness, close to the thermodynamic stability limit and a broader distribution for the amorphous-layer thickness. Crystal-mobile polymers, on the other hand, such as PEO (Poly Ethyleneoxide) with fast ICD show a well-defined thickness of the amorphous regions but broadly distributed crystal thicknesses. The morphological difference between the two types of polymers is schematically shown in Chapter 2. These features can be worked out by a quantitative modeling of small-angle X-ray scattering (SAXS) data [47, 50]. However, the generality of our proposals is not yet cross-checked in a broad range of different polymers,

though they work well for three model polymers (PEO, POM (Poly Oxymethylene) and PCL).

Although ICD or α_c-relaxation plays an essential role in the determination of semicrystalline morphology of polymers and their mechanical properties, it is not yet clear what are the molecular criteria for the presence of an α_c-relaxation or if there is any. Gedde suggested that polymers with small or no pendant groups, no layered structure formed due to strong hydrogen bonds, with short repeating units and with weak intermolecular forces are the polymers to have an α_c-relaxation [51]. Hu and Schmidt-Rohr [52] summarized the studies of α_c-relaxation on a few polymers, where it is found the generality of the suggestion by Gedde may not be complete, e.g. iPP (isotactic Polypropylene) has ICD while sPP (syndiotactic Polypropylene) does not. The suggestion by Gedde also indicates that aliphatic polyesters do not have ICD, as their repeating unit can be large and there is the presence of layered crystalline structures [53]. The layers formed because of the gathering of ester groups increase the difficulty of α_c-relaxation as these layers are normal to the c direction (fiber direction) of the crystal unit cell (cf. Chapter 2). Pepels et al. showed that the stacking of the ester groups in the crystal (layered crystalline structure) of aliphatic polyesters plays a more important role than the size of the repeating unit in restricting ICD [54]. When the layered crystalline structures are disturbed, the aliphatic polyester can regain α_c-relaxation, even if the repeating unit is rather large (copolymer of PCL and Polypentadecalactone (PPDL)). Song et al. proposed that the polymer chain conformation in crystals has an influence on ICD [55]. It was concluded that helical chain conformation favors ICD, while a planar chain conformation does not. The conclusion is based on only one pair of polymers (PLLA (Poly-L-Lactic Acid) and PCL).

My literature review of studies of semicrystalline morphology on common aliphatic polyesters shows that only rather few studies of semicrystalline morphology of aliphatic polyesters are reported (cf. Chapter 4), even though some aliphatic polyesters are already commercially available in many applications for more than 20 years. Similarly, studies on ICD of aliphatic polyesters are also rather few (cf. Chapter 4).

Therefore, in this work, I aim to study ICD and semicrystalline morphology of a series of chemically similar polyesters that were selected based on material availability, in order to check the generality of our proposals (the dependence of morphological features on ICD) in aliphatic polyesters, to understand whether there are molecular criteria for the presence of ICD in aliphatic polyesters and to fill the missing studies of semicrystalline morphology and ICD in the field of aliphatic polyesters. In addition, the dependence of the mechanical modulus on semicrystalline morphology and ICD of all investigated aliphatic polyesters will be clarified as well.

The semicrystalline morphology and ICD of a commercially available PBS (Poly Butylene Succinate) were investigated to test if our proposals are valid for aliphatic polyesters. The results are presented in Chapter 5. PBS does not have measurable ICD and shows the typical semicrystalline morphology of crystal-fixed polymers. To

expand the generality of our proposals further, a commercially available P3HB (Poly-3-hydroxybutyrate) was studied, the result is reported in Chapter 6. It turns out that P3HB is another crystal-mobile aliphatic polyester, besides PLLA. Chapter 7 summarizes the studies of the semicrystalline morphology and ICD of a series of selected polyesters with similar chemical structures, which are different from each other only by the number of CH_2 and CH_3 groups in the repeating unit. The results show that all these aliphatic polyesters are crystal-fixed polymers except PLLA and P3HB. The molecular criteria for the presence of α_c-relaxation is proposed. All the aliphatic polyesters studied in the work follow our proposals regarding semicrystalline morphology and ICD without exception.

Chapter 2

Basic concepts

This chapter introduces basic concepts of polyesters and polymer crystallization relevant to this study, which complements Chapter 1 and facilitates the reading for the following chapters. Section 2.1 contains the explanation of aliphatic polyesters, their synthesis and biodegradability. Polymer crystallization is introduced in Section 2.2.

2.1   Aliphatic polyesters

What is a **polymer**? The term polymer refers, by definition, to molecules formed from a number of building blocks, called monomers, usually connected by covalent bonds [56]. **Polyesters** are polymers containing ester groups (Figure 2.1) as major structural components of the main chains of the macromolecules of which the polymer is composed [57]. However, polyesters do not usually refer to polymers that contain ester groups attached to the main chain either directly (e.g. cellulose triacetate, poly(vinyl acetate) or poly(methyl acrylate), or within short side-chains. In this study, I focus only on **aliphatic polyesters**. It is a type of polyesters containing no aromatic moieties (in the traditional sense, 'having a chemistry typified by benzene' according to IUPAC (International Union of Pure and Applied Chemistry)).
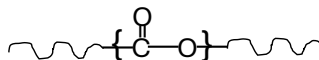

Figure 2.1: Schematic view of an ester group in a polymer chain

In this section, two sorts of common polymerizations used for producing aliphatic

polyesters are introduced (Section 2.1.1) and the biodegradation reaction is briefly mentioned (Section 2.1.2). The books by Scheiers [57] and Koltzenburg [56] and Rieger [58] provide the basis of Section 2.1.

2.1.1   Synthesis

Polycondensation and Ring-Opening Polymerization (ROP) are the most common synthesis routes for the aliphatic polyesters in this study (cf. Chapter 4). Below, two polymerizations are briefly introduced to provide explanations of definition or nomanclatures used in this study.

Polycondensation

Polycondensation is a step-growth polymerization. The polymerization results in new covalent chemical bonds and the elimination of (mostly low-molecular) fragments. In the synthesis of aliphatic polyesters, the polymerization relies on the esterification reaction of diacids and diols or on the esterification of hydroxy-acids (esterification generally refers to the formation of ester as reaction product from two reactants (e.g. diol and diacids)) to form new covalent chemical bonds. During polymerization, water molecules, as fragments, are eliminated. Therefore, the reaction requires that the monomers possess diacid and diols groups or hydroxyl and acid groups are united in the same monomer. The monomers containing diacid and diols are referred to as AA and BB monomers. The corresponding polyesters synthesized based on AA and BB monomers are called AA-BB polyesters. The monomers having both acid and hydroxyl groups are referred as to A-B monomers. A-B monomers (lactone belongs to this group as well) are the building blocks of A-B polyesters.
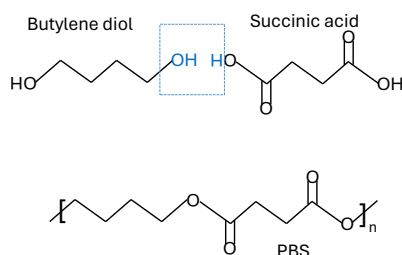
Figure 2.2: Chemical structures of butylene diol (AA monomer), succinic acid (BB monomer) and polybutylene succinate (AA-BB polyester). The blue box indicates an elimination of a water molecule.

Figure 2.2 shows the chemical structure of a typical AA-BB polyester, Polybutylene Succinate (PBS), and its AA and BB monomers. PBS is synthesized by a polycondensation reaction (cf. Chapter 4). Although the polymerization is relatively easy to take place and each monomer has the same reactivity, it has limitations regarding

the degree of polymerization. PBS with a high-molar mass can only be achieved at very high conversions. Here is a brief introduction of molar mass used in the field of polymers. Unlike small molecules, which can be characterized by a particular molar mass, the molar mass or molecular weight of a polymer has a distribution. The molar mass of a polymer can only be defined by an average value, which can be normally calculated in several different ways. M_n and M_w represent two commonly used average values, they are number average molecular weight and mass average molecular weight, as defined by the following equations

$$M_n = \frac{\sum n_i \cdot M_i}{\sum n_i}, \ M_w = \frac{\sum n_i \cdot M_i^2}{\sum n_i \cdot M_i} \tag{2.1}$$

where n_i is the number or amount of the molecules that have a molar mass M_i. The ratio of M_w to M_n is called the Poly Dispersity Index (PDI), which is commonly used to characterize the distribution width of the molar mass of a polymer sample. The greater PDI is, the broader the distribution width of molar mass is, and vice versa. The large-scale production of PBS is based on a slightly modified version of polycondensation and with efficient techniques to remove the fragments. Another limitation is that a polycondensation reaction normally results in large PDI. The lowest PDI is 2 only from ideal polycondensation polymerization. Therefore, using this polymerization to produce high-molecular-weight and low-PDI polyesters is still challenging. This difficulty can be solved by ring-opening polymerization.

Ring-opening polymerization

As indicated by the name of the polymerization, a general feature of ROP is that the monomers are rings of varying size. There is release of ring strain and enthalpy after the rings are open during polymerization, which are the main driving forces for this type of polymerization. In contrast to polycondensation, ROP is an addition polymerization, which does not eliminate low-molecular fragments. In the synthesis of aliphatic polyesters, the rings are normally lactones. As shown in Figure 2.3 (a), valerolactone (the ring) is an ester formed by internal esterification of carboxylic acid and hydroxyl groups in the same monomer. Therefore, lactone is an AB monomer. Depending on a different mechanism, ROP can be further divided into different ring-opening polymerization, e.g. free radical, cationic and anionic polymerization. For details, please see the reference [56]. PVL can be polymerized by cationic and anionic ROP. Figure 2.3 (b) shows schematically a cationic polymerization of PVL as an example. Compared with polycondensation, ROP, regardless of which type, is more complicated, as it has more steps during polymerization, e.g. initiation, chain growth and chain transfer. However, it is much easier for ROP to produce high molar mass polyesters. The living character of the ROP of lactones can lead to lower PDI than polycondensation [58]. Please refer to Chapter 4 for detailed references of the polymerization methods of each aliphatic polyester investigated in this study.
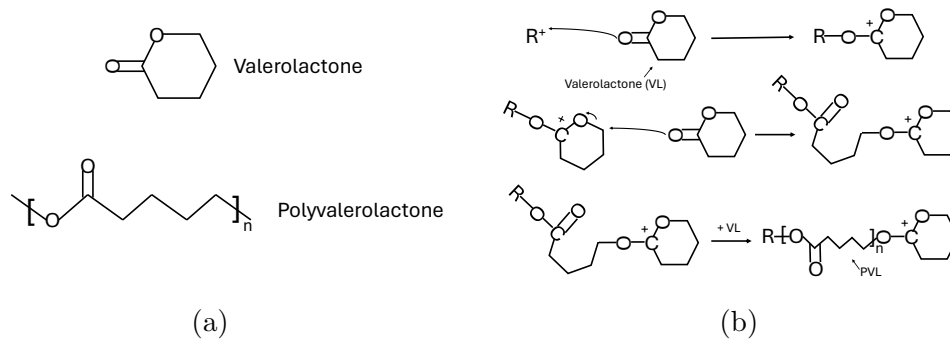
Figure 2.3: (a) Chemical structures of valerolactone (VL) and polyvalerolactone (PVL) (b) Cationic ring-opening polymerization of PVL, the mechanism is proposed by Penczek [59] and Kricheldorf [60]. R^+ is a cationic initiator.

2.1.2   Biodegradability of polyesters

Biodegradability is mentioned in Chapter 1, which is one of the most attractive properties of aliphatic polyesters. This work **does not** involve any studies of biodegradability. In this section, I briefly introduce some relevant definitions, an important biodegradation reaction of polyesters and some evaluation methods for biodegradability, in order to complete a full picture of aliphatic polyesters. Please note that I am aware of the complexity of this theme because of the broadness of definition and large amount of test protocols for evaluating biodegradation. Clarifying the complexity or avoiding ambiguity is out of the scope of this section.

Biodegradation and biodegradable polymers have the following definitions according to IUPAC. Biodegradation refers to the breakdown of a substance catalyzed by enzymes in vitro or in vivo. Biodegradable polymers are polymers susceptible to degradation by biological activity with the degradation accompanied by a lowering of their molar mass. Although degradations of polymer can be realized by many reactions, e.g. thermal, chemical and mechanical reactions, only a few of these reactions are mild enough to be seen in the natural environment, one of which is a hydrolysis reaction. Hydrolysis reaction involves breaking covalent bonds by water molecules.

Figure 2.4: A scheme of the hydrolysis reaction of PBS

The hydrolysis reaction is actually the reverse reaction of the esterification reaction, by which some polyesters are synthesized. Even if the polyesters are not synthesized by a polycondensation reaction, the ester bonds on the backbone of polyesters are mostly susceptible to hyd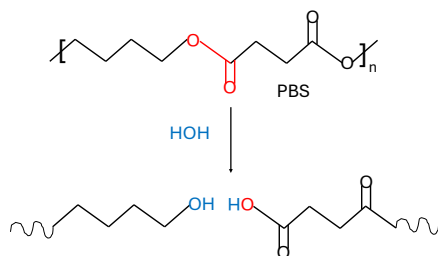rolysis. Figure 2.4 shows the scheme of a hydrolysis reaction. Therefore, compared with other types of polymers, polyesters are relatively more biodegradable (water or moisture is considered to be found almost everywhere). Certainly, the rate of the hydrolysis reaction, or whether the reaction takes place or not, is largely dependent on many factors, e.g. temperature, humidity, PH value or the presence of a catalyst. Apart from the hydrolysis reaction, the other mild reactions for biodegradation, which are more demanding in terms of the reaction conditions, e.g. enzymatic degradation and photo degradation, can be found only in the specific environments, e.g. aquatic environment, and composting condition, either separately or simultaneously. As for detailed information, please see the reference [57].

The physical, chemical and biological surroundings among many environments where plastics can end up vary quite a lot, different methods and protocols are thus used to evaluate whether the sample is biodegradable or not. Some of the methods are relative specific or in-house methods, to which there is normally no access. Some of the methods are standard ones, which are referring to ASTM (American Society for Testing and Materials), ISO (International Organization for Standardization), DIN (German Institute for Standardization), etc., which are available from the corresponding organizations. An ASTM method, ASTM D5988-18, is briefly described here as an example. This ASTM tests the biodegradability of plastic in soil, which is prepared in the lab or obtained from the natural environment according to procedure in the norm. The amount of CO_2 generated from the plastic sample during the test period is monitored and compared with the reference material. Not only do all different environments have different test methods, landfilling (e.g. ASTM D5526-94D), aquatic environment (e.g. ISO 18830:2016), compost (e.g. ASTM D6400-21), even in one environment, there are also different standards (ISO 19679:2020, ISO 14853:2016, etc., are all for the aquatic environment). It is rather likely that a biodegradable polyester is biodegradable in a certain environment, but is a non-degradable polymer in others. Therefore, the topic of biodegradability of polyesters, is supposed only to be discussed under specific conditions or the environment.

2.2 Polymer crystallization

Polymer crystallization is a broad subject covered by many polymer physics textbooks, some of which provide the basis for this section [51,61]. This section aims to briefly introduce the basic concepts or the features of polymer crystallization relevant to this study.

2.2.1   Structure and morphology

Similar to low molar mass compounds, polymers, including aliphatic polyesters, are able to form crystals, if they possess regular chemical structure. Below, I introduce the characteristic structure and morphology of semicrystalline polymers, from Å to μm. Polymers crystallize usually from their melt (similar to the crystallization conditions in this study), in which polymer chains are random coils and inter-penetrate each other to form entanglements. Chains are partially stretched to form crystalline regions during crystallization. The description of a crystal structure of a polymer is not different from that of a low molar mass compound. For instance, the description contains the crystal system, crystal unit cell and lattice constant. It is also possible that some of the polymers, e.g. the aliphatic polyesters in this study, can form more than one sort of crystal form, i.e. different unit cells, either at different crystallization conditions or simultaneously at the same condition. This phenomenon is called polymorphism. To avoid complexity due to polymorphism, if a sample shows polymorphism in this study, the focus is only on one of the accessible forms in terms of the characterization and the crystallization conditions. Figure 2.5 (a) presents, as an example, the structure of the unit cell of the crystal of Polyethylene (PE). Two chains with all-trans conformation pass through the unit cell. One unit cell includes two C_2H_4 groups. The unit cell is described by three unit vectors: a, b and c. As the unit cell is an orthorhombic crystal system (or symmetry), three unit vectors are perpendicular to each other. All A-B polyesters in this study form an orthorhombic crystal system (cf. Chapter 4). c is along chain direction, with a dimension of 2.55 Å. a and b have a length of 7.42 and 4.95 Å, respectively. The dimensions of the crystalline region in a and b directions (crystal growth directions) are much larger than that of the c direction, as the dimension of the c direction is governed by the stability of the crystal (explained in Section 2.2.2). The unstretched chains form amorphous regions which are stacked with crystalline regions alternatively, as shown in Figure 2.5 (b). This two-phase lamellar structure (it is called semicrystalline morphology in the text below) can be described by three parameters: the average crystalline layer thickness (d_c), the average amorphous layer thickness (d_a) and the long period (LP) which is the sum of d_a and d_c. These three parameters have a dimension from a few nm to a few tens of nm. It is also possible to calculate the degree of crystallinity (X_c) by these three parameters, as

$$X_c = \frac{d_c}{LP} \cdot 100\% \tag{2.2}$$

From Figure 2.5 (b), to clarify one confusion, the polyethylene chains are not necessarily normal to the lamella stacks, or the tilting angle of the chains does not necessarily need to be zero. For the detailed information, please refer to the reference [62]. From a nucleus, the lamellar structure grows with branching and splaying, and fills a spherical space. The so-called spherulite is observed in the size of μm by an optical microscope, as schematically shown in Figure 2.5 (c).
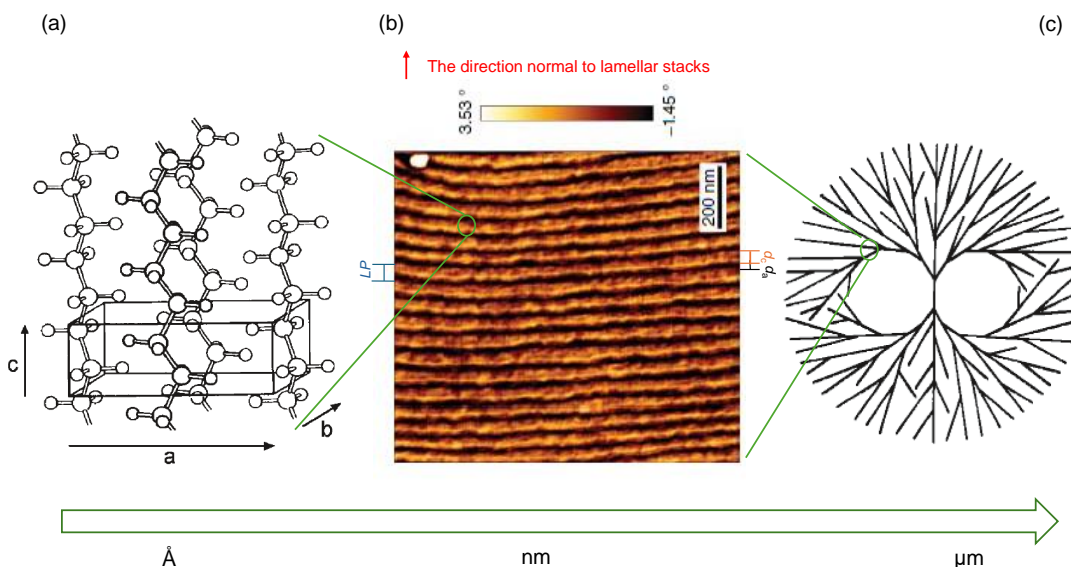
Figure 2.5: (a) Unit cell of PE crystallites. The figure is adapted from the reference [49]. (b) AFM phase image of the lamellar structure of a sample of linear low-density polyethylene, the bright stripes represent crystalline layers with thickness of d_c, the dark stripes are amorphous layers with thickness of d_a. The red arrow is the direction normal to lamellar stacks. The figure is adapted from the reference [50]. (c) Schematic drawing of a fully developed spherulite. The figure is adapted from the reference [49].

2.2.2 Kinetics and thermodynamics

Crystallization kinetics

Unlike small molar mass compounds, the crystallization of polymers usually starts at a temperature far below their melting temperatures (T_m) according to the regular Differential Scanning Calorimeter (DSC) cooling scans (cf. Chapter 3), or more precisely, the equilibrium melting temperatures (T_m^0), which is explained below. As this dynamic cooling experiment involves the process of nucleation and crystal growth, it is easier to study crystallization kinetics at isothermal conditions. An optical microscope (cf. Chapter 3) can be used to separate the nucleation and crystal growth process of a polymer at isothermal conditions. As nucleation is not the main focus of this study, I do not expand on this topic here. Figure 2.6 shows the typical dependence of the growth rates of spherulites for different polymers measured by optical microscope on super cooling (difference between T_m^0 and isothermal crystallization temperature). The growth rate of three polymers demonstrates a "bell-shape" curve. The rate has a maximum at a temperature between zero super cooling and glass transition temperature. From the maximal rate temperature to zero super cooling,

the rate decreases. From the maximal rate temperature to T_{g}, the rate decreases as well. The curve can be described by the following equation [63].

$$\mu = \mu_0 \cdot exp - \frac{T_{\mathrm{A}}}{T - T_{\mathrm{V}}} \cdot exp - \frac{B}{T_{\mathrm{m}}^0 - T} \tag{2.3}$$

where μ is the growth rate of spherulite, T_{A} is activation energy (1000-2000 K), B is a polymer-dependent constant, T_{m}^0 is equilibrium melting temperature, T_{V} is Vogel temperature, which is 30-70 K lower than T_{g}. The first exponent function (containing T_{V}) controls the left half of the bell shape, while the second exponent function dominates the right half of the bell shape of the curve.
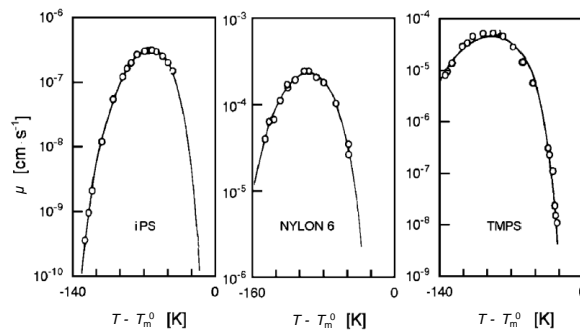
Figure 2.6: Examples of temperature dependence of the radial growth rate of spherulite of different polymers [61]. iPS is isotactic polystyrene, Nylon6 is poly(ϵ-caprolactam), and TMPS is poly tetramethyl-p-silpheylene siloxane. T_{m}^0 is the equilibrium melting temperature, which is explained in the following section, μ is the growth rate of a spherulite of a polymer. The figures are adapted from the reference [64].

Crystallization thermodynamics

Crystallization kinetics relies on thermodynamics which provides the driving force (the reduction of Gibbs free energy, G) for the crystallization process. A practical example is to precisely determine the dependence of μ on temperature based on Equation 2.3. This determination relies on a thermodynamic parameter: equilibrium melting temperature (T_m^0), which means the melting temperature of an infinite thick crystal. T_m^0 is normally determined by the Gibbs-Thomson equation, as shown in Equation 2.4

$$T_m = T_m^0 (1 - \frac{2\sigma}{d_c \rho_c \Delta H_m^0}) \tag{2.4}$$

where σ is the specific surface (the fold surface normal to lamellar stacks) free energy $(\mathrm{J\,m^{-2}})$, ρ_c is the density of the crystalline region, ΔH_m^0 is the specific melting enthalpy of the crystal $(\mathrm{J\,g^{-1}})$. Below, I introduce the basics of thermodynamics relevant to polymer crystallization through the explanation of the derivation of Equation 2.4.
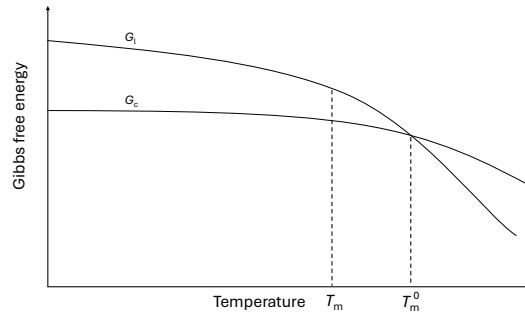
Figure 2.7: Schematic plot of the Gibbs free energy of polymer melt (G_l) and crystal (G_c) vs. temperature, melting temperature (T_m) and equilibrium melting temperature (T_m^0)

Figure 2.7 shows the Gibbs free energy of polymer melt (G_l) and polymer crystal (G_c) at different temperatures. The two curves cross over at the equilibrium melting temperature, below which $G_l > G_c$, above which $G_l < G_c$. Polymer crystallization takes place at the crystallization temperature (T_c), which is below T_m^0. To simplify the question, $T_c = T_m$ is assumed. The crystal thickening is excluded from the case. Gibbs free energy at molten status (polymer melt) or crystalline phase (polymer crystal) is defined as

$$G_l = H_l - T_m S_l, \ G_c = H_c - T_m S_c \tag{2.5}$$

where $G_{l,c}$, $H_{l,c}$ and $S_{l,c}$ are the Gibbs free energy in the melt/crystalline phase, enthalpy in the melt/crystalline phase, and entropy in the melt/crystalline phase,

respectively, at temperature T_m. The change of Gibbs free energy ((ΔG)) between two phases at temperature (T_m) is the difference between equations in Equation 2.5. For instance, the change of Gibbs free energy ((ΔG)) from melt to crystalline state is expressed as

$$\Delta G = \Delta H - T_m \Delta S \tag{2.6}$$

where ΔG is $G_c - G_l$, ΔH is $H_c - H_l$ and ΔS is $S_c - S_l$. When ΔG is negative, polymer crystal is favored, as the energy is reduced. The greater the absolute value of ΔG is (the lower the T_c or T_m is), the larger the driving force is for the phase transition. It is assumed that ΔH and ΔS are not temperature-dependent. During an equilibrium phase transition, ΔG is zero, and the temperature is T_m^0.

$$\Delta G = 0 = \Delta H - T_m^0 \Delta S \tag{2.7}$$

ΔG can also be divided into a surface-independent change and a surface-dependent change as

$$\Delta G = \Delta g^* \cdot M + \sum_{i=1}^{n} A_i \sigma_i, \ M = \rho_c A d_c \tag{2.8}$$

where Δg^* is the surface-independent specific free energy change with a unit of $\mathrm{J\,g^{-1}}$, M is the mass of the substance experiencing phase change, A is the area of the fold surface. If it is an equilibrium phase transition, Equation 2.9 is valid.

$$\Delta g^* \cdot M = \sum_{i=1}^{n} A_i \sigma_i \tag{2.9}$$

In comparison with the area of the fold surface, the surfaces parallel to lamellar stacks are negligible as

$$\sum_{i=1}^{n} A_i \sigma_i \approx 2A\sigma, \tag{2.10}$$

Δg^* can be described by the specific enthalpy change (ΔH_m^0) and the specific entropy change (ΔS_m^0) at a temperature of T_m as

$$\Delta g^* = \Delta H_m^0 - T_m \Delta S_m^0 = \Delta H_m^0 (1 - \frac{T_m \Delta S_m^0}{\Delta H_m^0}) \tag{2.11}$$

Similar to Equation 2.7, when it is an equilibrium phase transition, Δg^* is zero.

$$\Delta g^* = \Delta H_m^0 - T_m^0 \Delta S_m^0 = 0, \ T_m^0 = \frac{\Delta H_m^0}{\Delta S_m^0} \tag{2.12}$$

Combining Equations 2.9, 2.10, 2.11, 2.12 leads to the Gibbs-Thomson equation. In practice, a linear relationship is observed in the plot of $\frac{1}{d_c}$ versus T_m. T_m^0 is obtained by the extrapolation of T_m to $\frac{1}{d_c}$ equal to zero. The slope of the plot contains the information of the fold surface energy (σ) and the enthalpy of melting (ΔH_m^0).

Certainly, there are other ways to determine the equilibrium melting temperature of a polymer crystal, e.g. Hoffmann-Weeks plot. For the detailed information, please refer to the reference [65].

With the Gibbs-Thomson equation (Equation 2.4), it is not only possible to determine T_m^0, but also to understand the dependence of d_c on T_m, i.e. the higher the melting temperature of a polymer crystal, the greater its d_c is. When d_c goes into infinite, T_m is equal to T_m^0.

2.2.3 Intracrystalline chain diffusion (ICD)

Does d_c only depend on T_m? According to the reference [66] and some experimental results in this study, some polymers increase their d_c with crystallization time, but some do not. This increase is assigned to the contribution of intracrystalline chain diffusion (ICD), or α_c-relaxation. This process is realized by the so-called helical jump or monomer jump. Let's take one polymer chain, which is partially in a crystal, as an example. The monomer jump means that this chain can diffuse further into the crystal along the chain in the crystal by one monomer at a temperature above T_g. Consequently, on the side of the crystallite, the chain length has increased by one monomer, while the chain length in the amorphous regions has been decreased by one monomer. When waiting long enough, more monomers can diffuse stepwisely into crystalline regions according to the same pattern. Therefore, d_c can also increase over time. The monomer jump follows an Arrhenius temperature dependence and can be described as

$$\langle \tau_c \rangle = \tau_0 \cdot \exp \frac{E_a}{RT} \tag{2.13}$$

where $\langle \tau_c \rangle$ is the average correlation time of a monomer jump at a temperature of T, which is the average residence time of a monomer in a given crystal raster position, E_a is the activation energy, τ_0 is a fitting parameter. $\langle \tau_c \rangle$ can be measured by NMR measurements (cf. Chapter 3). The presence of ICD can also be probed by rheology measurements and dielectric measurements. The semicrystalline polymers showing the presence of ICD or α_c-relaxation are called crystal-mobile polymers, and the semicrystalline polymers showing no measurable ICD are called crystal-fixed polymers. A non-measurable ICD means that $\langle \tau_c \rangle$ is longer than 1 s. If $\langle \tau_c \rangle$ is less than 1 s, it is measurable. The measurable and non-measurable ICD also lead to different semicrystalline morphology and secondary crystallization behaviors, as explained in the following sections.

2.2.4 Typical semicrystalline morphology of crystal-fixed and crystal-mobile polymers

The recent study from our group [50] shows that it is possible to model the morphology of semicrystalline polymers (average thickness of the crystalline layers (d_c), average thickness of the amorphous layers (d_a) and their distribution widths σ_c and σ_a) by a series of Gaussian distributions. With the help of this model, Schulz and co-workers [47, 48] found that under isothermal crystallization conditions, crystal-fixed polymers typically show greater d_a than d_c, while crystal-mobile polymers show greater d_c than d_a, as schematically illustrated in Figure 2.8. d_c of a crystal-fixed polymer does not vary significantly within the polymer, as its d_c is largely dependent on T_c and there is no additional ICD that enables further thickening of d_c. However, there is a relatively large distribution width in terms of d_a of the crystal-fixed polymer. For a crystal-mobile polymer, its d_c has a large distribution width in the polymer because of the

presence of ICD. In contrast, d_a of a crystal-mobile polymer is quite uniform within the polymer. Therefore, in the following text, the typical semicrystalline morphology of crystal-fixed polymer refers to d_a and its distribution width being greater than d_c and its distribution width. The typical semicrystalline morphology of crystal-mobile polymer refers to d_c and its distribution width being greater than d_a and its distribution width.
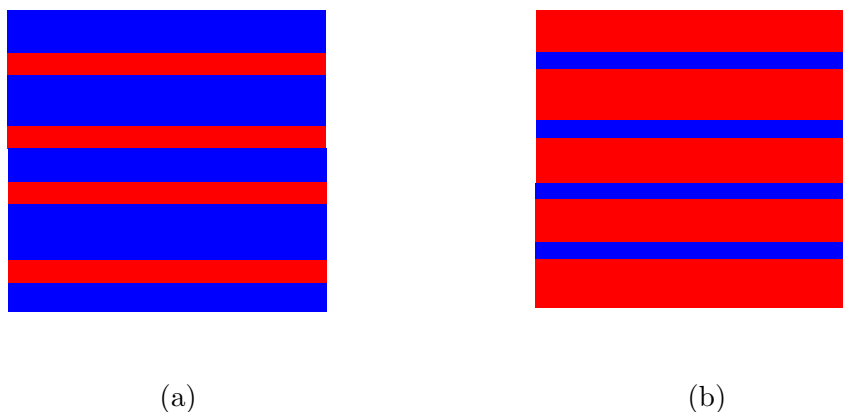

(a) (b)

Figure 2.8: (a) Schematic view of the typical semicrystalline morphology of a crystal-fixed polymer, the red stripes are crystalline layers, the blue stripes are amorphous layers (b) Schematic view of the typical semicrystalline morphology of a crystal-mobile polymer, the red stripes are crystalline layers, the blue stripes are amorphous layers.

2.2.5 Insertion crystallization and surface crystallization

Polymers with and without measurable ICD show different types of secondary crystallization. In this section, secondary crystallization refers to the crystallization during cooling after isothermal crystallization finishes at the isothermal crystallization temperature (T_c).

Figure 2.9 (a) schematically shows a typical semicrystalline morphology of a crystal-fixed polymer formed at a crystallization temperature that is higher than room temperature (RT). When the polymer is further cooled down to RT, the semicrystalline morphology is illustrated in Figure 2.9 (b). Due to the decrease in temperature, additional thin crystals were formed in the amorphous regions. This type of secondary crystallization is called insertion crystallization, which is the main mechanism of secondary crystallization of a crystal-fixed polymer. The insertion crystallization can be either observed by direct imaging techniques or the combination of SAXS and WAXS measurement (cf. Chapter 3). In addition, it is also possible to observe this increase in crystallinity by NMR measurement [67].

Figure 2.10 (a) schematically shows a typical semicrystalline morphology of a crystal-mobile polymer formed at a crystallization temperature (T_c) above room tem-

(a)   (b)

Figure 2.9: (a) Schematic view of typical semicrystalline morphology of crystal-fixed polymer, the red stripes are crystalline layers, the blue stripes are amorphous layers (b) Schematic view of insertion crystallization, which takes place based on the morphology in (a), the red stripes are crystalline layers, the blue stripes are amorphous layers. The figures are adapted from the reference [61].

perature. Figure 2.10 (b) shows the morphology when the polymer is cooled to RT from T_c. Different from the insertion crystallization, no or few thin crystals is formed during cooling or at RT. Instead, the interface between d_c and d_a shifts towards an amorphous region by reducing d_a and increasing d_c. As this type of secondary crystallization takes place at the interface between the crystalline and amorphous regions, or the surface of the crystalline regions, it is called surface crystallization. Typically, the crystallinity due to surface crystallization does not increase so significantly as insertion crystallization. The surface crystallization process can easily be observed by NMR and SAXS measurements. For further detailed explanations of these two modes of secondary crystallization, please refer to the reference [61].

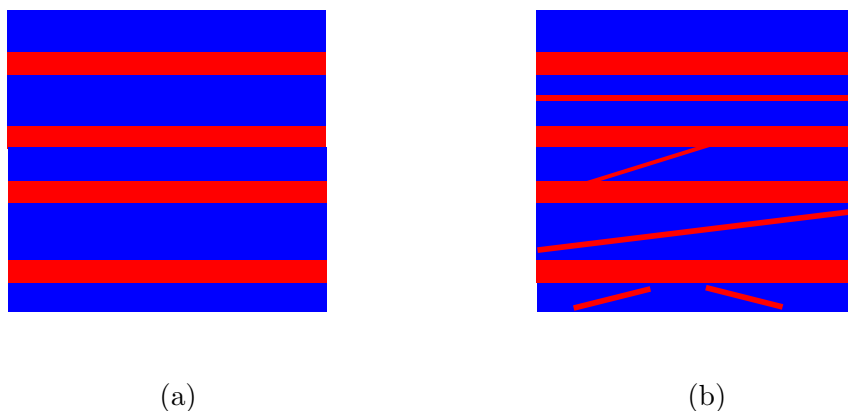(a)   (b)

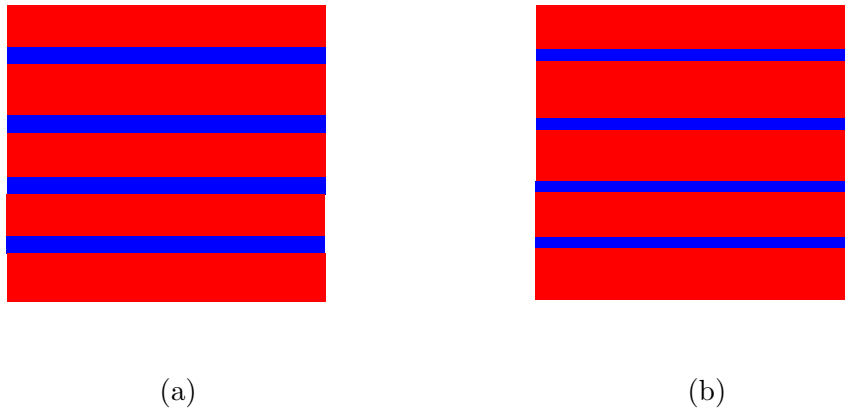Figure 2.10: (a) Schematic view of the typical semicrystalline morphology of a crystal-mobile polymer, the red stripes are crystalline layers, the blue stripes are amorphous layers (b) Schematic view of surface crystallization which takes place based on the morphology in (a), the red stripes are crystalline layers, the blue stripes are amorphous layers. The figures are adapted from the reference [61].

Chapter 3

Experimental methods

This study involves experimental techniques of X-ray scattering (Small Angle X-ray Scattering (SAXS) and Wide Angle X-ray Scattering (WAXS)), Nuclear Magnetic Resonance (NMR), rheology, Differential Scanning Calorimeter (DSC) and Polarized Optical Microscopy (POM). In this chapter, I provide basic knowledge of each experimental technique, demonstrate procedures for their data analysis and show examples of the data analysis to facilitate understanding of the results in the following sections. The detailed instrument parameters and sample treatments are found in the experimental section in the corresponding chapters.

3.1 X-ray scattering

The X-ray scattering technique is used to study of the structure of polymers. SAXS and WAXS are two scattering techniques covering different ranges of scattering angles that measure different length scales of an investigated structure. A structure with a dimension of 1-100 nm is within the measurement range of SAXS, while a structure with a dimension of 1-10 Å is measured by WAXS. The two techniques are presented below individually.

3.1.1 SAXS

SAXS is used to characterize the semicrystalline morphology of the aliphatic polyesters in this study, which is on a length scale of 1 to 100 nm. The average crystalline (d_c) and amorphous (d_a) thickness layer, and their distribution width σ_c and σ_a, respectively, of the samples are determined based on the data analysis of SAXS measurements. In this section, I schematically introduce the SAXS setup, and then provide a guide through the corresponding definitions, necessary derivations and calculations, in order to explain the interpretation of the angular-dependent intensity. The second part of this section covers the application of the basic knowledge of a semicrystalline polymer system. The data analysis and their corresponding examples are demon-
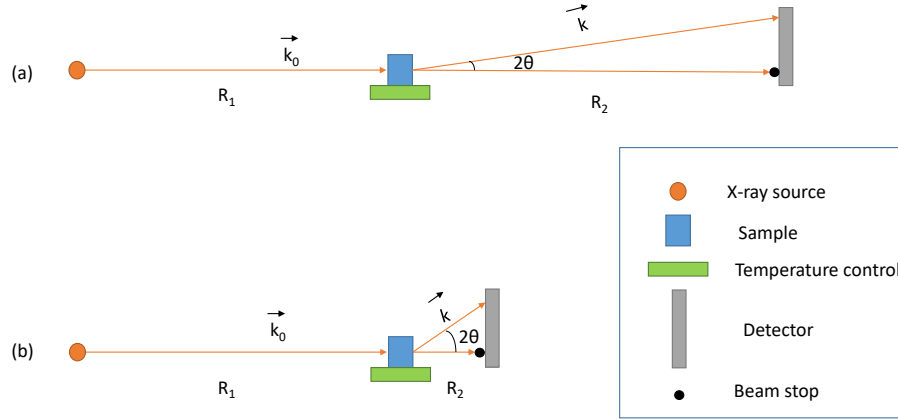
Figure 3.1: Schematic view of X-ray scattering instruments (a) SAXS, (b) WAXS

strated in the third part of this section. The books of Roe [68] and Strobl [61], and the paper by Seidlitz and co-workers [50] provide the basis of section 3.1.1.

Setup and basic knowledge of SAXS

The sample in Figure 3.1 (a) is irradiated by X-ray (J_0, plane wave) with a wavelength of λ_0 and a wave vector $\vec{k_0}$ ($\left|\vec{k_0}\right| = 2\pi/\lambda_0$). There is a fixed distance between the sample and the X-ray source, R_1. R_2 is a sample-to-detector distance, which is calibrated before a measurement and not changed during the measurement. After being irradiated, the scattered radiation (J, spherical wave) with a wavelength of λ (elastic scattering $\lambda_0 \approx \lambda$) and a wave vector $\vec{k}$ is recorded as a function of angle (2θ) by the detector. The aim of the SAXS experiment based on this layout is to measure an angular-dependent intensity ($I(2\theta)$) of the sample. The angular-dependent intensity can be further analyzed to determine d_c, d_a and their distribution width σ_c and σ_a, respectively.

The **scattering vector** ($\vec{s}$) is the difference between the incident ($\vec{k_0}$) and the scattered ($\vec{k}$) wave vector.

$$\vec{s} = \frac{1}{2\pi}(\vec{k} - \vec{k_0}) \tag{3.1}$$

$|\vec{s}|$ is, therefore, a function of θ based on Equation 3.2.

$$|\vec{s}| = \frac{2sin\theta}{\lambda} \tag{3.2}$$

The angular-dependent flux J becomes thus a scattering-vector-dependent flux ($J(\vec{s})$), as described below

$$J(\vec{s}) = A(\vec{s}) \cdot A(\vec{s})^* = |A(\vec{s})|^2 \tag{3.3}$$

where $A(\vec{s})$ is the sum of the amplitudes of the scattered waves originating from all scattering centers in the sample, $A(\vec{s})^*$ is the complex conjugation of $A(\vec{s})$. Equation 3.4 shows $A(\vec{s})$ with continuous version of electron density distribution function ($\rho(\vec{r})$)

$$A(\vec{s}) = A_0 b_e \int_V \rho(\vec{r}) e^{-i2\pi\vec{s}\cdot\vec{r}} d\vec{r} \tag{3.4}$$

where A_0 is the amplitude of the incident beam, b_e is the scattering length of an electron. With the description of $A(\vec{s})$ by $\rho(\vec{r})$, Equation 3.3 can be replaced by Equation 3.5.

$$J(\vec{s}) = A_0{}^2 b_e{}^2 \int_V \int_V \rho(\vec{r_1}) e^{-i2\pi\vec{s}\cdot\vec{r_1}} \rho(\vec{r_2}) e^{i2\pi\vec{s}\cdot\vec{r_2}} d\vec{r_1} d\vec{r_2} \tag{3.5}$$

Instead of using variables $\vec{r_1}$ and $\vec{r_2}$, a new variable is adopted $\vec{r}$.

$$\vec{r} = \vec{r_1} - \vec{r_2} \tag{3.6}$$

Equation 3.5 is, then, replaced by Equation 3.7.

$$J(\vec{s}) = A_0{}^2 b_e{}^2 \int_V \left(\int_V \rho(\vec{r_2} + \vec{r}) \rho(\vec{r_2}) d\vec{r_2} \right) e^{-i2\pi\vec{s}\cdot\vec{r}} d\vec{r} \tag{3.7}$$

The mathematical expression in the bracket of Equation 3.7 is an auto-correlation function of $\rho(\vec{r_2})$, as described by Equation 3.8.

$$g(\vec{r}) = \int_V \rho(\vec{r_2} + \vec{r}) \rho(\vec{r_2}) d\vec{r_2} \tag{3.8}$$

To simplify the further interpretation and analysis of intensity, I introduce $\delta\rho(\vec{r_2})$ to replace the electron density distribution function $\rho(\vec{r_2})$, according to Equation 3.9

$$\delta\rho(\vec{r_2}) = \rho(\vec{r_2}) - \langle\rho\rangle \tag{3.9}$$

where $\langle\rho\rangle$ is the average density of the sample. Equation 3.8 is rewritten as

$$g(\vec{r}) = \int_V \delta\rho(\vec{r_2} + \vec{r}) \delta\rho(\vec{r_2}) d\vec{r_2} + constant \tag{3.10}$$

and becomes a sum of an auto-correlation function of $\delta\rho(\vec{r_2})$ and a constant ($\langle\rho\rangle^2$). $\langle\rho\rangle^2$ gives only an unmeasurable contribution to forward scattering when $\vec{s}$ is 0. On the other hand, angular-dependent intensity is defined as the ratio of $J(\vec{s})$ to J_0, based on the same definition from the book by Roe [68], which is also the differential scattering cross-section.

$$I(\vec{s}) = \frac{J(\vec{s})}{J_0} \tag{3.11}$$

J_0 is not dependent on θ or $\vec{s}$ but equal to $|A_0|^2$. To combine Equations 3.11, 3.10 and 3.7, the dependence of the intensity on the autocorrelation function ($g(\vec{r})$) is established as

$$I(\vec{s}) = b_{\mathrm{e}}^2 V \int_V g(\vec{r}) e^{-i2\pi \vec{s} \cdot \vec{r}} d\vec{r} \tag{3.12}$$

To remove the dependence of scattering intensity ($I(\vec{s})$) on a sample volume and the electron scattering length (b_{e}), the intensity in context below refers to absolute scattering intensity (I_{abs}), which is normalized by the volume of the sample and the electron scattering length.

$$I_{\mathrm{abs}}(\vec{s}) = I(\vec{s})/(b_{\mathrm{e}}^2 V) = \int_V g(\vec{r}) e^{-i2\pi \vec{s} \cdot \vec{r}} d\vec{r} \tag{3.13}$$

Application of SAXS on semicrystalline polymers

The morphology of an ideal semicrystalline polymer is approximated according to Figure 3.2 (a). Along the z-direction, crystalline layers (in red) and amorphous layers (in blue) stack on each other alternatively to form a two-phase system. There is a sharp boundary between a crystalline layer and an amorphous layer, and a substantial electron density difference ($\delta\rho(z)$) between two neighboring layers. Perpendicular to z-direction, the lateral dimension of each crystalline and amorphous layer is much greater than d_{c} and d_{a}.

Based on the above approximation, the scattering-vector-dependent intensity from a SAXS measurement on a semicrytalline polymer sample (Equation 3.13) contains only the information on the change of electron density along the z-direction within the measurement length scale (1-100 nm). Therefore, it is reasonable to reduce the 3D correlation function ($g(\vec{r})$) into a 1D correlation function ($K(z)$ is denoted as the 1D correlation function in the following context). Then, Equation 3.13 is reduced as

$$I_{\mathrm{abs}}(s) = \frac{2}{4\pi s^2} \int_{-\infty}^{\infty} K(z) e^{-i2\pi s z} dz \tag{3.14}$$

The correlation function can be calculated through Fourier transformation of $2\pi s^2 I_{\mathrm{abs}}(s)$ as described by Equation 3.15

$$K(z) = \int_{-\infty}^{\infty} 2\pi s^2 I_{\mathrm{abs}}(s) e^{i2\pi s z} ds \tag{3.15}$$

d_{c} and d_{a} can be determined by $K(z)$, the procedure was described in detail in the reference [50]. Although this interpretation is frequently used for the determination of the morphology of semicrystalline polymers, this approach is not the focus in this study due to its disadvantages, which are comprehensively elaborated in the reference [50] as well. The approach of this study is to interpret the second derivative of $K(z)$, $K''(z)$, or the so-called Interface Distribution Function (IDF). On the one hand, the IDF function of an ideal lamellar structure system can be described by a series of delta functions at the interfaces between different phases, as shown in

Figure 3.2 (c). These delta functions are broadened in a semicrystalline polymer that deviates from the ideal one. $K''(z)$ can then be described as

$$K''(z) = \frac{O_{\text{ac}}\Delta\rho}{2}(h_{\text{a}}(z) + h_{\text{c}}(z) - 2h_{\text{ac}}(z) + h_{\text{aca}}(z) + h_{\text{acc}}(z) - ...)\tag{3.16}$$

where O_{ac} is the specific inner surface per unit volume of the interfaces between crystalline and amorphous regions, which is inversely proportional to the sum of d_{a} and d_{c}, $\Delta\rho$ is the electron density difference between two phases, $h_{\text{a,c}}(z)$ is the distribution of d_{c} and d_{a}, which is described by a normal distribution function as

$$h_{\text{a,c}}(z) = \frac{1}{\sqrt{2\pi}\sigma_{\text{a,c}}}e^{-\frac{(z-d_{\text{a,c}})^2}{2\sigma_{\text{a,c}}^2}}\tag{3.17}$$

where $\sigma_{\text{a,c}}$ is the distribution width, d_{c} and d_{a} are the peak positions.

On the other hand, the IDF function can also be calculated directly from $I_{\text{abs}}(s)$ as

$$K''(z) = -8\pi^3\int_{-\infty}^{\infty}s^4 I_{\text{abs}}(s)e^{i2\pi sz}ds\tag{3.18}$$

However, the measured I_{abs} contains extra contributions from the scattering signal of a two-phase system (Ps^{-4}), thermal density fluctuations within the amorphous phase (c_2), a contribution from the amorphous halo $(c_1 s^2)$. P, Porod parameter, is related to the specific inner surface O_{ac} and the electron density difference $\Delta\rho$ as

$$P = \frac{O_{\text{ac}}\Delta\rho^2}{8\pi^3}\tag{3.19}$$

c_1 and c_2 are constants. P is used to determine when the crystallization process is changed from primary crystallization to secondary crystallization. This information should be subtracted from I_{abs} before the calculation of $K''(z)$ according to Equation 3.20.

$$K''(z) = -8\pi^3\int_{-\infty}^{\infty}(I_{\text{abs}} - Ps^{-4} - c_1 s^2 - c_2)s^4 e^{i2\pi sz}ds\tag{3.20}$$

As the description of $K''(z)$ for semicrystalline polymer system is found from both experimental and theoretical sides, $K''(z)$ becomes the bridge between theoretical modeling and experimental measurement. In the next section, I will describe the practical procedure of using a theoretical model to interpret experimental results to determine d_{c}, d_{a} and their distribution width σ_{c} and σ_{a}, respectively.
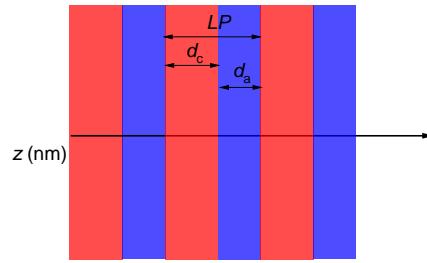
(a) Ideal lamellar stack with the z-direction along the lamellar normal. The crystalline layer is in red with a thickness of d_c, the amorphous layer is in blue with a thickness of d_a, long period is $LP = d_a + d_c$.
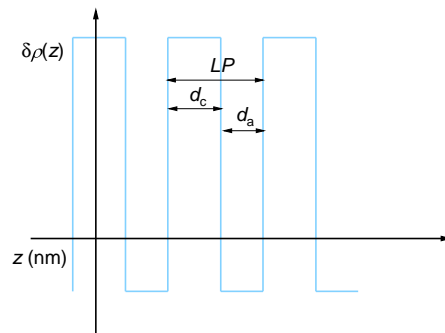
(b) Electron density difference along the z-direction according to (a)
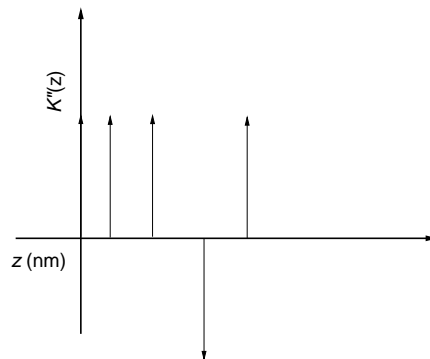
(c) The interface distribution function (IDF or $K''(z)$) according to (a)

Figure 3.2: Schematic view of ideal lamellar stacks in semicrystalline polymer system, its electron density difference in different phases and its IDF

SAXS data analysis and examples

According to Equation 3.20, $K''(z)$ can be calculated from experimental data through Fourier transformation. Practically, the cosine transform is used to realize the calculation as

$$K''(z) = -16\pi^3 \int_0^\infty (I_{\mathrm{abs}} - Ps^{-4} - c_1 s^2 - c_2)s^4 \cos(2\pi s z)ds \qquad (3.21)$$

Due to large noise at large scattering vectors, the experimental data is multiplied by a window function to suppress noise

$$w(s) = e^{-4\pi\sigma^2 s^2} \qquad (3.22)$$

where σ is the width of the window function. Depending on the selection of σ, different levels of noise suppression is achieved. Of course, this window function is also taken into account on the left side of Equation 3.20 in the form of convolution of $K''(z)$ and $w(z)$.

It is also possible to perform inverse transformation from $K''(z)$ back to experimental data,

$$2 \int_0^\infty \frac{(K''(z) * w(z))}{8\pi^3} \cos(2\pi z)dz = (I_{\mathrm{abs}} - Ps^{-4} - c_1 s^2 - c_2)s^4 w(s) \qquad (3.23)$$

This property is critical for the data analysis, as no analytical solution for IDF ($K''(z)$) is found find, but the analytical solution for its Fourier transformation [50]. Therefore, according to the solution containing fitting parameters d_{c}, d_{a}, σ_{c} and σ_{a}, a fit is performed on the experimental data $((I_{\mathrm{abs}} - Ps^{-4} - c_1 s^2 - c_2)s^4 w(s))$. Then, it is checked if the fitting is reasonable by applying transformation of the fit and experimental data according to Equation 3.21 into real space. The detailed process is elaborated by the two examples in Figure 3.3.

Figure 3.3 (a) shows the measured I_{abs} and Porod fit ($Ps^{-4} + c_1 s^2 + c_2$) based on PBS, which crystallized at T_{c}=100 °C. P, Porod parameter, was determined under the condition that Equation 3.21 is equal to zero when z is zero. The scattering signal from a two-phase system at large s gives a constant contribution (P) in reciprocal space, which shows up as an δ function at $z = 0$ in real space, as shown in Figure 3.2 (c). Therefore, Equation 3.21 containing no contribution of P should be zero when z is zero. c_1 and c_2 were determined based on the shape of I_{abs} at large s. Figure 3.3 (c) shows the difference between I_{abs} and the Porod fit ($I_{\mathrm{abs}} - Ps^{-4} - c_1 s^2 - c_2)s^4 w(s)$ and the fit in red based on the solution [50]. With this fit, d_{c}, d_{a}, and their distribution width σ_{c} and σ_{a} are determined. The assignment of d_{a} and d_{c} is usually based on the crystallinity measured by DSC, NMR, or other techniques. In the case of PBS, the assignment of d_{a} and d_{c} was based on the crystallinity measured by [1] NMR-FID. As the crystallinity of PBS at T_{c}=100 °C is around 40%, d_{c} was assigned to the peak at low z value. The cosine transform of both the fit and the difference in Figure 3.3 (c) were illustrated in Figure 3.3 (e). In addition, the decomposition of $K''(z)$,

based on the transformation of the fit, into crystalline contribution (h_c), amorphous contribution (h_a) and long period contribution (h_{ac}) are presented as dashed lines in Figure 3.3 (e). Figure 3.3 (b), (d) and (f) follow the same structure based on a P3HB sample. P3HB normally has higher than 50% crystallinity, d_a, d_c assignment was different from the assignment of PBS.

In this study, d_c, d_a and their distribution width σ_c and σ_a are compared with the typical morphology of crystal-fixed and crystal-mobile polymers (cf. Chapter 2), in order to find out to which category of polymer a sample belongs.
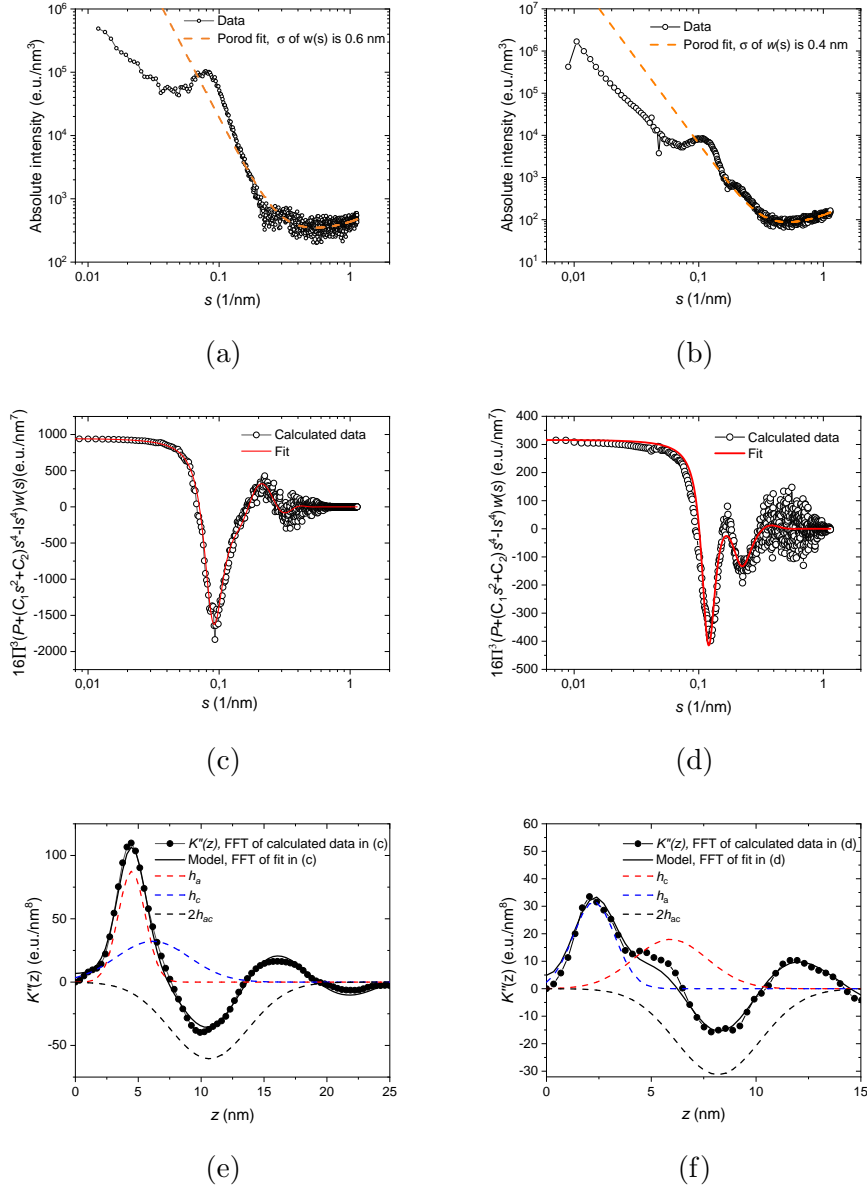
Figure 3.3: (a) I_{abs} and Porod fit of PBS, (b) I_{abs} and Porod fit of P3HB (poly-3-hydroxybutyrate), (c) $(-I_{\text{abs}} + Ps^{-4} + c_1 s^2 + c_2)s^4 w(s)$ of PBS and the fit according to the solution in the reference [50], (d) $(-I_{\text{abs}} + Ps^{-4} + c_1 s^2 + c_2)s^4 w(s)$ of P3HB and the fit according to the solution in the reference [50], (e) The cosine transformation of the fit and $(-I_{\text{abs}} + Ps^{-4} + c_1 s^2 + c_2)s^4 w(s)$ in (c) and its decomposition in three contributions (dashed lines) h_{c}, h_{a} and $2h_{\text{ac}}$, (f) The cosine transformation of the fit and $(-I_{\text{abs}} + Ps^{-4} + c_1 s^2 + c_2)s^4 w(s)$ in (d) and its decomposition in three contributions (dashed lines) h_{c}, h_{a} and $2h_{\text{ac}}$

3.1.2   WAXS

WAXS is widely used to determine the crystallinity of semicrystalline polymers, it is, however, rather difficult to analyze WAXS data precisely [69]. Therefore, in this study, WAXS is used only to observe a relative change in the crystallinity of the samples, instead of quantitatively determining the absolute crystallinity of the samples. In this section, I schematically introduce the setup and the procedure for observing the change in the crystallinty by WAXS.

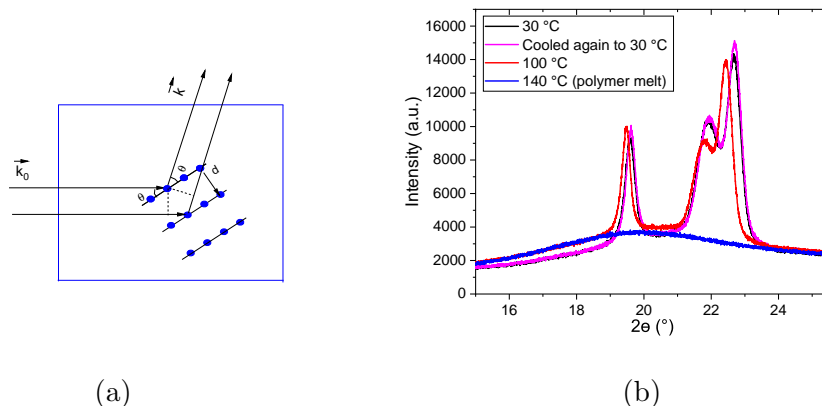(a)   (b)

Figure 3.4: (a) Bragg reflection (b) WAXS measurements on PBS (Polybutylene succinate) at different temperatures

The setup of WAXS is schematically shown in Figure 3.1 (b). Similar to SAXS setup, the sample is irradiated by X-ray with a wavelength of λ_0 and a wave vector $\vec{k_0}$, the scattered radiation with a wavelength of λ (elastic scattering $\lambda_0 \approx \lambda$) and a wave vector $\vec{k}$ is recorded as a function of angle by the detector. In comparison with the setup of SAXS, the sample-to-detector distance (R_2) of the setup of WAXS is much smaller, which enables WAXS to determine up to a rather wide angle. However, the resolution at a small scattering angle is very poor.

The same as other regular crystals, semicrystalline polymer has also lattice planes in crystalline region with separation of d between two adjacent planes (cf. Chapter 2). According to Bragg's law (Equation 3.24), Bragg reflection takes place when $2\sin(\theta)d$ is equal to wavelength or integral multiple of wavelength, as schematically shown in Figure 3.4 (a).

$$2\sin(\theta)d = n\lambda \tag{3.24}$$

The examples of the measurement results are shown in Figure 3.4 (b). The red curve in Figure 3.4 (b), obtained from semicrystalline PBS at $T_c = 100\,°C$, indicates that the Bragg reflection occurs under a few angles. WAXS signal is not only contributed by the crystalline part, but also the amorphous part (amorphous halo), as shown by the blue curve in Figure 3.4 (b), which was the measurement based on a fully molten PBS.

A method of determination of crystallinty was proposed by Ruland [69]. However, it is rather difficult to perform analysis due to tedious procedures. Empirically, X_c is determined by the equation below

$$X_c = \frac{A_c}{A_{total}} \cdot 100\% \tag{3.25}$$

where A_c is the scattering peak area due to Bragg reflection, A_{total} is the total area below the scattering curve. However, it is uncertain over which range of 2θ A_{total} is determined. Although this empirical method gives limited precision of crystallinity values, it might be practical for observation of a relative change of crystallinity. Let's compare the curves in red and black in Figure 3.4 (b), it is qualitatively clear that the intensity of the Bragg reflections increases at the expense of the amorphous background when the temperature decreases, which indicates an increase in crystallinity. In this study, WAXS is always combined with other experimental techniques (SAXS, NMR and DSC) to confirm the observation of the crystallinity change.
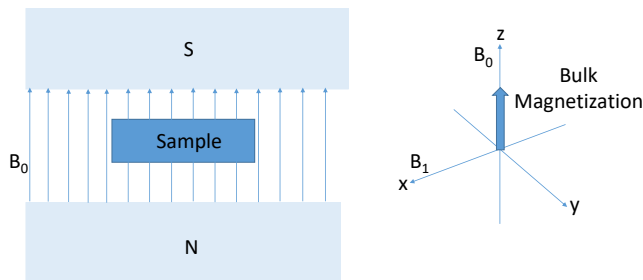
Figure 3.5: Schematic view of NMR instrument

3.2   Nuclear magnetic resonance

Solid-state NMR is suitable for characterizing molecular structure and dynamics of semicrystalline polymers. Various NMR techniques are used to measure slow ($\langle \tau_c \rangle$ up to 1 s) and fast ($\langle \tau_c \rangle < 200\,\mu\text{s}$) intracrystalline chain diffusion, and the crystallinity of the aliphatic polyesters. In this study, the measurements and corresponding data analyses were carried out by Afiq Anuar in cooperation with the solid-state NMR group headed by Prof. Dr. Kay Saalwächter. The aim of this section is to provide the fundamental principles of NMR, in order to enable the basic interpretation of NMR data in the following chapters. Before presenting each NMR technique involved in this study, I will start with a basic understanding of NMR techniques. The book by Keeler [70] provides the basic knowledge of NMR.

NMR spectroscopy is based on a spin property of nuclei, which is characterized by a nuclear spin quantum number, I. Nuclei with a non-zero spin quantum number are NMR-active and detectable by NMR. The samples in this study, polyesters, consist of carbon (C), hydrogen (H) and oxygen (O) nuclei. ^{1}H is NMR-active and accounts for nearly 100% natural abundance. In contrast, ^{12}C and ^{16}O are not NMR-active, while their isotopes ^{13}C and ^{17}O are NMR-active. However, The low natural abundance of ^{13}C requires a significant number of scans to achieve an acceptable signal-to-noise ratio. ^{17}O, of which natural abundance is less than 0.1%, is not the focus of this work.

When NMR-active nuclei are placed in an external magnetic field B_0, as shown in Figure 3.5, the nuclei show different energy levels. Let us take one ^{1}H as a specific and simple example. This proton has two energy levels, $+1/2v_0$ and $-1/2v_0$ under the magnetic field of B_0 in the z-direction. v_0 is Larmor frequency in units of hertz (Hz) and has a dependence on B_0 as

$$v_0 = \frac{1}{2\pi}\gamma B_0 \tag{3.26}$$

where γ is a gyromagnetic ratio. A higher B_0 results in a larger energy difference or frequency difference. The energy difference between these two levels (v_0) is reflected by a peak at a frequency of v_0 in the NMR spectra. Instead of using frequency to describe this energy difference or the peak position in the NMR spectra, chemical shift relative to an agreed reference compound (TMS, tetramethylsilane) is conventionally used to quote the NMR frequency as exemplary expressed below

$$\delta_{\mathrm{ppm}} = \frac{v_0 - v_{\mathrm{TMS}}}{v_{\mathrm{TMS}}} \cdot 10^6 \tag{3.27}$$

where v_{TMS} is the Larmor frequency of proton of TMS, the unit of chemical shift is in part per million or ppm. The implementation of chemical shift eases the communication of NMR data among different research groups because the dependence of v on the external magnetic field is removed and the value of δ_{ppm} is rather practical than v which often contains 9 different digits with a unit of Hz. The situation is more complex when there are more than one spin. Energy levels vary due to the interactions between different spins (spin-spin coupling), of which the details can be found in reference [70].

When a polyester sample, which contains many nuclei, is placed in the magnetic field of B_0, each individual nucleus behaves like a small magnetic moment. When all the small magnetic moments are added up together, a net magnetic field along the direction of B_0 is formed, which is called bulk magnetization, as shown in Figure 3.5. The bulk magnetization can be perturbed by applying a radio-frequency (RF) pulse (B_1) in the x-y plane, which tilts the magnetization away from the z-axis. It can relax back to its original status after the pulse. There are two types of relaxation process that are critical in this work. T_2 relaxation (transverse relaxation) describes the process by which the bulk magnetization in the x-y plane decays back to zero after the RF pulse. This decay is due to the loss of phase coherence among the spins as a result of spin-spin interactions. These interactions cause individual spins to process at slightly different frequencies, leading to a dephasing effect and a reduction in the overall signal. The other relaxation is T_1-relaxation (longitudinal relaxation), which describes the process by which the bulk magnetization returns to its equilibrium state along the z-axis after being perturbed by an RF pulse.

This study involves several NMR techniques, governed by T_1- and T_2-relaxation processes, to probe different aspects of the polymer samples, which is explained below. For an in-depth methodological description of all methods, please refer to the corresponding references [67, 71–76] and Chapter 5, 6 and 7.

3.2.1   Low field ^{1}H NMR-free induction decay

A 90° pulse is applied to the sample in the magnetic field of B_0. Then, FID signals (x-y plane) are recorded over time by a coil directly after the 90° pulse. The FID signals contain the information of fast segmental dynamics of protons in the amorphous phase and the strong ^{1}H–^{1}H dipole–dipole couplings in the crystalline phase. The strong dipole-dipole coupling results in a fast decay of the FID signal, while fast segmental dynamics lead to a slow decay of the signal. In addition, the FID signals consist of another intermediate decay, which is assigned to the intermediate phase. The entire FID signals are empirically described as

$$I_{\mathrm{FID}}(t) = f_{\mathrm{c}} \cdot e^{-(a^2 t^2/2)} \cdot \frac{\sin{(b \cdot t)}}{b \cdot t} + f_{\mathrm{i}} \cdot e^{-(t/T_{2,i}^*)^{v_{\mathrm{i}}}} + f_{\mathrm{a}} \cdot e^{-(t/T_{2,a}^*)^{v_{\mathrm{a}}}} \qquad (3.28)$$

where t is the acquisition time, $f_{\mathrm{c,i,a}}$ is the amplitude of the corresponding decaying component, $T_{2,i},^*$ $v_{\mathrm{a,i}}$ are the shape parameters of the more mobile components, while a and b are the shape parameters of the crystalline part. To probe the presence of fast ICD, the crystalline contribution to the FID is isolated from $I_{\mathrm{FID}}(t)$. When the crystalline contributions at different temperatures show a difference in terms of the shape, there is a presence of fast ICD. When all crystalline contributions overlap with each other, there is no presence of fast ICD in the time scale of µs. The mass crystallinity is calculated based on

$$X_{\mathrm{c}} = \frac{f_{\mathrm{c}}}{f_{\mathrm{c}} + f_{\mathrm{i}} + f_{\mathrm{a}}} \cdot 100\% \qquad (3.29)$$

In practice, due to the dead time (switching from applying pulse to recording), some of the signals are missing at the very beginning. To reproduce the missing signals, an Magic-Sandwich Echo (MSE) is applied [72]. Although the missing signals are reproduced by MSE, the intensity of the entire signal is slightly reduced. Therefore, the shape parameters are taken from the fitting of MSE-FIDs, while component amplitudes are taken from the measured FID. Figure 3.6 shows an example of the FID curve in green obtained from PBS (poly butylene succinate) during isothermal crystallization at 100 °C. The missing signals at the beginning of the FID curve were reproduced by MSE in black. The MSE curve was fitted by Equation 3.28 to determine all the shape parameters (a, b, $T_{2,i}^*$ and $v_{\mathrm{a,i}}$). Then, the FID curve was fitted by Equation 3.28 with all the fixed shape parameters from MSE fitting to determine $f_{\mathrm{c,i,a}}$. With all the determined parameters of FID, the decomposition of three contributions are shown in Figure 3.6, they are in blue, red and dark red. The crystalline contribution (in blue) is used for further investigation of fast ICD. If no fast ICD in the sample is found, NMR high field measurements are carried out to probe whether there is a presence of slow ICD or not, as described in the sections below. The mass crystallinity of this PBS sample was determined by Equation 3.29 with $f_{\mathrm{c,i,a}}$ obtained from the FID.
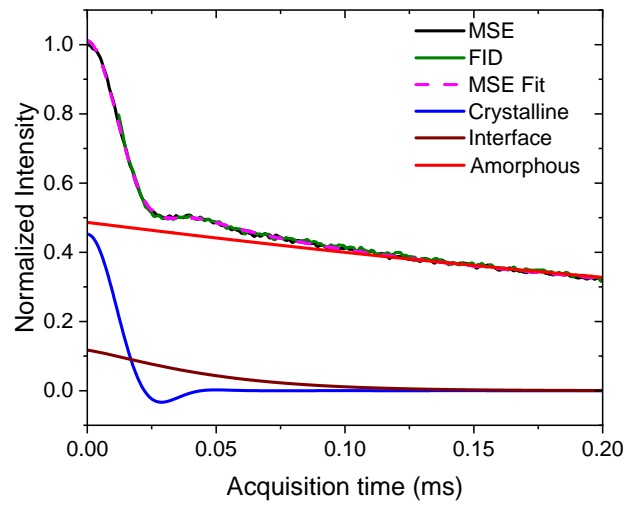
Figure 3.6: FID, MSE-FID and MSE fit of PBS at T_{c}=100 °C and the three fitted components of the MSE-FID

3.2.2   High field ^{13}C NMR

High field ^{13}C NMR MAS Spectroscopy

All high-field ^{13}C NMR techniques below were performed under the Magic Angle Spinning (MAS) condition, where dipole coupling interaction is averaged. The ^{13}C spectroscopy technique was used to reveal all possible chemical shifts of ^{13}C in the samples in this study under MAS. With ^{13}C direct polarization (DP) and ^{13}C cross-polarization (CP), which relies on ^{1}H-^{13}C dipolar polarization transfer, it is possible to differentiate ^{13}C resonance in the crystalline region from ^{13}C resonance in the amorphous region of the semicrystalline samples from ^{13}C spectra. Therefore, ^{13}C spectroscopy with different polarization methods lays a foundation for further investigation of the specific crystalline ^{13}C peaks in the sample by two other NMR techniques below.

High field ^{13}C NMR CODEX

^{13}C Centerband-Only Detection of Exchange (CODEX) NMR measurements reveal slow motions of the different chemical groups, which rely on the rotation of the Chemical Shift Anisotropy (CSA) tensors. In this study, CODEX was used to measure the average correlation time $\langle \tau_{c} \rangle$ describing ICD. The CSA information is normally lost under MAS conditions, but can be selectively reintroduced (recoupled) by different pulses or a combination of a series of pulses before and after a mixing time (τ_{mix}, waiting time). The intensity of the corresponding crystalline ^{13}C peak based on ^{13}C spectroscopy measurement is recorded over mixing time (τ_{mix}). Molecular rotations during τ_{mix} lead to a decay of the intensity of the corresponding crystalline peak. $\langle \tau_{c} \rangle$ is determined according to a fit of the decay of the peak intensity in the reference [75]. The detailed information of the fit is described in the reference [75]. If no reorientation of the CSA tensor occurs during τ_{mix}, the intensity of the corresponding peak remains constant, which indicates no presence of ICD up to a timescale of 1 s.

High field ^{13}C T_1-relaxation and diffusive exchange

For some of the polyesters in this study, CODEX measurement is unsuitable to measure τ_{c}. It is because the polyesters possess all-trans rather than helical chain conformation, where the translation by one monomer unit results in all atoms crystallographically equivalent positions. In those cases, ^{13}C T_1-relaxation and diffusive exchange were used to characterize diffusive long-range ICD of the samples with which CODEX can not deal. An intense crystalline peak based on the ^{13}C spectra is chosen to probe its T_1-relaxation. The information contained in the decay of the T_1-relaxation process, the suitable pulse sequence and the interpretation of ICD from the decay were described in detail in the references [71, 77].

3.3   Rheology

Rheology is a versatile technique, which can be used to characterize visco-elastic properties, dynamic mechanical properties, relaxation process and etc., of polymers. In this study, dynamic shear modulus was measured by a rotational rheometer at different temperatures (below T_{m}). Whether there is a relaxation process in the crystalline regions (α_{c}) of the samples was probed, by constructing a master curve based on the Time Temperature Superposition (TTS) principle. In this section, I briefly introduce the frequency-dependent modulus of polymer and the TTS principle with an example, in order to explain qualitatively how the dynamic shear modulus of the samples is measured and how the presence of α_{c} relaxation in the samples is observed. The books by Rubinstein [78] and Strobl [61] provide the necessary references for this section.
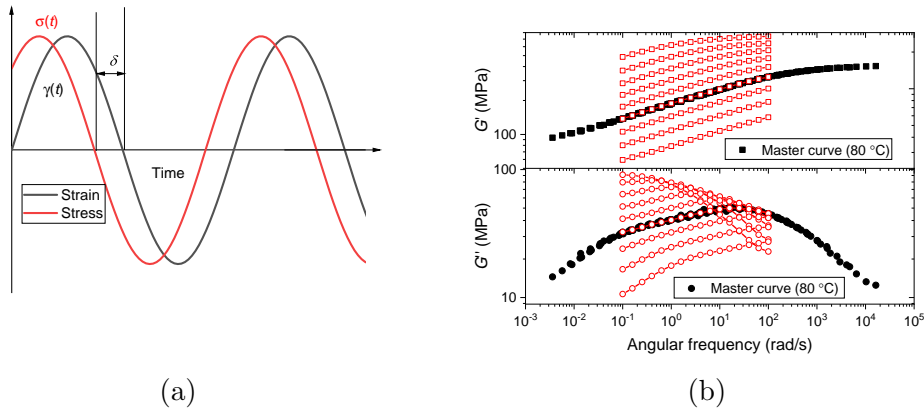

(a)	(b)

Figure 3.7: (a) Dynamic stress-strain curves, δ is the phase angle (b) The master curves of G' and G'' of HDPE (Total Lumicene$^{\circledR}$ mPE M5510 EP, $M_{\mathrm{n}} = 27\,700\,\mathrm{g\,mol}^{-1}$, PDI $= 2.8$), reference temperature is $80\,^{\circ}\mathrm{C}$. Due to the small change of crystallinity with temperature, unsubstantial shift factors along the y axis were involved. The red hollow dots are the data measured at different temperatures but at the same frequency range (0.1-$100\,\mathrm{rad\,s}^{-1}$). The black dots are the shifted data, for the construction of the master curves.

Shear modulus (G) is known as the ratio of shear stress (σ) to shear strain (γ) in the static mode

$$G = \frac{\sigma}{\gamma} \tag{3.30}$$

In the dynamic mode, an applied strain is described as

$$\gamma(t) = \gamma_0 \sin(\omega t) \tag{3.31}$$

where ω is the shear frequency, t is time and γ_0 is the amplitude of the strain, which is mathematically shown in Figure 3.7. For the linear response (rather small strain

0.1%) of a viscoelastic material, e.g. the polymer samples in this study, the stress oscillates at the same frequency as the applied strain, and contains additionally a phase angle expressed as

$$\sigma(t) = \sigma_0 \sin(\omega t + \delta) = \sigma_0 \cos(\delta) \sin(\omega t) + \sigma_0 \sin(\delta) \cos(\omega t) \tag{3.32}$$

where δ is the phase angle, σ_0 is the amplitude of stress. It is possible to decompose the stress into two orthogonal functions that oscillate with the same frequency, one in-phase with the strain and the other out-of-phase with the strain by $\frac{\pi}{2}$ as

$$\sigma(t) = \gamma_0 G'(\omega) \sin(\omega t) + \gamma_0 G''(\omega) \cos(\omega t) \tag{3.33}$$

where $G'(\omega)$ is in-phase frequency-dependent shear modulus, G'' is out-of-phase frequency-dependent shear modulus. When Equations 3.33 and 3.32 are combined, G' and G'' have then the expression below.

$$G'(\omega) = \frac{\sigma_0}{\gamma_0} \cos \delta, \;\; G''(\omega) = \frac{\sigma_0}{\gamma_0} \sin \delta \tag{3.34}$$

G' is defined as storage modulus and G'' is defined as loss modulus. The ratio of G'' to G' is the tangent of the phase angle, loss tangent.

$$\tan \delta = \frac{G''(\omega)}{G'(\omega)} \tag{3.35}$$

As $G'(\omega)$, $G''(\omega)$ and $\tan \delta$ are all frequency-dependent, in the following chapters, dynamic shear modulus (mainly G') are always compared among different samples under the same frequency.

The solid dots in Figure 3.7 (b) show typical frequency-dependent $G'(\omega)$ and $G''(\omega)$ of HDPE over a broad range of frequency at $80\,^{\circ}\text{C}$ (below T_m). $G'(\omega)$ decreases with frequency, and $G''(\omega)$ shows a broad peak, which indicates the presence of a relaxation process (α_c-relaxation, in this case). The curves are so-called master curves, which are constructed by shifting the corresponding hollow dots in red based on the Time Temperature Superposition (TTS) principle. TTS is a concept that a certain mechanical property of polymer (e.g. dynamical shear modulus) at one temperature (T) and frequency (ω) is a function of the mechanical property at reference temperature (T_r) and frequency ($a_\text{T}\omega$). This concept is, for instance, described as

$$G(T, \omega) = G(T_\text{r}, a_\text{T}\omega) \tag{3.36}$$

where a_T is the shift factor. For a logarithmic frequency scale, Equation 3.36 is replaced by

$$G(T, \log \omega) = G(T_\text{r}, \log \omega + \log a_\text{T}) \tag{3.37}$$

The shift factor is following Arrhenius dependence as

$$\log a_\text{T} = \log A - \frac{E_\text{a}}{RT} \cdot \log e \tag{3.38}$$

where A is the Arrhenius factor, E_a is the activation energy for α_c-relaxation process, R is the ideal gas constant and T is temperature. With the implementation of the TTS concept, a regular commercial rheometer, which can only reasonably probe dynamic modulus of a sample at angular frequency range from 0.1 to $100\,\mathrm{rad\,s^{-1}}$, is able to measure material properties in a broader range of frequency. TTS also enables us to screen the presence of α_c-relaxation of the samples in this study based on the criteria of observing a peak from a master curve of G''.

3.4   Differential scanning calorimetry

DSC is one of the most widely used thermal analysis techniques in the field of polymer science. In this study, the technique was used to determine the melting temperature (T_m) and melting enthalpy (ΔH) of each aliphatic polyester. As T_m and ΔH of all samples were measured by a power compensation DSC equipment, the following introduction of DSC instrument and working principle of DSC focus only on this type of equipment. Another popular type of DSC equipment (heat flux) is not discussed in this work. The book chapter of Mueller [79] provides the main basis for this section.
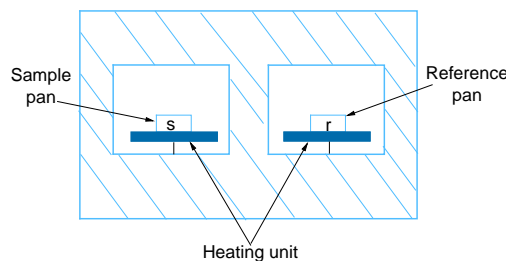

Figure 3.8: Schematic view of a power compensation DSC

Figure 3.8 shows a schematic view of power compensation DSC equipment. The instrument has two separate adiabatic chambers where the sample and the reference are placed within aluminum pans. For this study, the reference is air (an empty aluminum pan). The temperatures of the two pans change linearly with time and are always kept the same as each other, which is realized by the independent power output of two heating units in the chambers. The difference in the power output (power compensation) is recorded over time or temperature (if a heating rate is constant), which is proportional to heat flow ($\frac{dQ}{dt}$). The dependence of $\frac{dQ}{dt}$ on c_p (the specific heat capacity) is described by Equation 3.39

$$c_\mathrm{p} m \beta = \frac{dQ}{dt} \tag{3.39}$$

where m is mass of a sample, β is heating rate of a sample ($\frac{dT}{dt}$). Therefore, the recorded heat flow ($\frac{dQ}{dt}$) at different temperatures can be converted into c_p. Before the conversion, the heat flow to the pan is subtracted from the heat flow to the pan and sample, by running a baseline measurement with only empty pan.

The temperature at the maximal melting peak is selected as T_m. If the heating rate (β) is constant, Equation 3.39 can be rewritten as

$$c_\mathrm{p} m = \frac{dQ}{\beta dt} = \frac{dQ}{dT} \tag{3.40}$$

where T is the temperature of a sample. Therefore, the area under the peak is the corresponding enthalpy of melting, ΔH, which is often used to determine crystallinity of semicrystalline polymer by the following equation

$$X_c = \frac{\Delta H}{\Delta H_{m,100}} \cdot 100\% \tag{3.41}$$

where $\Delta H_{m,100}$ is the literature value of extrapolated enthalpy of melting of a hypothetical 100% crystalline sample, or called enthalpy of melting. In the study below, ΔH is used together with other techniques (SAXS and NMR-FID) to determine $\Delta H_{m,100}$ of each sample.

3.5   Polarized light optical microscopy

An optical microscope is commonly used to observe the information about the size, shape and relative arrangement of visible features of a sample. The characterization range of an optical microscope is from around 1 µm to several hundred µm. A polarized light optical microscope (POM) contains all the components of a conventional optical microscope and, in addition, two polarization filters, which are placed above and below a sample. In this study, POM is used to measure the growth rate of spherulite of polyesters, which has a dimension of a few µm. Below, a brief introduction to POM system and the procedure to measure the growth rate of spherulite are provided. Regarding other applications of POM in the field of polymer and basic knowledge of POM, please refer to the book by Sawyer [80], which also provides the basis for this section.
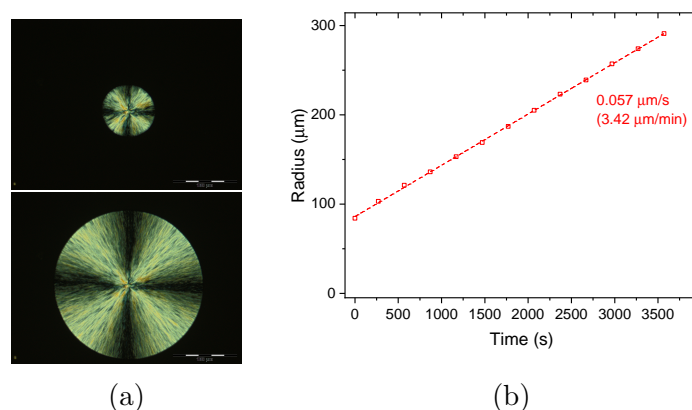

(a)   (b)

Figure 3.9: (a) POM pictures of a spherulite of PLLA at different time during the isothermal crystallization at $140\,^{\circ}\mathrm{C}$, analyzer has a 90° rotation with respect to polarizer. (b) The radius of the spherulite of PLLA (in (a)) vs. time measured at $T_{\mathrm{c}}=$ $140\,^{\circ}\mathrm{C}$. The dashed line is the linear fit.

An unpolarized light, generated from a light source, is polarized linearly after it goes through the first polarization filter (polarizer), which is placed between the light source and a sample holder. The light continues the path and reaches the second polarization filter (analyzer), which is placed between the sample holder and eyepiece and has a plane of polarization perpendicular to the polarizer. If there is no sample in the sample holder, or the sample is isotropic, no light can pass further through the analyzer to reach the objective and finally be observed by an eyepiece. If a polymer spherulite forms (anisotropic) from polymer melt (isotropic), a so-called maltese cross is observed, as shown in Figure 3.9 (a). Therefore, it is possible to record the growing process of a spherulite from polymer melt at different temperatures by using a camera. Figure 3.9 (b) is an example of the determination of a growth rate of spherulite of PLLA at $140\,^{\circ}\mathrm{C}$ temperature. The radius of the spherulite grows linearly with time.

The slope is the growth rate of the spherulite. The growth rate is compared with the timescale of ICD to determine whether a polyester is a crystal-fixed or crystal-mobile polymer.

Chapter 4

Sample system and state of the art

The aliphatic polyesters involved in this study were obtained from the market or the collaborating labs. The polyesters range from the simplest polyester (PGA) to the PE-like polyester (PPDL), which possess different numbers of CH_2 groups (N_{cc}) in the monomer units along the backbone of the polymer. The polyesters with the CH_3 group as a side chain are also included in the study. In addition, a successful and commercially available AA-BB polyester is investigated. The approach of the study is to test whether the proposals based on our previous studies [47, 48] are valid in the aliphatic polyesters by checking the semicrystalline morphology and intracrystalline chain diffusion (ICD) of all the polyesters. The polyesters with different N_{cc} are suitable for investigating the influence of N_{cc} on ICD and semicrystalline morphology. The polyesters with and without CH_3 group are suitable for the investigation of the impact of the CH_3 group as a side chain on ICD and semicrystalline morphology. This chapter provides the general introduction, crystalline structure, crystallization kinetics and thermodynamics, and an overview of semicrystalline morphology and ICD of each aliphatic polyester.

4.1   A-B aliphatic polyesters

4.1.1   Poly Glycolic Acid (PGA)

Introduction

PGA is the simplest polyester, the chemical structure of which is illustrated in Figure 4.1 (a). The polymer was first mentioned in 1932 [81]. Nowadays, PGA is commercially available, e.g. from Kureha Chemical Industry Co. Ltd., and synthesized by ring-opening polymerization method for large-scale production [82]. The synthesized polymer does not only have good mechanical properties (tensile modulus of 7.4 GPa and tensile strength of 117 MPa according to ISO 527 standard based on Kuredux® from Kureha), but it also withstands high temperatures (T_g of 45 °C and T_m of 222 °C) [83, 84]. Apart from the good mechanical and thermal properties,
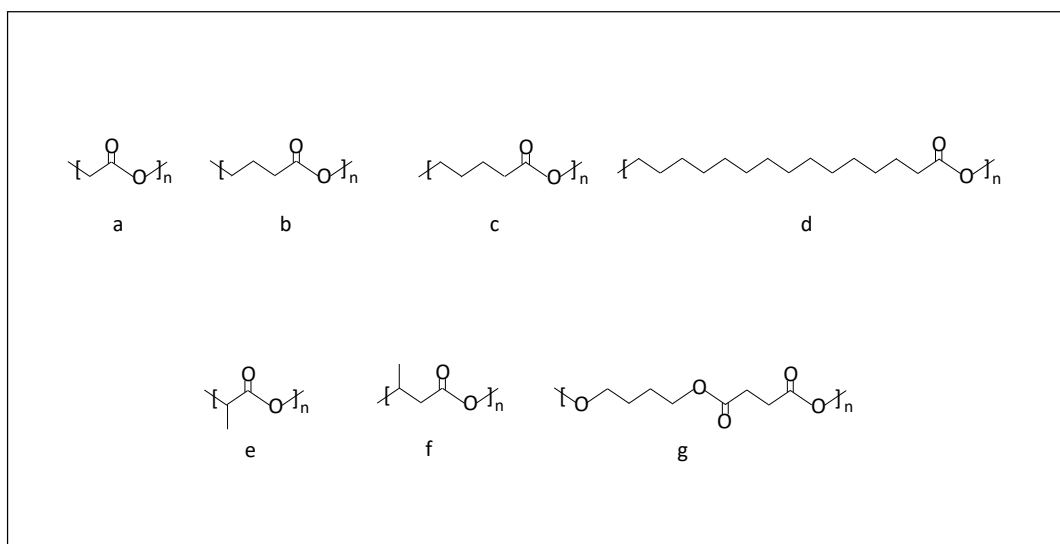
Figure 4.1: Chemical structure of all polyesters investigated in this study. (a) Poly Glycolic Acid (PGA), (b) Poly-4-hydroxybutyrate (P4HB), (c) Polyvalerolactone (PVL), (d) Poly ω-pentadecalactone (PPDL), (e) Poly-L-Lactide Acid (PLLA), (f) Poly-3-hydroxybutyrate (P3HB), (g) Polybutylene Succinate (PBS)

PGA is degradable, which is a desired property to tackle waste management of plastic waste. PGA is susceptible to hydrolytic degradation and is turned into glycolic acid in the natural environment [15, 85]. This polymer can also be degraded in vitro and in vivo [86]. It is degraded into small molecules, e.g. glycine, which is either excreted in the urine or converted into carbon dioxide and water [87]. Therefore, PGA is already used for many medical applications, e.g. sutures, scaffolding matrices for tissue regeneration and drug delivery [83]. The polymer is also used in certain packaging applications as a barrier material to lower gas permeability due to its high crystallinity [82], which partially reduces the environmental issue when the material is accidentally discarded into the natural environment. However, PGA is still not able to replace commodity plastic in a wide range of applications because of its high manufacturing cost [82] and its brittleness, which is characterized by short elongation at break (30%).

Crystalline structure

Niu et al. recently showed that PGA crystallizes in β form with unit cell dimensions (lattice constants): a = 0.872 nm, b = 0.502 nm, c (the fiber axis) = 2.05 nm at 60 °C under mechanical strain [88]. Polymer chains in β form crystal adopt 7_2 helical conformation, in contrast to its planar α form crystal, which was revealed in 1968 by Chatani and co-workers [89]. α form crystal contains planar zigzag chains in an orthorhombic unit cell with dimensions: a = 0.522 nm, b = 0.619 nm, and c (the fiber axis) = 0.702 nm. This semicrystalline polymer has a density of 1.5-1.6 g cm^{-3} (Kureha). Fully α form crystalline PGA has a density of 1.707 or 1.69 g cm^{-3}, while fully amorphous PGA has a density of 1.45 g cm^{-3} [90].

In addition, a number of studies found the existence of hydrogen bonds between polymer chains by terahertz technique [91, 92], which is likely to result in unusually high melting temperatures compared with other aliphatic polyesters.

Kinetics and thermodynamics of crystallization of PGA

Needle-like hedrites with a large length-to-diameter ratio were observed by Yu et al. at 200 °C [93]. The determination of the growth rate of the crystal of PGA is, therefore, difficult. Yu et al. also reported that PGA shows complicated melting behaviors: multiple melting peaks observed by DSC heating scan after isothermal crystallization at different temperatures [93]. Chen et al. studied the crystallization kinetics of PGA by fast-scanning DSC [94]. It is possible to measure the crystallization rate (determined by half time from heat flow during the isothermal crystallization procedure) at most temperatures from 75 to 175 °C. The entire "bell shape" curve was constructed, with a maximal crystallization rate of around 160 °C. Chujo et al. studied PGAs with different comonomer content to determine $\Delta H_{m,100}$, which is 2500 or 2800 calories per mole of crystallizable repeating unit (180 or 202 J g^{-1}) [95]. Cohn et al. used melting enthalpy (measured by DSC) of different PGAs with the known crystallinity from the

reference [96] to determine $\Delta H_{m,100}$ of PGA, $139\,\mathrm{J\,g^{-1}}$ [97]. Clapeyron–Clausius relation was employed to determine $\Delta H_{m,100}$ by Nakafuku and co-workers, $183\,\mathrm{J\,g^{-1}}$ [84]. The equation relies largely on the equilibrium melting temperature, which is difficult to precisely determine. The equilibrium melting temperature ($T_m{}^0$) of PGA, typically determined by Hoffman–Weeks plots, has a wide spread from $231.6\,^\circ\mathrm{C}$ to $252\,^\circ\mathrm{C}$ [84, 93].

Semicrystalline morphology and ICD

The semicrystalline morphology of β form was revealed recently by Niu et al. [88]. It has an amorphous layer thickness (d_a) of $4\,\mathrm{nm}$, crystalline layer thickness (d_c) of $2\,\mathrm{nm}$ and long period (LP) of $6\,\mathrm{nm}$ at an isothermal crystallization temperature of $60\,^\circ\mathrm{C}$ according to the analysis of 1D correlation function of SAXS data. Compared with β form, α form was more widely investigated by researchers. Unless otherwise specified, the crystal form of PGA in the below context refers only to α form, on which this study focuses. Montes et al. showed that α form crystal has $d_c = 7\,\mathrm{nm}$, $d_a = 6\,\mathrm{nm}$ and $LP = 13\,\mathrm{nm}$ at an isothermal crystallization temperature of $195\,^\circ\mathrm{C}$ [98], based on analysis by 1D correlation function of SAXS measurement. Nishimura et al. also used the 1D correlation function to analyze SAXS results and demonstrated the semicrystalline morphology of PGA at $185\,^\circ\mathrm{C}$: $d_a = 7.2\,\mathrm{nm}$, $d_c = 6.2\,\mathrm{nm}$ and $LP = 13.4\,\mathrm{nm}$ [91]. Yu et al. used SAXS technique to measure LP of PGA, which changes from 6 to $7.5\,\mathrm{nm}$ when the temperature goes from 170 to $200\,^\circ\mathrm{C}$ [93]. d_c from their study was determined by the product of the long period (Lorentz-corrected SAXS) and the crystallinity measured by DSC [93]. Montes et al. reported the crystallinity of 37 and 50% by using $^1\mathrm{H}$ NMR-FID and DSC techniques, respectively [99, 100]. Gilding et al. measured the crystallinity of 37% based on an analysis of WAXS results [96]. Sekine et al. used NMR FID to characterize the crystallinity of PGA at different temperatures [101]. They reported that the rigid fraction increased from 52 to 85% when the temperature decreased from 200 to $120\,^\circ\mathrm{C}$, which was due to the increase of the immobile amorphous fraction. No report of ICD has been found to the best of my knowledge.

4.1.2 Poly-L-Lactide Acid (PLLA)

Introduction

Similar to PGA, PLLA was also mentioned by Carother [81], whose chemical structure is shown in Figure 4.1 (e). PLLA is able to be synthesized by many methods, e.g. polycondensation, ring-opening polymerization (ROP), enzymatic polymerization [102], among which ring-opening polymerization is currently used for industrial production [103]. The polymer is commercially available, e.g. Luminy ® PLA from TotalEnergies Corbion Ltd. has T_g of $60\,^\circ\mathrm{C}$, T_m of $175\,^\circ\mathrm{C}$, the tensile modulus of $3500\,\mathrm{MPa}$ and elongation at break less than 5% (ISO 527-1, Luminy L175 from Total-

Energies Corbion). Although PLLA is relatively brittle, the property can be modified or improved by blending with PBS (Polybutylene Succinate) [25] and through suitable processing methods [104]. Due to its good thermal, tunable mechanical properties, relatively low manufacturing cost and, more importantly, degradability, the material shows potential to replace commodity plastics to solve plastic waste issues and is already the most widely used bioplastic in many industries [102]. PLLA is degradable, but its degradation reaction relies on PH value and temperature [105]. Therefore, PLLA does not degrade during landfills operation, which is the most common and problematic waste disposal method [20]. The material is also not degradable in the ocean, where littered plastics end up [106, 107]. The industrial composting condition (e.g. DIN EN 13432) is suitable for the degradation reaction of PLLA, under which PLLA is decomposed into small molecules that can be digested by bacteria [108]. More plastic waste going into composting contributes positively to current plastic waste management. In addition, the degradation reaction also takes place in vitro and in vivo [109], which expands applications of PLLA to medical and pharmaceutical fields, e.g. fracture fixation and drug delivery [83, 110].

Crystalline structure

PLLA possesses polymorphism, α, α', β, and γ forms crystals. α form crystal has two chains in a 10_3 helical conformation packed in an orthorhombic unit cell with a = 1.07 nm, b = 0.645 nm, c (fiber direction) = 2.78 nm [111]. α form, the main focus of PLLA in this study, is formed by cooling PLLA from melt to crystallization temperatures above 130 °C. Its density is 1.26-1.29 g cm^{-3} [112]. α' form has unit cell dimensions: a = 1.08 nm, b = 0.62 nm, c (fiber direction) = 2.88 nm [113]. This form is rather similar to α form. It has 10_3 helical chain conformation and is generated by cooling PLLA from melt to crystallization temperature at 100 °C or below. The density of α' form (1.25 g cm^{-3}) is lower than that of α form and rather closer to that of the fully amorphous PLLA (1.248 g cm^{-3}). Consequently, it is difficult to use SAXS measurement to characterize its semicrystalline morphology [112]. β form is generated by hot-drawing the melt-spun or solution-spun PLLA fibers to a high-draw ratio. It has six chains in a 3_1 helical conformation in an orthorhombic unit cell with a = 1.031 nm, b = 1.821 nm and c (fiber direction) = 0.900 nm [114]. Cartier reported that PLLA has γ form crystal, which is produced by epitaxial crystallization and is characterized by two helices with 3_1 conformation packed in an orthorhombic unit cell having unit cell dimensions: a = 0.995 nm, b = 0.625 nm, c (fiber direction) = 0.880 nm [115].

Kinetics and thermodynamics of crystallization of PLLA

Androsch et al. studied the growth rate of the spherulites of α form crystal by optical microscope [116]. The growth rate shows a maximum of around 125 °C, and decreases with increasing crystallization temperature. Meanwhile, they reported that the ap-

parent crystallization rate determined by half-time of DSC heat flow during isothermal crystallization reaches a peak value at $90\,°C$. Jariyavidyanont et al. reviewed thoroughly $\Delta H_{\mathrm{m,100}}$ of α form, which was from 90-200 $\mathrm{J\,g^{-1}}$, and they determined $\Delta H_{\mathrm{m,100}}$ by flash DSC technique, which is 104.5 $\mathrm{J\,g^{-1}}$ [117]. Abe et al. used non-linear and linear Hoffmann Weeks plots to determine the equilibrium melting temperature, which is 215 and $227.1\,°C$ [118, 119]. However, different crystal forms were not taken into account. Tsuji et al. used a linear Hoffmann Weeks plot to determine the equilibrium melting temperature, which is from $181\text{-}212\,°C$ [120].

Semicrystalline morphology and ICD of PLLA

Abe et al. characterized the crystalline layer thickness (d_{c}) and amorphous layer thickness (d_{a}) by both SAXS and Atomic-Force Microscopy (AFM) at different crystallization temperatures, e.g. d_{c}= 14.7 nm (SAXS result based on 1D correlation function), d_{c}= 17.1 nm(AFM) at T_{c}= $150\,°C$ [119]. Cho et al. determined d_{c} and d_{a} by SAXS measurement [121]. According to the analysis of interface distribution function on their SAXS data, PLLA has d_{c} of 20 nm and d_{a} of 8 nm at T_{c}= $143\,°C$, and does not show crystal thickening during isothermal crystallization. Chen et al. used center band-only detection of exchange (CODEX) NMR measurement to measure $\langle \tau_{\mathrm{c}} \rangle$ of the helical jump motions in α form crystal at different temperatures, i.e. $\langle \tau_{\mathrm{c}} \rangle$ is around 3-250 ms from 103-150 °C. $\langle \tau_{\mathrm{c}} \rangle$ exhibits Arrhenius behaviors, with the activation energy, E_{a}, around 91 $\mathrm{kJ\,mol^{-1}}$ [122, 123]. Song et al. reported different force-induced melting behaviors of PLLA and PCL (Polycaprolactone) due to the presence and absence of ICD, respectively [55].

4.1.3   Poly-3-hydroxybutyrate (P3HB)

Introduction

P3HB, first isolated by Lemoigne in 1925, is found in the soil bacteria [124], which is produced as an energy source against starvation. Its chemical structure is illustrated in Figure 4.1 (f). Although the polymer is possible to be chemically synthesized [125], it is currently produced by microorganisms on an industrial scale [126]. P3HB has a glass transition temperature of $0\text{-}27\,°C$ [127–129] and a melting temperature of $177\,°C$ [130]. The material has a tensile modulus of 1700 MPa and elongation at break of 5% according to $1\,\mathrm{mm\,min^{-1}}$ and $50\,\mathrm{mm\,min^{-1}}$ tensile rate, respectively (Biomer specification). As P3HB can be consumed by microorganisms, its biodegradability is widely recognized [16]. Due to its good biodegradability and thermal properties, P3HB is used for some applications either alone or as part of a blend with other polymers, e.g. packaging and tissue engineering [131, 132]. However, short elongation at break hinders broader applications of P3HB. It is well known that its elongation at break becomes even shorter during the storage time due to the slow secondary crystallization [133], which further restricts its applications. The details are presented

in Chapter 6.

Crystalline structure

P3HB possesses two forms of crystals, α and β forms. Yokouchi et al. revealed that the crystal unit cell of α form is orthorhombic with the lattice constants: a = 0.576 nm, b = 1.320 nm, c (fiber direction) = 0.596 nm. Polymer chains adopt 2_1 helical chain conformation in the crystal [134]. The lattice constants of β form crystal were also mentioned by Yokouchi et al. : a = b= 0.992 nm, c (fiber direction) = 0.596 nm. In contrast to α form, the polymer chains in β form crystals adopt the planar chain conformation. Iwata et al. demonstrated the generation of β form crystals under mechanical force from α form crystals [135]. This study focuses only on α form of P3HB. In addition, Sato et al. showed there is hydrogen bonding between the polymer chains in the crystal [136].

Kinetics and thermodynamics of crystallization of P3HB

Cao et al. measured the growth rate of a spherulite of P3HB at different crystallization temperatures and found that the maximum growth rate is around 80 °C [130]. Gaffar investigated the dependence of melting temperatures on crystallization temperatures by DSC technique [137]. The corresponding melting temperatures were used to determine the equilibrium melting temperature of P3HB, which is 197 °C according to Hoffmann Weeks plot. Barham et al. extrapolated melting enthalpies of P3HB obtained at different densities to the theoretical density of a fully crystalline P3HB. Unlike other relatively widely studied polyesters, this is the only available $\Delta H_{m,100}$ = 146 J g^{-1} in the literature [138].

Semicrystalline morphology and ICD

Heo et al. used 1D correlation function to analyze SAXS results and reported that P3HB has a crystalline layer thickness (d_c) of 8.9 nm and an amorphous layer thickness (d_a) of 3.7 nm at 145 °C [139]. They observed no crystal thickening at 145 °C within 60 min. Van Nguyen et al. and Chiu et al. characterized d_c and d_a at low crystallization temperatures (below 90 °C) [140, 141]. Xia et al. probed intracrystalline chain diffusion of P3HB by NMR-CODEX and claimed P3HB did not have measurable ICD at room temperature [142]. However, the study presented in Chapter 6 reported that P3HB has a measurable ICD at high crystallization temperatures.

4.1.4 Poly-4-hydroxybutyrate (P4HB)

P4HB was found in 1926 and was first reported in 2003 for implantable medical device applications by Tepha, Inc. [143]. Its chemical structure is illustrated in Figure 4.1 (b). It is difficult to synthesize P4HB chemically by ring-opening polymerization method because of the small ring strain of the monomers [144]. The commercially

available P4HB homopolymers are produced through a fermentation process [145]. The material has T_g of $-51\,^{\circ}$C and T_m of $60\,^{\circ}$C [145]. P4HB is a tough material. Its Young's modulus is around 120 MPa, and its elongation at break can reach 500%, both of which are dependent on molecular weight [146]. The product made from P4HB is degraded both in vitro and in vivo conditions [147,148]. Due to its unique mechanical properties and superior degradability, P4HB is already widely used in many medical applications, e.g. sutures and heart valves [145]. However, the crystallization of P4HB is rather rarely studied.

Su et al. reported that the unit cell of P4HB is orthorhombic with the lattice constants: a = 0.775 nm, b = 0.477 nm, c (fiber axis) = 1.199 nm [149]. The polymer chains adopt the planar chain conformation in the crystals. No polymorphism has been reported so far.

Keridou et. al reported the growth rate of spherulites of P4HB at different crystallization temperatures, where the maximum growth rate appears at $20\,^{\circ}$C [150].

Keridou et al. also studied the melting temperatures of P4HB after isothermal crystallization at different temperatures, which were used to determine the equilibrium melting temperature, $T_m{}^0 = 79.9\,^{\circ}$C (Hoffman weeks plot) [151]. No $\Delta H_{m,100}$ value is available in the literature.

Keridou et al. showed that P4HB formed a crystalline layer thickness of 7.9 nm and an amorphous layer thickness of 1 nm according to the analysis of the 1D correlation function of SAXS measurement. No study on intracrystalline chain diffusion of P4HB has been found.

4.1.5   Polyvalerolactone (PVL)

The homopolymer of PVL is seldom studied, of which chemical structure is illustrated in Figure 4.1 (c). I am not aware of any commercially available homopolymer, but only lab-scale synthesis. PVL homopolymer can be synthesized through ring-opening polymerization of valerolactone [152]. The synthesized polymer has a glass transition temperature (T_g) of $-67\,^{\circ}$C and a melting temperature of $52\,^{\circ}$C [152]. Its Young's modulus is around 570 MPa and its elongation at break is between 150-200% [152].

Furuhashi et al. reported an orthorhombic unit cell with the lattice constants: a = 0.747 nm, b = 0.502 nm, c (fiber axis) = 0.742 nm, in which the polymer chains adopt planar conformation [153]. No polymorphism is reported.

Yevstropov et al. reported that PVL has $\Delta H_{m,100}$ of $18.2\,\text{kJ}\,\text{mol}^{-1}$, which is $182\,\text{J}\,\text{g}^{-1}$, based on the combination of enthalpy measured by DSC and the crystallinity [154].

No study on the semicrystalline morphology and intracrystalline chain diffusion of PVL has been found in the literature.

4.1.6 Poly ω-pentadecalactone (PPDL)

PPDL is chemically similar to high density polyethylene (HDPE), as shown in Figure 4.1 (d). Currently, there is no commercially available PPDL in the market, but only from lab-scale synthesis, which was synthesized by ring-opening polymerization [155, 156]. The synthesized polymer has a glass transition temperature of $-27\,^{\circ}\mathrm{C}$ and a melting temperature of $97\,^{\circ}\mathrm{C}$. PPDL also possesses decent mechanical properties, e.g. Young's modulus greater than $300\,\mathrm{MPa}$ and elongation at break longer than 500%, which is not only dependent on molecular weight, but also on temperatures [157]. HDPE has Young's modulus of $560\,\mathrm{MPa}$ and elongation of 690% according to ASTM D882 (DOW™ DMDA-8904 NT 7 High Density Polyethylene Resin). Therefore, PPDL is also called PE-like polyester, as it is chemically and mechanically similar to PE.

However, compared with HDPE, PPDL is not at all widely studied. Gazzano et al. revealed the dimensions of unit cell of crystal: a = $0.749\,\mathrm{nm}$, b = $0.503\,\mathrm{nm}$ and c (fiber axis) = $2\,\mathrm{nm}$ [158]. The unit cell is pseudo-orthorombic monoclinic. PPDL chains adopt the planar conformation in the crystals, and so does HDPE [159].

The melting behaviors of PPDL were studied by Cai and co-workers [160]. Unlike the other aliphatic polyesters (PGA, P4HB, PVL and PBS), PPDL does not show multiple melting peaks during the melting process observed by DSC.

Cai et al. also determined $\Delta H_{\mathrm{m,100}}$ of PPDL, by the extrapolation of the melting enthalpy to the specific volume of 100% crystalline PPDL, which is $227\,\mathrm{J\,g^{-1}}$ [160]. Skoglund et al. reported the possible $\Delta H_{\mathrm{m,100}}$ of $223\,\mathrm{J\,g^{-1}}$ and $264\,\mathrm{J\,g^{-1}}$ [161], the original literature is not available. Lebedev and Yevstropov reported $\Delta H_{\mathrm{m,100}}$ of $56\,\mathrm{kJ\,mol^{-1}}$, which was the calculation based on the heat capacity measured by DSC, roughly $233\,\mathrm{J\,g^{-1}}$ [162]. They also reported that PPDL has an equilibrium melting temperature of $370\,\mathrm{K}$. Cai et al. used linear and non-linear Hoffmann Weeks plots to extrapolate melting temperature to obtain $T_{\mathrm{m}}{}^{0}$, $101\,^{\circ}\mathrm{C}$ and $109.3\,^{\circ}\mathrm{C}$, respectively [160].

Cai et al. reported that PPDL has d_{c} of 10-13 nm based on 1D correlation function analysis of SAXS measurement [157]. Focarete et al. reported that PPDL has a crystallinity of 64 and 54% by the combination of melting enthalpy measured from DSC measurement and $\Delta H_{\mathrm{m,100}}$ value from the literature and WAXS measurement, respectively [155].

4.2 AA-BB aliphatic polyesters

4.2.1 Polybutylene Succinate or Poly Tetramethylene Succinate (PBS or PTMS)

Introduction

PBS was launched in 1993 as Bionolle™. The product is now available from PTT MCC Biochem under the trade name of BIOPBS [163]. Its chemical structure is illustrated in Figure 4.1 (g). The material is synthesized by polycondensation of succinic acid and butanediol [164]. It has T_g of $-30\,°C$ and T_m of $115\,°C$, which is not significantly lower than T_m of HDPE (PTT specification of FZ91). The synthesized material possesses comparable mechanical properties with HDPE [26]. It is even possible to fine-tune some of the mechanical properties by blending PBS with PLLA, which further narrows down the gap of mechanical properties between HDPE and PBS [25, 165]. In addition, PBS can easily undergo biodegradation in compost [166]. Therefore, this synthetic biodegradable polymer is considered to be a good candidate for replacing HDPE in many applications, especially in packaging applications [25], to tackle plastic waste issues.

Crystalline structure

PBS possesses polymorphism. A number of studies showed that PBS undergoes a transition from α form crystals to β form crystals under strain and relaxation [167, 168]. α form crystals have the unit cell dimensions: a = 0.523 nm, b = 0.912 nm, c (fiber axis) = 1.090 nm [169], and β form crystals have the unit cell dimensions: a = 0.584 nm, b = 0.912 nm, c (fiber axis) = 1.186 nm. The polymer chains adopt the planar chain conformation in both forms of crystals. In this study, the focus is only on α form crystals. The fully crystalline α form crystal has a density of $1.34\,\mathrm{g\,cm^{-3}}$, while the fully amorphous PBS has a density of $1.18\,\mathrm{g\,cm^{-3}}$ [170].

Kinetics and thermodynamics of crystallization of PBS

Miyata et al. studied the growth rate of spherulite at different isothermal crystallization temperatures, the rate increases to more than $10\,\mathrm{\mu m\,min^{-1}}$ when the isothermal crystallization temperature decreases from 110 to $90\,°C$ [170]. Papageorgiou et al. demonstrated that the crystallization rate of PBS increases quickly with decreasing isothermal crystallization temperatures according to DSC measurements, and they only had access to half of the "bell shape" curve [171]. They also illustrated that PBS shows multiple melting peaks during heating according to DSC measurements [171]. $\Delta H_{m,100}$ of PBS was determined by different researchers by different methods: the density method $(200\,\mathrm{J\,g^{-1}})$ [170], the combination of DSC and WAXS $(210\,\mathrm{J\,g^{-1}})$ [171], the combination of DSC and NMR $(183\,\mathrm{J\,g^{-1}})$ according to Chapter

5. The equilibrium melting temperature of PBS, mostly determined by Hoffmann Weeks plot, ranges from 122 to 135 °C [172–174].

Semicrystalline morphology and ICD

Papageorgiou et al. reported that PBS has a crystallinity of 35-40% from 80-95 °C based on their WAXS measurements [171]. Xu et al. showed that PBS has a crystalline layer thickness of 4.5 nm at 100 °C, based on the analysis of the interface distribution function of SAXS result [173]. In addition, they found no crystal thickening during isothermal crystallization. Schick et al. demonstrated that PBS has a narrow distribution width of d_c, between 3.2 and 4.5 nm, at 100 °C, which was determined by the combination of the results from flash DSC technique and other thermodynamic parameters from the literature [175]. In Chapter 5, it is revealed d_a, d_c and their distribution width (σ_a, σ_c) of PBS at different crystallization temperatures by SAXS measurement. PBS forms greater d_a (around 6.5 nm) than d_c (around 4.3 nm) and greater distribution width of d_a than that of d_c. Chapter 5 shows that PBS does not have measurable ICD in crystalline regions according to NMR T_1- and T_2-relaxation measurements.

Chapter 5

PBS, a crystal-fixed polymer

5.1 Introduction

Based on our recent studies [47,48], we proposed that semicrystalline polymers exhibit different morphological features depending on the existence of intracrystalline chain diffusion (ICD) and the difference between the timescale of ICD ($\langle \tau_c \rangle$) and crystal growth (τ_{lc}). When $\tau_{lc} \geq \langle \tau_c \rangle$, semicrystalline polymers show the following morphological features: $d_c > d_a$ and $\sigma_c > \sigma_a$. We call the polymers crystal-mobile polymers. d_c and d_a are average crystalline and amorphous layer thicknesses, respectively; σ_c and σ_a are their corresponding distribution widths. When $\tau_{lc} < \langle \tau_c \rangle$, semicrystalline polymers show different morphological features: $d_c \leq d_a$ and $\sigma_c \leq \sigma_a$. We call these polymers crystal-fixed polymers. Additionally, these two types of polymers show different ways to stabilize their crystals during heating: the crystals of crystal-mobile polymer thicken to gain stability, while the crystals of crystal-fixed polymer melt and recrystallize to form more stable crystals [176]. As the studies were carried out in three model polymers, we aim to check the generality of our proposals in this chapter, by extending our studies further into a biodegradable aliphatic polyester, PBS (Polybutylene Succinate) [166]. PBS is commercially available and is replacing PE in a few applications because it has similar thermal properties and its mechanical properties are not substantially inferior to those of PE, and, more importantly, it is more environmentally friendly [26,177,178]. PE, the most consumed polymer because of its superb thermal and mechanical properties [178, 179], is a crystal-mobile polymer [52, 180], but it is not well recyclable nor biodegradable [181]. Compared with PE, PBS is, however, still not widely studied and there is no quantitative study of intracrystalline chain diffusion and semicrystalline morphology (cf. Chapter 4), both of which are essential for the understanding of the difference in mechanical properties (our focus is on mechanical modulus) between PE and PBS .

Therefore, in this chapter, we present an experimental study to probe the potential ICD of PBS by a combination of solid-state NMR techniques with a SAXS-based

analysis of the complete semicrystalline morphology. The combination of these different robust methods was used to determine the crystallinity and its dependence on temperature. In addition, we provide a more reliable value for the enthalpy of melting or the extrapolated enthalpy of melting of a hypothetical 100% crystalline sample ($\Delta H_{m,100}$).

These results were published in the reference [67]. The text below was slightly modified based on the reference to suit the content of this dissertation. The NMR experiments in the chapter were carried out by Afiq Anuar from the solid-state NMR group headed by Prof. Kay Saalwächter. We provided a sufficient description of NMR results to support our argument. For a more in-depth understanding of NMR results, please refer to the references [67, 71–73]. At the end of this chapter is an appendix (Section 5.6) containing all the necessary information and raw data for the main text.

5.2   Material

We used a commercial-grade polybutylene succinate (FZ91) from PTT MCC Biochem Co., Ltd. with molecular weight $M_n = 40\,850\,\mathrm{g\,mol^{-1}}$, $M_w = 143\,400\,\mathrm{g\,mol^{-1}}$ ($PDI = 3.5$) as measured by GPC in dichloromethane with polystyrene calibration.

5.3   Result and discussion

5.3.1   PBS is a crystal-fixed polymer confirmed by NMR, SAXS and POM

To determine if PBS is a crystal-fixed polymer, we need to compare the timescale of possible ICD, τ_c, with the layer crystallization time, τ_{lc} [47]. To study fast molecular dynamics on the time scale of μs in the crystalline fraction of PBS, we performed ^{1}H NMR-free induction decay (FID) measurements. In addition, these measurements allow us to determine the crystallinity, which we discuss separately below. After isothermal crystallization at $100\,°\mathrm{C}$, the sample was cooled to $30\,°\mathrm{C}$ and heated stepwise to $115\,°\mathrm{C}$. At each temperature, an FID measurement was taken and the normalized crystal fraction was extracted according to the procedure described in Chapter 3. The resulting FIDs for the crystalline fractions are shown in Figure 5.1. All curves show no significant changes with temperature. The temperature independence of the curves indicates the absence of ICD on the time scale of the method ($\approx 0.2\,\mathrm{ms}$) [72]. If there was relevant ICD, we would observe temperature-dependent changes in the shape of the curves reflecting the increasingly fast molecular dynamics, where $\langle \tau_c \rangle(T)$ typically follows an Arrhenius dependence [47].

As no fast ICD was detected in PBS, we now need to address potentially slower motions up to the scale of seconds. Exchange-NMR methods relying on the reorientation of the ^{13}C Chemical-Shift Anisotropy (CSA) tensor, as used in our previous
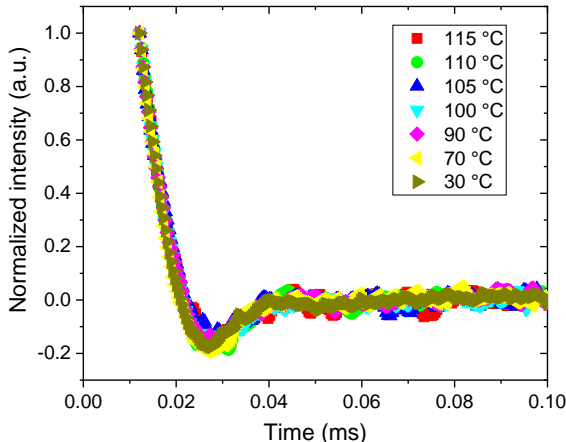
Figure 5.1: Normalized ^{1}H NMR-FID curves of the crystalline fraction of PBS crystallized at $T_c = 100\,°C$ measured at different temperatures as indicated in the legend. The fluctuations at larger times reflect the noise level. Note that data below 0.012 ms are missing due to the instrument dead time. The figure is reproduced from the reference [67].

work focusing on poly(oxymethylene) [48], are not applicable for PBS. The reason is the regularity of the crystal structure, specifically the all-trans rather than helical conformation, where the translation by one monomer unit places all atoms in crystallographically equivalent positions [169]. Therefore, we probe the diffusive long-range ICD of PBS, which is based on the possible detection of monomer exchange between the crystalline and amorphous regions. This can be achieved by observing an exchange between ^{13}C isotropic chemical shifts related to the two regions, provided they are distinguishable [74], and by ^{13}C T_1-relaxation [74, 77].

Distinguishing the resonances (chemical shifts) from crystalline and amorphous regions was achieved by ^{13}C spectra under Magic Angle Spinning (MAS) condition. The corresponding results are shown in Figure 5.2 (a). The red and blue dashed lines are the crystalline (subscript c) and the amorphous (subscript a) resonances from ^{13}C spectra, respectively. The total resonances of crystalline and amorphous regions are illustrated by the black solid curve. Please refer to the reference [67] for detailed explanations of the technique.

Based on the observed ^{13}C spectra, the well-separated intense peak b_c was chosen to probe its T_1-relaxation and thus assess potential ICD. The detailed deconvolution of the resonance peaks can be found in Appendix Figure 5.1. The T_1 decay curves of b_c for two different temperatures (30 and $90\,°C$) are shown in Figure 5.2 (b). If there is the presence of ICD, a monomer diffusion from the crystalline region into the amorphous region is expected. This diffusion results in a fast and linear decay of ^{13}C

signal with square root time scale ($\sqrt{t}$) in a short time period [77], e.g. approximately less than 1 s. However, in Figure 5.2 (b), the T_1-relaxation curves of peak b_c show no linear dependence on $\sqrt{t}$ ($T_1 < 1$ s) at both temperatures, which implies the absence of ICD in PBS up to the timescale of about 1 s.

PBS is thus similar to the previously studied PCL, which was shown to be a crystal-fixed polyester [182]. To prove the robustness of our T_1 relaxation measurement, the same measurement was also carried out on PCL (Appendix Figure 5.1 (c)), no monomer diffusion is found as well.

(a)

(b)
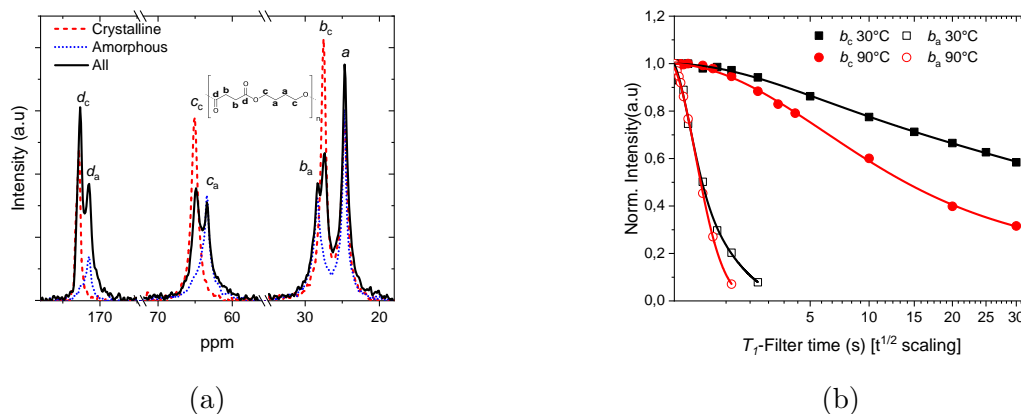
Figure 5.2: (a) Comparison of ^{13}C spectra: total contribution in black, the amorphous (subscripts a) and crystalline (subscripts c) contributions of ^{13}C spectra are in blue and red, respectively. (b) T_1 relaxation decay vs. the square root of the waiting time of peak b_c at 30 and 90 °C. The solid lines are biexponential fits (see Appendix Table 5.1 for the detailed results). The amorphous-phase decays for resonance b_a are included only for comparison. The figures are reproduced from the reference [67].

The layer crystallization time τ_{lc} can be estimated from the spherulitic growth velocity μ according to Equation 5.1 [47].

$$\tau_{lc} = \frac{5\mathring{A}}{\mu} \tag{5.1}$$

We measured μ of PBS during isothermal crystallization for different crystallization temperatures T_c. μ decreased with increasing T_c, accordingly τ_{lc} increased, as shown in Figure 5.3. The orange straight line in Figure 5.3 (b) corresponds to the measurement threshold of τ_c estimated by NMR; τ_{lc} is lying well below this line for all T_c. Based on our previous results on PEO and PCL, we would therefore expect that the semicrystalline morphology of PBS shows the typical morphological features of a crystal-fixed polymer, i.e. a well-defined crystal thickness and a broad distribution for the thickness of the amorphous regions [48].

(a)

(b)
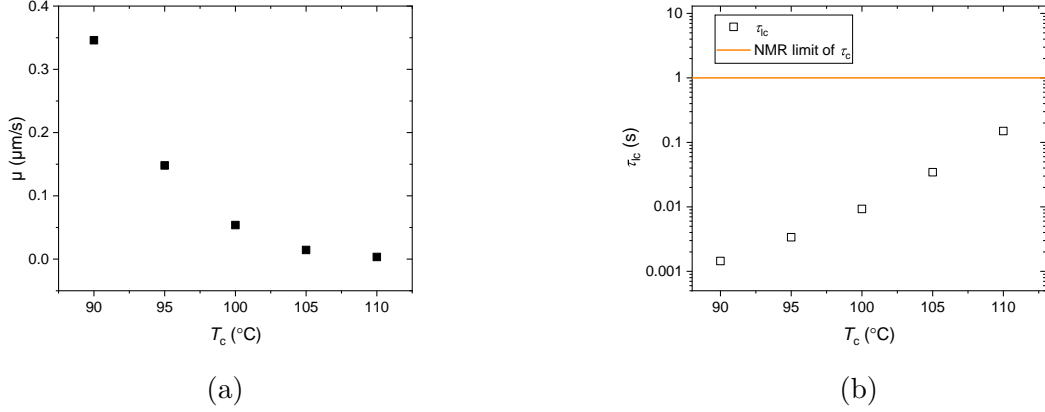
Figure 5.3: (a) Crystal growth velocity μ of PBS vs. crystallization temperature. (b) Corresponding layer crystallization time (τ_{lc}) and lower bound for the jump correlation time ($\langle\tau_c\rangle$) as a function of temperature. The figures are reproduced from the reference [67].

To characterize the semicrystalline morphology of PBS, we performed in-situ SAXS measurements during isothermal crystallization over a broad range of crystallization temperatures. Using a one-dimensional stack model for analysis (cf. Chapter 3), we determined the mean thickness of the crystalline and amorphous layers, d_c and d_a and their distribution widths, σ_c and σ_a. The results are shown in Figure 5.4. The Porod constant P is proportional to the specific crystalline-amorphous interface and can, therefore, be used to follow the increase of crystallinity during the measurement (cf. Chapter 3). The time at which 80 % of the final value was reached is marked by dashed vertical lines to indicate the transition from primary to secondary crystallization. As usual, the primary crystallization slows down strongly with increasing T_c. While d_c remains essentially unchanged during the whole course of crystallization, there is a reduction of d_a, which is most likely caused by the growth of additional crystals in larger amorphous regions. Note that the distribution width for the crystal thickness σ_a is larger than the corresponding value for the amorphous regions, σ_c. Based on the results in Figure 5.4 (c), we obtained the volume crystallinity according to Equation 5.2.

$$X_{c,volume} = \frac{d_c}{d_c + d_a} \cdot 100\%$$ (5.2)

The mass crystallinity can be determined by taking the density of the crystalline and amorphous regions into account.

$$X_{c,mass} = \frac{\rho_c \cdot d_c}{\rho_c \cdot d_c + \rho_a \cdot d_a} \cdot 100\%$$ (5.3)

Here $\rho_c = 1.34\,\mathrm{g\,cm^{-3}}$ is the density of the crystalline regions and $\rho_a = 1.18\,\mathrm{g\,cm^{-3}}$ is the density of amorphous regions [170]. Both crystallinities are listed in Table
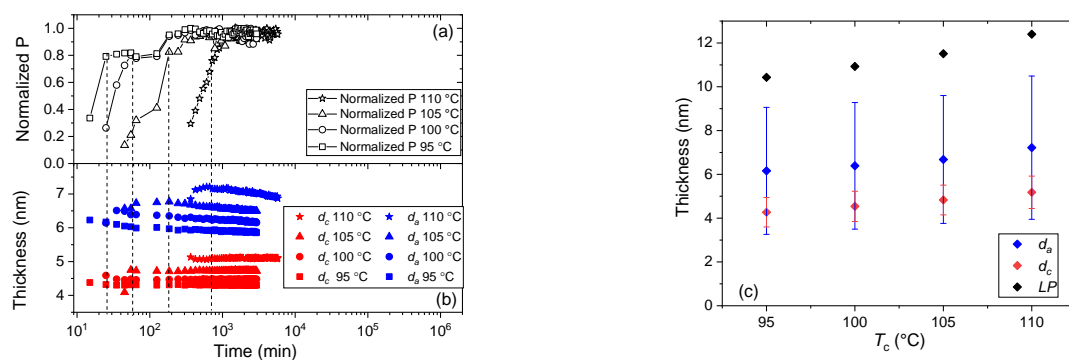
Figure 5.4: (a) Porod parameter P and (b) thickness of crystalline d_c and amorphous d_a layers during the course of isothermal crystallization at different temperatures (T_c = 95, 100, 105 and 110 °C). (c) d_c, d_a and long period LP vs. crystallization temperature T_c, data obtained from the endpoint of each isothermal process in (b). Error bars indicate the distribution widths σ_c and σ_a. The figures are reproduced from the reference [67]. The detailed analysis of each data in (c) are shown in Appendix Figures 5.4, 5.5, 5.6 and the figure in Chapter 3.

5.1 together with the crystallinity measured by ^{1}H NMR-FID, which was calculated according to Chapter 3.

Table 5.1: Volume crystallinity $X_{c,volume}$ and mass crystallinity $X_{c,mass}$ as measured by SAXS and NMR, melting enthalpy ΔH_m from DSC (cf. below), and the average melting enthalpy of 100% crystalline PBS, $\Delta H_{m,100} = \Delta H_m / X_{mass}$ calculated from all shown values.

T_c (°C)	SAXS $X_{c,volume}$ (%)	SAXS $X_{c,mass}$ (%)	NMR $X_{c,mass}$ (%)	ΔH_m by DSC (J g^{-1})	$\Delta H_{m,100}$ (J g^{-1})
95	42	45	41	77	
100	42	45	42	79	183±8
105	41	44	42	80	

The agreement between the crystallinities determined by SAXS and NMR is reasonable and within expectations, given the fact that the two methods rely on different principles. While SAXS measures density, the NMR-based FID deconvolution is based on mobility contrast. Additionally, the NMR analysis relies on a three-phase model, where Table 5.1 shows the value for the crystalline phase only. Based on the combined values, an estimate for the enthalpy of melting can be given, as discussed below, together with the DSC measurements. Our values for d_c are consistent with

the available values in the literature. These are SAXS-based values from Xu et al. and an indirect estimate based on sophisticated DSC measurements and selected literature values for the enthalpy of melting, the equilibrium melting temperature and the free energy of the fold surface of lamellar crystals [173, 175]. All of our results are consistent with our previous conclusions about the general morphological features of crystal-fixed polymers: A well-defined, relatively small crystal thickness d_c, absence of any observable crystal thickening, crystallinity X_c below 50%, greater values for σ_a than σ_c, while d_a and d_c show values of the same order of magnitude [47, 48].

5.3.2   Melting behavior and enthalpy of melting
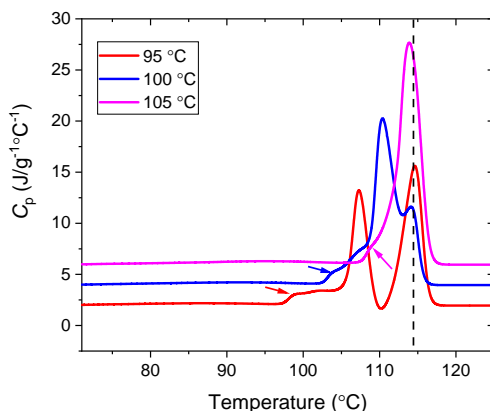
Figure 5.5: Heating scans of PBS at $10\,\mathrm{K\,min^{-1}}$ after isothermal crystallization at different temperatures (T_c) as indicated in the legend. The onset of melting is pointed out by arrows. The dashed line illustrates the approximately constant value of the final melting peak. The measurement for $T_\mathrm{c} = 100\,°\mathrm{C}$ and $105\,°\mathrm{C}$ were shifted vertically. The figure is reproduced from the reference [67].

With the help of the known values of the crystallinity determined above, measurements of the enthalpy of melting of semicrystalline samples can be used to determine the extrapolated enthalpy of melting of a hypothetical 100% crystalline sample. Figure 5.5 shows heating scans of PBS after isothermal crystallization at different temperatures (T_c). As observed before [171, 172, 183], PBS shows multiple melting caused by melting peaks and recrystallization, as it is typical for crystal-fixed polymers within a suitable parameter range [176]. The onset of melting, indicated by arrows, is related to the stability of the crystals directly after crystallization. Accordingly, this feature shifted to higher temperatures with increasing crystallization temperature, while the final melting peak as a result of reorganization during heating by (repeated) melting and recrystallization appeared more or less at the same temperature, independent of T_c.

To determine the melting enthalpies ΔH_m, we extrapolated the heat capacity (c_p) from the molten state above $120\,°\mathrm{C}$ to T_c as a base line and then integrated the heat capacity from T_c to $120\,°\mathrm{C}$ for each T_c. Division by the mass crystallinity gives an estimate for $\Delta H_\mathrm{m,100}$. Note that the value $\Delta H_\mathrm{m,100}$, is the enthalpy of melting at the temperature of melting, i.e. around $115\,°\mathrm{C}$, not at the equilibrium melting temperature. The mean value is $\Delta H_\mathrm{m,100} = 183\,\mathrm{J\,g^{-1}}$, with a standard deviation of $8\,\mathrm{J\,g^{-1}}$. This value is comparable but lower than those reported by other researchers of $200\,\mathrm{J\,g^{-1}}$ [170] and $210\,\mathrm{J\,g^{-1}}$ [171]. The latter value was determined in a similar way as above from the combination of a determination of the enthalpy of melting by DSC

and crystallinity, in this case, by WAXS. Given the limited precision of crystallinity values determined by WAXS, we believe that our value is more reliable. A third value of $110.3\,\mathrm{J\,g^{-1}}$ is often cited in the literature with reference to Chapter 5 of the reference [184] without giving a detailed derivation. $\Delta H_{m,100}$ itself is not given in there. Given the experimental results, this value can obviously be discarded.
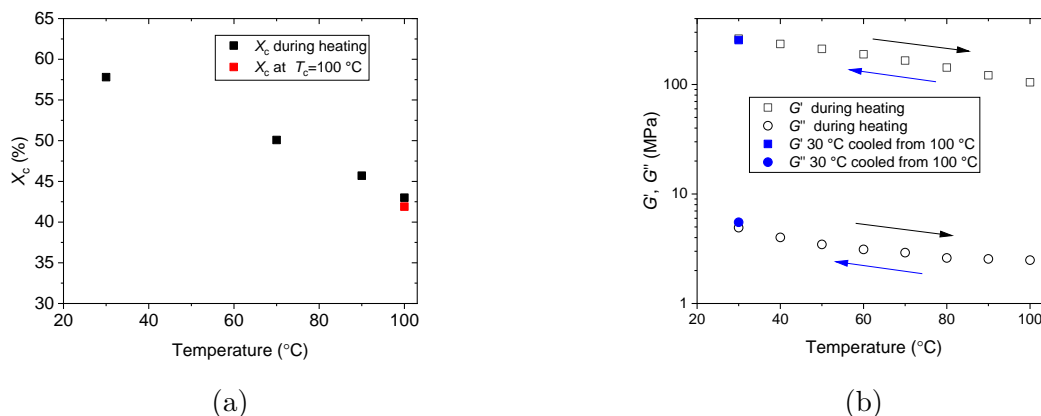
5.3.3 Temperature-dependent crystallinity and mechanical modulus

Figure 5.6: (a) Mass crystallinity (X_c) of PBS ($T_c = 100\,°\mathrm{C}$) measured by ^{1}H NMR-FID at different temperatures below T_c. The measurement at the end of the isothermal crystallization is represented by the red square. The sample was then cooled to $30\,°\mathrm{C}$ and the data shown as black symbols were acquired during heating. (b) G' and G'' vs. temperature ($10\,\mathrm{rad\,s^{-1}}$, 0.1% strain). The externally crystallized sample ($T_c = 100\,°\mathrm{C}$) was also measured during heating (black squares). A final measurement was taken after subsequent cooling at $30\,°\mathrm{C}$ (blue symbols). The figures are reproduced from the reference [67].

A major motivation to characterize and understand the morphology of semicrystalline polymers is due to the fact that the mechanical properties, and specifically the modulus depend strongly on the crystallinity [28, 185]. Based on specific DSC experiments, PBS is reported to crystallize further upon cooling below T_c, even if the previous isothermal crystallization at elevated temperatures was complete [186, 187]. It is therefore of interest for practical application, e.g in packaging [188], to determine the crystallinity and the mechanical modulus in the temperature range between T_c and room temperature. While in DSC the changes in crystallinity are difficult to identify and separate from the heat capacity signal (Appendix Figure 5.2), they show up clearly in the ^{1}H NMR-FIDs.

The resulting temperature-dependent crystallinity is shown in Figure 5.6 (a). After an isothermal crystallization at $T_c = 100\,°\mathrm{C}$, the sample was cooled to $30\,°\mathrm{C}$

and subsequently heated step-wise back to $100\,°C$ with NMR measurements at each holding temperature. In this temperature range, the crystallinity changes more or less reversibly by a factor of about 1.4. To confirm that the immobile phase formed during cooling is indeed crystalline, we performed WAXS measurements at selected temperatures, which show, in fact, an increase in the intensity of Bragg reflections at low temperatures (Appendix Figure 5.3 (a)). Given the specific semicrystalline morphology, i.e. $d_a > d_c$ and large σ_a, one would expect that this additional crystallization follows the scenario of insertion crystallization, i.e. the thin crystals formed upon cooling grow into the larger amorphous regions. This picture is qualitatively consistent with observed changes in the SAXS data, shown in Appendix Figure 5.3 (b). A similar effect was observed before for PCL but weaker because of the smaller temperature difference between T_{room} and T_c [47].

To investigate the effect of the observed changes in crystallinity on the linear mechanical properties, we measured the dynamic shear modulus over the same temperature range at a fixed frequency. Samples with a similar thermal history as above (isothermal crystallization, $T_c = 100\,°C$) were heated step-wise from 30 to $100\,°C$ during the measurement, and then cooled again to $30\,°C$ to confirm the reversibility of the measured values. The resulting values for G' and G'' are shown in Figure 5.6 (b). The storage modulus increases by a factor of about 2.5 during cooling over the relevant temperature range and the change in G'' is similar, while the absolute value is more than two orders of magnitude smaller. This behavior confirms that the temperature-dependent changes are not caused by any relaxation. The results show that the additional crystallization upon cooling leads to a significant reinforcement of the material, which, on the other hand, also leads to a softening at elevated temperatures, which might be relevant for specific applications. We would expect that these are general effects for crystal-fixed polymers.

5.4   Conclusion

In conclusion, we could show that PBS has to be classified as a crystal-fixed polymer without or, at most, very slow intracrystalline chain diffusion, for which reorganization of the semicrystalline morphology plays no role during crystallization. In agreement with our hypothesis, PBS shows the typical morphological features that we previously attributed to this class of polymers, namely: a relatively small crystal thickness d_c with a weak dependence on crystallization temperature, absence of any discernible crystal thickening during isothermal crystallization; low crystallinity ($X_c < 50\%$), greater values for the distribution width σ_a of the amorphous regions than that for the crystalline layers σ_c. Similar to PCL, the model polymer from our previous studies, melting of the original crystals happens only slightly above T_c and during further heating, a complicated melting and recrystallization process occurs, leading to a final melting temperature largely independent on the crystallization temperature.

Making use of the large temperature range between crystallization/melting and

room temperature, we could furthermore show that the crystallinity increases significantly during cooling by insertion crystallization, leading to a rather strong increase in mechanical modulus [47, 48, 176]. Presumably, these are general effects for crystal-fixed polymers.

Based on the relatively precise and consistent values obtained for the crystallinity by two different experimental methods, we could extrapolate the measured value for the enthalpy of melting to the value of a 100% crystalline sample, $\Delta H_{m,100} = 183 \pm 8\,\mathrm{J\,g^{-1}}$. Given the larger range of values for this quantity given previously in the literature, we believe that our value allows a more precise determination of the crystallinity based on simple DSC measurements.

With the decisive role of the intracrystalline chain diffusion for the morphology of semicrystalline polymers becoming more and more established, the question arises about which factors favor the existence and the time scale of such a dynamics. Polyesters promise to be interesting objects of study here, given the fact that e.g. PLA is known to exhibit ICD on an intermediate time scale [122, 123], although complete morphology is not yet revealed. ICD of other polyesters is rarely studied, and neither is their morphology. A deeper understanding of the semicrystalline morphology of this polymer family would also be of practical interest, as polyesters are promising replacements for commodity plastics because of their biodegradability and the fact that at least some of them are biobased.

5.5   Experimental details

This section is different from Experimental Method Chapter (Chapter 3), it contains only the detailed instrumental parameters and the sample treatments with the purposes of data reproduction.

Proton low-resolution NMR-FID

[1]H time-domain nuclear magnetic resonance (NMR) experiments at low field ($B_0 \approx$ 0.5 T) were performed on a Bruker minispec mq20 spectrometer with a proton frequency of about 20 MHz ($B_0 \approx 0.47$ T) using a static probe head with a wide temperature range realized by heated or cooled air flow. The temperature accuracy of the instrument is $\pm$ 1 K with a gradient of up to 0.5 K over the sample. We used a 90° pulse length of around 2.8 μs; the recycle delay (RD), i.e. the time between successive scans, was set to 2 to 3 s, sufficient for near-complete T_1-relaxation. Measurements and analyses were conducted as reported in our previous works [72, 73]. To overcome problems with the dead time of about 12 μs, we compared free induction decay (FID) signals detected directly after a 90° pulse with signals after a magic-sandwich echo (MSE). The latter avoids the dead time but features some loss of intensity, meaning that shape parameters are taken from the MSE-FIDs while component amplitudes are taken from the FIDs. The samples were always heated to 140 °C for 10 min to remove the thermal history and then cooled to different crystallization temperatures for isothermal crystallization. The step-wise heating for the measurement shown in Fig 5.6(a) was carried out with a rate of about 5 K min^{-1}, with an additional 10 min of equilibrium time before each NMR-FID measurement. A detailed analysis of FID measurement can be found in the previous publications [72, 189].

[13]C MAS spectroscopy

All ^{13}C spectra and data were recorded on 400 MHz Bruker Avance III spectrometers with [13]C Larmor frequency of 100.6 MHz using double- and triple-resonance magic-angle-spinning (MAS) probes at a spinning frequency of 10,000 $\pm$3 Hz. The pulse lengths on the ^{1}H and ^{13}C channels were around 3 μs. Cross-polarization (CP) spectra were recorded with contact times of 0.1 ms for crystalline-signal selection as well as 1.5 ms for maximum signal overall, using an RD of 5-7 s (shorter at higher temperature) for near-complete T_1-relaxation of the ^{1}H nuclei (being the source of polarization in CP). In contrast, ^{13}C direct polarization (DP) with short RD of around 1 s emphasizes the mobile/amorphous signals. For measurements of the [13]C T_1-relaxation decay, the pulse sequence of Torchia [71] featuring a z-filter on the ^{13}C channel after CP was used, utilizing peak deconvolution to faithfully separate the different resonances.

Small-angle X-ray scattering (SAXS)

SAXS measurements were performed on a Kratky compact camera (Anton Paar GmbH, Graz, Austria) equipped with an X-ray optics (AXO Dresden GmbH, Germany), a temperature-controlled sample holder, and a 1D detector Mythen2 R 1K (Dectris, Switzerland). As the camera has a slit focus, the data had to be deconvoluted. This was achieved by applying the desmearing algorithm by Strobl [190].

The PBS samples were quenched from the melt state (150 °C) to different isothermal crystallization temperatures in the Kratky camera. The exposure time for each measurement was 10 min.

The analysis of the SAXS data is based on the interface distribution function (IDF or K"(z)), originally introduced by Ruland [191]. The detailed analysis procedure is described in our previous publications [47, 50]. The corresponding examples of the analysis of our PBS sample can be found in Chapter 3, and Appendix Figures 5.4, 5.5, 5.6.

DSC

Differential scanning calorimetry was performed with a DSC 8000 from Perkin Elmer. The sample was heated to 150 °C to remove thermal history and quenched to different crystallization temperatures. After the completion of isothermal crystallization, the sample was cooled to -60 °C and heated to 150 °C at a rate of $10 \, \mathrm{K \, min^{-1}}$.

Rheology

The shear modulus was measured with a rheometer Ares G2 equipped with a heating chamber from TA instruments using a sample in stripe geometry (sample length between clamps 20 mm, width 10 mm, thickness 1.5 mm) at different temperatures but constant frequency of $10 \, \mathrm{rad \, s^{-1}}$ and 0.1% strain. Beforehand, the sample was isothermally crystallized at 100 °C in a rectangular mold (MeltPrep device) for 24 h, and then transferred to the rheometer at room temperature. The step-wise heating program for measurement shown in Figure 5.6 (b) was similar to that of ^{1}H NMR-FID measurement.

Optical Microscopy

Optical microscopy measurements were performed by using an Olympus BX51 microscope equipped with an Olympus XC30 camera allowing observation of the sample and recording of the images. A Linkam hot stage equipped with a Linkam TP 94 temperature controller and a Linkam LNP liquid nitrogen controller was used as the sample stage. We dissolved 103 mg PBS in 4 mL chloroform and placed one droplet of the solution on a cover glass, which was heated to 140 °C to remove the solvent and melt the PBS. Another cover glass was placed on top of PBS melt. For the measurements, the sample (PBS sandwiched between cover glasses) was placed on

the Linkam hot stage. We heated the sample to $140\,°\text{C}$ for $10\,\text{min}$ and then cooled it with a rate of $30\,°\text{C}\,\text{min}^{-1}$ to different temperatures for isothermal crystallization. The crystallization was directly monitored using polarized light optical microscopy. Olympus Stream Motion software was used to observe the camera view on a computer and to analyze the images.

5.6 Appendix

Table 5.1: Biexponential fit results of the ^{13}C T_1-relaxation decays.

polymer	temperature (°C)	cryst./am.	$T_{1,\text{short}}$ (s)	$T_{1,\text{long}}$ (s)	fraction $T_{1,\text{short}}$ (%)
PBS	30	cryst.	7.6	91.8	19
		am.	0.2	1.13	54
PBS	90	cryst.	11.0	93.7	64
		am.	0.07	0.39	5
PCL	30	cryst.	2.86	130.1	26
		am.	0.27	–	100

(a)

(b)

(c)
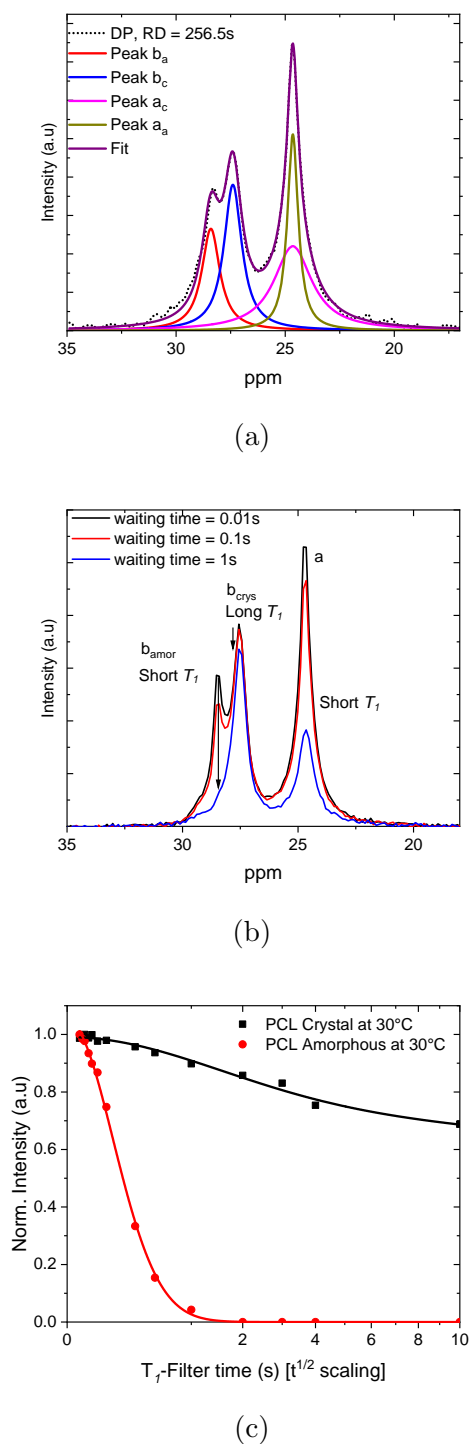
Figure 5.1: ^{13}C NMR details. (a) Illustration of the peak deconvolution on resonances b and a, revealing a different line width but almost identical shifts of the amorphous and crystalline signals of resonance a. (b) Individual spectra from the T_1-relaxation decay experiments, confirming the amorphous (short T_1) vs crystalline (long T_1) assignments. (c) T_1-relaxation decay data for a crystalline resonance of PCL at 30 °C to be compared with Figure 5.2 (b), showing overall similar phenomenology in PBS and PCL. The x-axis scaling in (b) and (c) corresponds to $\sqrt{t}$, which would give a linear decay if the process were diffusive. The figures are reproduced from the reference [67].
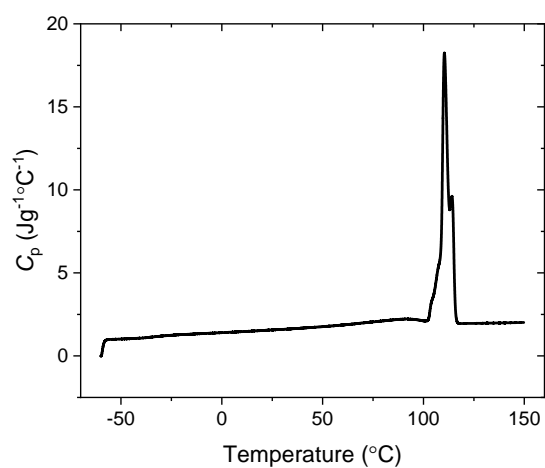
Figure 5.2: DSC heating curve ($T_c = 100\,°\text{C}$) as in Figure 5.5 of the main text but over the full temperature range. Any DSC signal due to the melting of additional crystals formed upon cooling below T_c is difficult to be separated from the background due to normal heat capacity. The figure is reproduced from the reference [67].

(a)   (b)
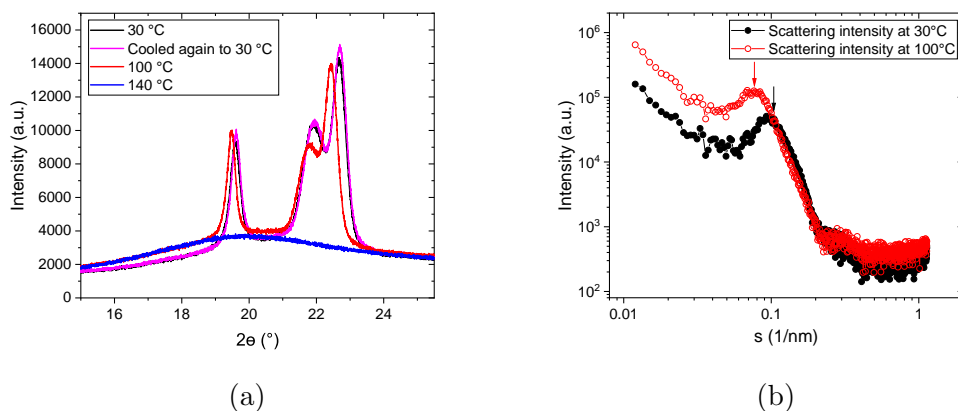
Figure 5.3: (a) WAXS intensity of PBS ($T_{\mathrm{c}} = 100\,°\mathrm{C}$) measured in $\theta - 2\theta$ geometry at PBS at different temperatures. (b) SAXS intensity of PBS ($T_{\mathrm{c}} = 100\,°\mathrm{C}$) at T_{c} and at room temperature. The figures are reproduced from the reference [67].

To confirm the increase of crystallinity upon cooling below the crystallization temperature, we performed WAXS and SAXS measurements. For WAXS experiments, the sample was crystallized at $100\,°\mathrm{C}$ externally in a MeltPrep device for 24 h. After transfer to the diffractometer the sample was measured at $30\,°\mathrm{C}$, $100\,°\mathrm{C}$, and then again at $30\,°\mathrm{C}$ to confirm reversibility. For comparison, a measurement in the melt state at $140\,°\mathrm{C}$ is shown. While a quantitative analysis is not straightforward due to the simultaneous change in intensity and position of the Bragg peaks and the underlying background and the fact that Bragg peaks at different temperatures are weakened by different Debye-Waller factors, it is qualitatively clear that the intensity of the Bragg reflections grows during cooling at the expense of the amorphous background indicating an increase in crystallinity.

The SAXS results also show changes upon cooling. The background at high q, caused by density fluctuations in the liquid phase, decreases consistently with the increase in crystallinity. The position of the minimum around $s \approx 0.2\,\mathrm{nm}$ reflecting the thickness of the crystallites remains nearly unchanged, while the position of the maximum indicated by arrows shifts to higher q, i.e. the long period takes on smaller values. These changes are typical for insertion crystallization, i.e. much thinner crystals grow into the larger amorphous regions in between already existing crystals. A quantitative analysis in terms of the lamellar stack model used for the measurements during isothermal crystallization is not appropriate in such a case as the distribution of crystal thickness develops a tail towards smaller values, which is difficult to catch the chosen model, although the changes show up qualitatively in the reduced mean long period.
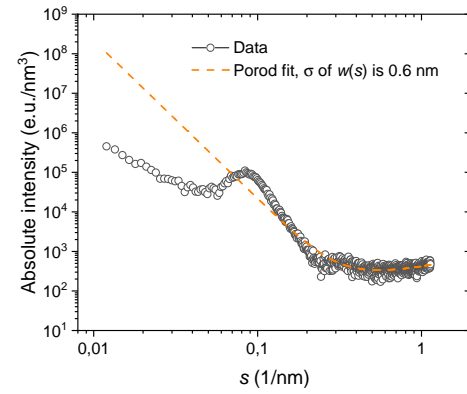
(a)
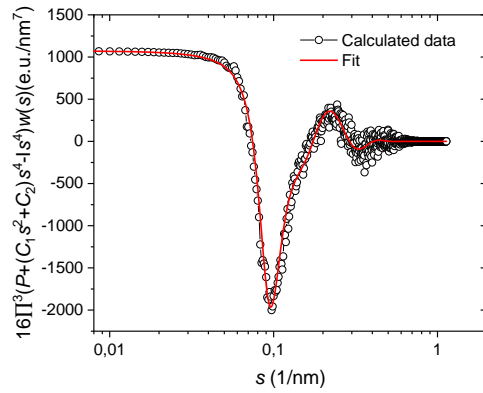
(b)
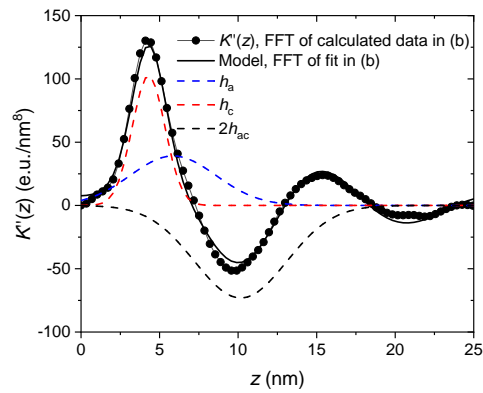
(c)

Figure 5.4: (a) I_{abs} and Porod fit of PBS, T_c=95 °C for 2945 min (b) $(-I_{abs} + Ps^{-4} + c_1 s^2 + c_2)s^4 w(s)$ and the fit according to our solution of PBS, (c) The cosine transformation of the fit and $(-I_{abs} + Ps^{-4} + c_1 s^2 + c_2)s^4 w(s)$ in (b) and its decomposition in three contributions (dashed lines) h_c, h_a and $2h_{ac}$
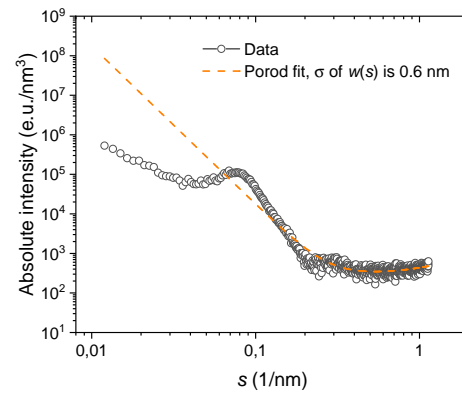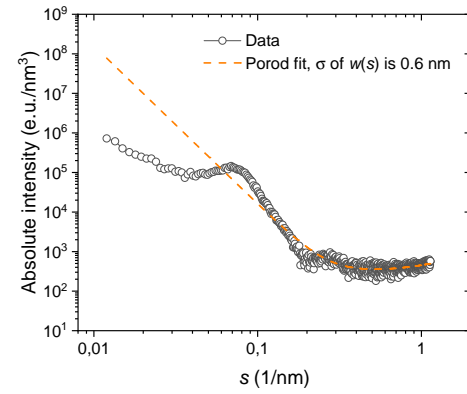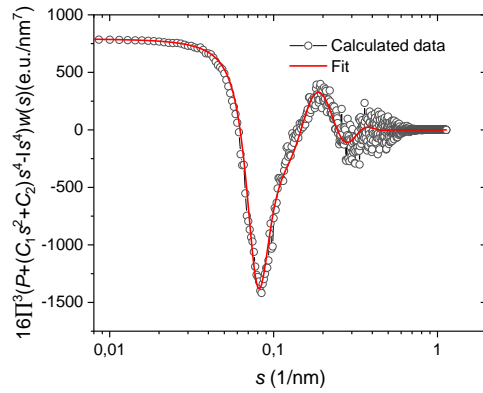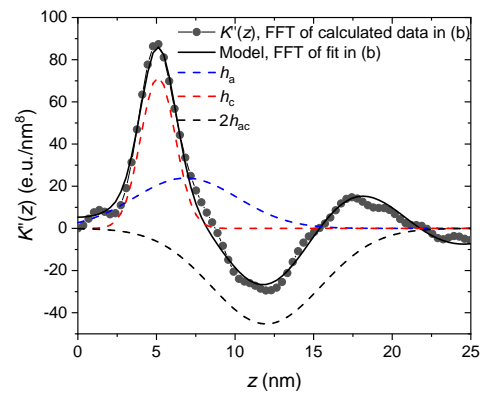
(a)
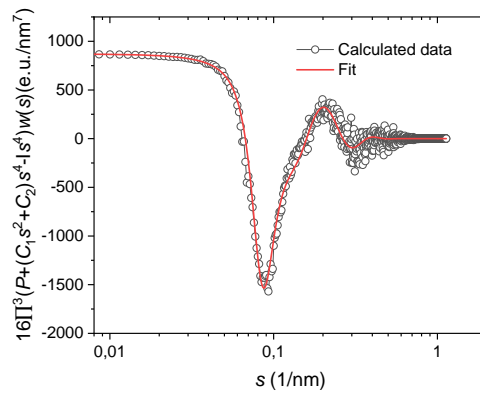
(b)
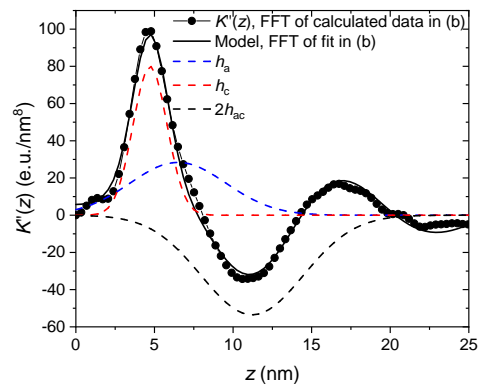
(c)

Figure 5.5: (a) I_{abs} and Porod fit of PBS, T_c=105 °C for 2945 min (b) $(-I_{abs} + Ps^{-4} + c_1s^2 + c_2)s^4w(s)$ and the fit according to our solution of PBS, (c) The cosine transformation of the fit and $(-I_{abs} + Ps^{-4} + c_1s^2 + c_2)s^4w(s)$ in (b) and its decomposition in three contributions (dashed lines) h_c, h_a and $2h_{ac}$

(a)

(b)

(c)

Figure 5.6: (a) I_{abs} and Porod fit of PBS, T_c=110 °C for 5765 min (b) $(-I_{abs}+Ps^{-4}+c_1s^2+c_2)s^4w(s)$ and the fit according to our solution of PBS, (c) The cosine transformation of the fit and $(-I_{abs}+Ps^{-4}+c_1s^2+c_2)s^4w(s)$ in (b) and its decomposition in three contributions (dashed lines) h_c, h_a and $2h_{ac}$

Chapter 6

P3HB, a crystal-mobile polymer

6.1   Introduction

Poly(3-hydroxybutyrate) (P3HB) is a biodegradable polyester, produced by microorganisms on an industrial scale [126]. The material possesses high elastic modulus and melting temperature (cf. Chapter 4). P3HB is able to replace commodity plastics in some applications, e.g. medical packaging and tissue engineering, but its applications are challenged by its brittleness (short elongation at break). The applications of P3HB are further limited by its detrimental embrittlement over time (elongation at break of products made of P3HB becomes shorter and shorter over time) [132, 133, 192]. The factors driving the embrittlement over time are considered to be either the physical aging of amorphous parts below their glass transition temperature (T_g) or secondary crystallization. Although P3HB has been already commercially available on the market for more than 30 years, its detailed semicrystalline morphology (crystalline (d_c) and amorphous (d_a) layer thickness and their distribution width, σ_c and σ_a) are still not complete (cf. Chapter 4). Xia and co-workers reported that P3HB did not possess measurable Intracrystalline Chain Diffusion (ICD) [142].

From our recent studies [47, 48], based on three model polymers, we propose that the semicrystalline polymers with measurable ICD (crystal-mobile polymer) show the typical morphological features: $d_c > d_a$, $\sigma_c > \sigma_a$, while the semicrystalline polymers without measurable ICD (crystal-fixed polymers) show: $d_c < d_a$, $\sigma_c < \sigma_a$. The measurable ICD refers to the timescale of ICD ($\langle \tau_c \rangle$) less than 1 s. When $\langle \tau_c \rangle$ is longer than 1 s, we consider ICD of a polymer is not measurable. The previous chapter (Chapter 5) successfully shows that our proposals are also valid for a commercially available AA-BB polyester, PBS (Polybutylene succinate). PBS shows no measurable ICD. It demonstrates the corresponding morphological features ($d_c < d_a$, $\sigma_c < \sigma_a$), as predicted by our proposals.

To check whether our proposals are further valid in polyesters and to provide complete information about semicrystalline morphology and ICD of P3HB, we extend our study to P3HB in this chapter. We reproduced the embrittlement of P3HB over

a period of aging time at a temperature far above T_g, in order to differentiate the effect of secondary crystallization from physical aging on the embrittlement of P3HB. The embrittlement was characterized by mechanical measurement (tensile test) and Dynamic Mechanical Analysis (DMA). The full semicrystalline morphology (d_c, d_a, σ_c and σ_a) was monitored and measured during the aging time by SAXS so that the missing information about semicrystalline morphology of P3HB is completely revealed. ICD of P3HB was investigated by variant NMR techniques: ^{1}H NMR-FID and [13]C Centerband-Only Detection of Exchange (CODEX). We find the presence of ICD in the crystalline P3HB. The activation energy of an α_c relaxation corresponding to ICD determined by ^{13}C NMR and DMA measurement, separately, is consistent with each other.

These results were recently published in the reference [76]. The text below is modified based on the reference to suit the content of this dissertation. At the end of this chapter, it is an appendix (Section 6.6) containing the necessary information to support the main text.

6.2   Material

P3HB without nucleating agent (P338 as pellets, with lot number 26T3380) was obtained from Biomer (Schwalbach, Germany). The polymer (P338) was reported to have an M_n of 130 kDa [193]. For other P3HB products from Biomer (P209 and P309) with similar M_n, the polydispersity (M_w/M_n) was determined to be around 4 [194]. P3HB is subjected to thermal degradation at and above its melting temperature [195]. In our hands, differential scanning calorimetry (DSC) experiments shown in Appendix Figure 6.1, illustrated the changes in the melting temperature upon repeated heating and cooling cycles, which may be taken as an indirect hint at sample degradation. To exclude such effects on our analyses, each measurement was performed with a new sample.

6.3   Result and discussion

6.3.1   Mechanical properties

In order to confirm the embrittlement of our P3HB sample over time, several mechanical measurements were conducted at room temperature. Stress-strain curves were utilized to observe storage effects on isothermally crystallized P3HB samples, as illustrated in Figure 6.1 and summarized in Table 6.1. In these measurements, the as-prepared sample was crystallized at 120 °C and then subjected to stress-strain measurement without aging. The crystallization temperature was chosen based on the DSC measurements (Appendix Figure 6.1). The strain at break (ϵ_B) of the as-prepared sample was 12.22%. 2 days of annealing at 60 °C leads to a reduction of ϵ_B to 7.18 %, which is further reduced to 6.46 % after 8 days. T_g of the amorphous phase
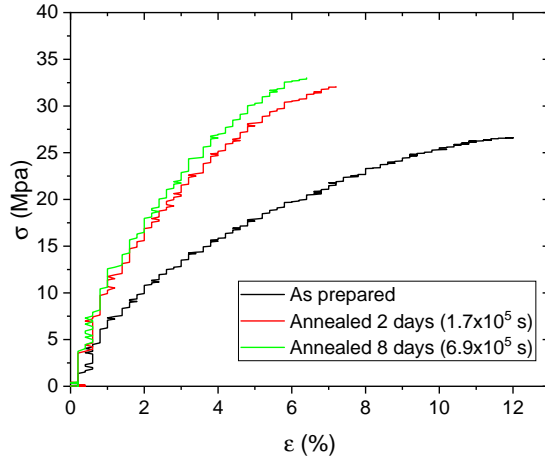
Figure 6.1: Exemplary stress-strain curves of P3HB, crystallized isothermally at 120 °C without and with annealing at 60 °C, all measured after cooling to room temperature within 5 min. The figure is reproduced from the reference [76].

Table 6.1: Strain at break (ϵ_B) and stress at break (σ_B) after different thermal treatments

Sample Treatment	ϵ_B (%)	σ_B (MPa)
As-prepared	12.22±0.62	26.06
Annealed 2 day at 60 °C	7.17±0.15	32.05
Annealed 8 day at 60 °C	6.46±0.38	33.00

of P3HB is reported in a range of about 0 to 27 °C [127–129], where the variation may be attributed to confinement effects in the small amorphous domains. Since our annealing temperature is well above this range, we take this as an indication that actual aging effects in still glassy amorphous domains are at least an unlikely cause of the embrittlement over time. Of course, the slow dynamics in the amorphous phase being close to T_g at ambient temperature, and even a slight increase related to the thickening of the crystalline lamellae, could well affect the overall brittleness.

Further DMA measurements were conducted during two days of annealing at 60 °C after isothermal crystallization at 120 °C, comparable to the conditions in Figure 6.1. Figure 6.2 (a) shows a slow increase and decrease of G' and G'' over time, respectively. The increase of G' reflects a stiffness increase that is consistent with the increase of the slope of the stress-strain curve in Figure 6.1.

Another important mechanical feature of P3HB can be seen from DMA temper-

ature sweeps. From such a data set, measured on a compression-molded specimen of non-isothermally crystallized P3HB, Figure 6.2 (b) illustrates the temperature effect at a fixed frequency of $0.1\,\mathrm{rad\,s^{-1}}$. The loss modulus G'' and $\tan\delta$ showed a broad peak starting from around $40\,^\circ\mathrm{C}$ that is typically observed in crystal-mobile polymers, being referred to as α_c-relaxation [47]. A detailed discussion, specifically the confirmation of the observation of actual α_c-relaxation through master-curve construction and the relation to NMR observations of ICD, will be presented below.

(a)   (b)
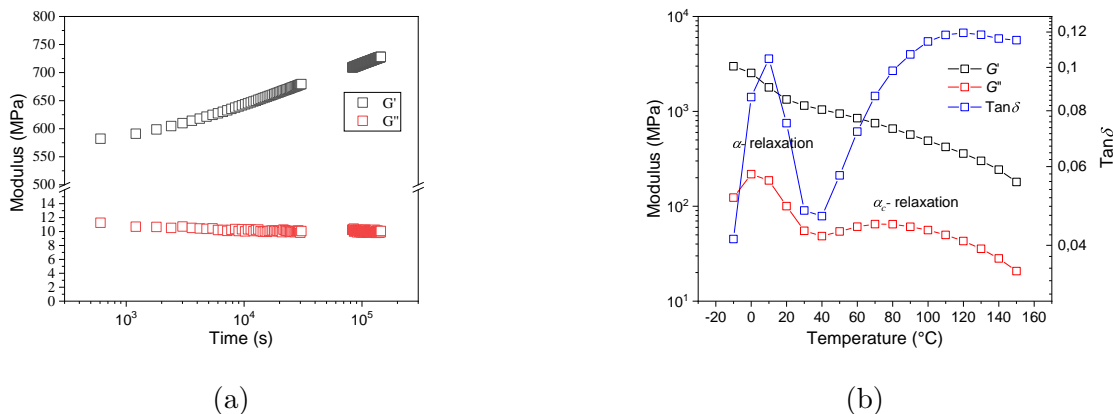
Figure 6.2: (a) G' and G'' measured by DMA during annealing at $60\,^\circ\mathrm{C}$, with a frequency of $10\,\mathrm{rad\,s^{-1}}$, a strain of 0.1%. There was a power outage during the aging experiment, which caused the gap of data both in G' and G''. The specimen was isothermally crystallized at $120\,^\circ\mathrm{C}$ for $1\,\mathrm{h}$ and then quickly cooled to room temperature and transferred to the DMA instrument (at $60\,^\circ\mathrm{C}$). (b) G' and G'' and $\tan\delta$ measured by DMA in the temperature range from -10 to $150\,^\circ\mathrm{C}$, with a frequency of $0.1\,\mathrm{rad\,s^{-1}}$ and strain amplitude of 0.1%. G'' and $\tan\delta$ show a sharp peak at around $0\text{-}20\,^\circ\mathrm{C}$, which refers to α relaxation. The specimen was non-isothermally crystallized at an estimated cooling rate of $5\,\mathrm{K}$. The figures are adapted from the reference [76].

6.3.2 Semicrystalline morphology

As P3HB embrittlement may be related to the change in crystallinity over time, SAXS was used to investigate the semicrystalline morphology of P3HB that was subjected to the same temperature profile as the samples studied mechanically. We are interested in the crystalline and amorphous layer thickness, d_c and d_a, respectively, as well as their distribution width, σ_c and σ_a, observed during isothermal crystallization at $120\,°C$ for about 1 hour and subsequent annealing at $60\,°C$ for 4 days.
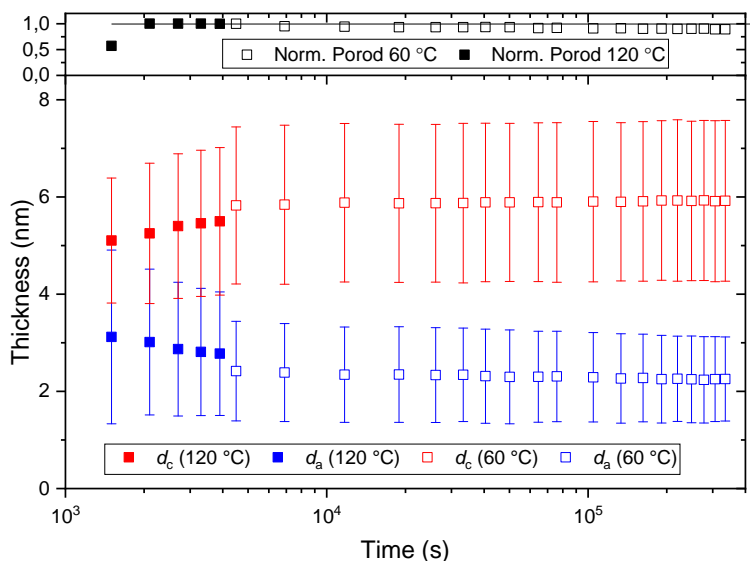
Figure 6.3: Crystalline (d_c) and amorphous (d_a) layer thickness during the course of isothermal crystallization at $120\,°C$ and during subsequent annealing at $60\,°C$ for 4 days. The horizontal dashed lines are here to guide the eye. Note that the "error bars" correspond to the width of the fitted thickness distributions, σ_a and σ_c. The upper panel shows the evolution of the normalized Porod parameter (Norm. Porod), confirming a constant interfacial area, thus, a constant number of lamellae. The solid dots represent the isothermal crystallization process at $120\,°C$; the hollow dots represent the aging process at $60\,°C$. The figure is adapted from the reference [76].

Figure 6.3 (the solids dots) shows the SAXS results of P3HB during isothermal crystallization at $120\,°C$. We observe that d_c and d_a are increasing and decreasing over time, respectively. The sample temperature was then reduced to $60\,°C$ to observe the presence of secondary crystallization via crystal thickening at a lower temperature, mimicking slow changes at room temperature on an accelerated timescale, as illustrated by the hollow dots in Figure 6.3. The data reveals an ongoing thickening of P3HB crystal lamellae even after about 4 days. We observe that d_c increases from 5.1

to 5.9 nm and d_a decreases by about the same amount, which results in an increase of the linear crystallinity SAXS $X_c = d_c/(d_c + d_a)$ from 0.62 to 0.72. Notably, the Porod parameter remains unchanged, confirming that the long period (LP), $LP = d_a + d_c$, is not changed.

As the long period stays constant at around 8.2±0.04 nm, it is an evidence of actual lamellar thickening rather than insertion crystallization. In the latter case, all structural parameters d_a, d_c and LP would rather decrease [67, 72]. Other important observations are broad σ_c and narrow σ_a, and σ_a is still narrowing, which, together with the high crystallinity, are the typical morphological features observed for the polymers possessing ICD [47, 48].

These changes may well be held responsible for the observed embrittlement, although we lack an explicit model that connects these morphology changes with brittle failure. Of course, there are other possibilities, e.g. through a higher confinement-induced T_g in the narrower amorphous gaps after aging/post crystallization [196–200], the change of the amount of tie chains and entanglements in the amorphous phase. To clarify the exact connection between morphology changes and embrittlement is out of the scope of this study.

6.3.3 Intracrystalline chain diffusion

From the results so far, we have strong indications of the presence of an α_c-relaxation (Figure 6.2 (b)), and the resulting ICD, constituting the origin of crystal thickening (Figure 6.3). These indications contradict the finding from Xia and co-workers [142], who reported there was the absence of an α_c-relaxation in P3HB. The α_c-relaxation is commonly attributed to helical jumps of the chains within the crystals [52], mediated by traveling defects [73]. The relevant timescale for this process is the jump correlation time $\langle \tau_c \rangle$, which is the average residence time of a monomer in a given crystal raster position and is normally characterized by NMR techniques.

The NMR experiments described in the chapter were carried out by Afiq Anuar from the solid-state NMR group headed by Prof. Kay Saalwächter. We provide a sufficient description of NMR results to support our argument. For a more in-depth understanding of NMR results, please refer to the references [72, 73, 75, 76].

To probe fast ICD ($\langle \tau_c \rangle < 200\,\mu s$), we performed temperature-dependent low-resolution ^{1}H NMR-FID measurement. If $\langle \tau_c \rangle < 200\,\mu s$, the shape of the crystalline components of FID curves would change with temperatures [72]. However, we do not observe any temperature-dependent changes, which indicates the absence of fast ICD (Appendix Figure 6.2). Therefore, $\langle \tau_c \rangle$ must exceed $200\,\mu s$ at any relevant temperature.

(a) (b)
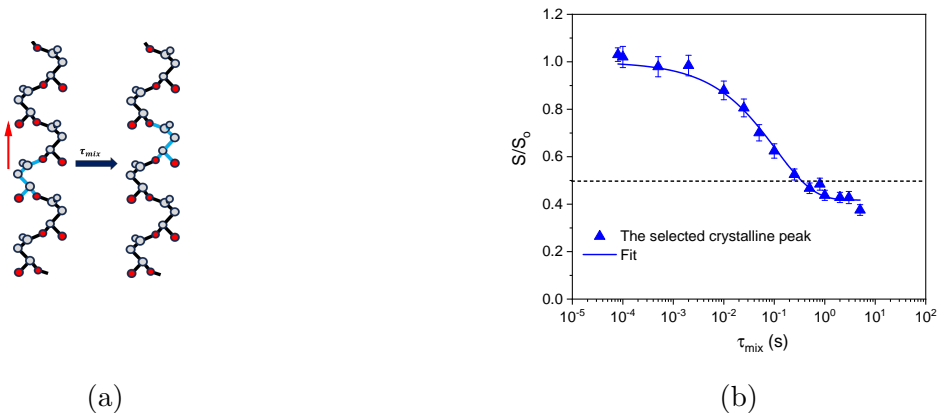
Figure 6.4: (a) Illustration of a helical jump in the P3HB crystal. The P3HB monomer, labeled in blue, jumps in the arrow direction (red) to a neighboring position, when τ_{mix} (waiting time) is long enough. (b) The normalized CODEX signal of the selected crystalline peak versus τ_{mix}, aiming to probe the timescale of monomer jumps. The sample was crystallized and measured at $120\,^\circ C$. The solid line refers to the fit according to the reference [75]. The dashed line indicates where the normalized intensity is 0.5. The normalized CODEX signal of the other crystalline peaks is illustrated in Appendix Figure 6.4. The figures are adapted from the reference [76].

To probe slower ICD ($\langle \tau_c \rangle > 200\,\mu s$), we performed Chemical Shift Anisotropy

(CSA)-based [13]C Centerband-Only Detection of Exchange (CODEX) measurement, which allows the observation of ICD up to $1\,s$. As P3HB possesses a 2_1 helical structure in its crystals [134, 201], there is a variation of CSA tensor orientations from monomer to monomer. This means that a monomer jump along a polymer chain of P3HB in the crystalline region, as shown schematically in Figure 6.4 (a), can lead to a variation in CSA tensor orientation. Therefore, the detection of slow chain mobility in the crystalline regions by the CSA-based CODEX technique is possible [75]. As we are only interested in the change of CSA tensor orientation in the crystalline regions, prior to CODEX measurement, it is important to determine which of the ^{13}C resonances are associated with the crystalline regions, which is achieved by the ^{13}C NMR spectra measurement (Appendix Figure 6.3). The selected resonance peak from the crystalline regions is utilized to probe the slow mobility within the crystalline regions. The intensity of the crystalline peak versus mixing time (τ_{mix}, considered as waiting time) is shown in Figure 6.4 (b). To compensate for the signal losses caused by T_1-relaxation, instead of plotting the intensity of the corresponding peaks (S_{mix}) versus τ_{mix}, the normalized intensity (S_{mix}/S_0, S_0 is the intensity with a short τ_{mix}) is plotted versus τ_{mix}. In Figure 6.4 (b), the normalized signal (S_{mix}/S_0) of the crystalline peak decays with τ_{mix}, which means there are molecular rotations during τ_{mix}. If no reorientation of the CSA tensor occurs during τ_{mix}, the signal will be refocused completely (intensity remains constant over τ_{mix}). The exact $\langle \tau_{\mathrm{c}} \rangle$ is obtained by the fit according to the reference [75] (the solid line in Figure 6.4 (b)), which is around $0.12\,s$ at $120\,°C$. In Figure 6.4 (b), a dashed line illustrates the theoretical prediction of the normalized intensity at a large τ_{mix} [75]. The dashed line represents a plateau equal to $1/M$, M is the distinguishable monomer jumping sites. In our case, M is equal to 2, as schematically shown in Figure 6.4 (a). We notice that the theoretical prediction is consistent with our measurement results, which is also a proof that our CODEX measurement is convincing.

By measuring $\langle \tau_{\mathrm{c}} \rangle$ at different temperatures, the apparent activation energies E_{a} of P3HB crystallized at different temperatures were obtained (80-$90\,kJ\,mol^{-1}$) via Arrhenius plots (Appendix Figure 6.5). The CODEX-based activation energy can be compared with the one available from the DMA experiments on the compression-molded stripe of nonisothermally crystallized P3HB (Figure 6.2 (b)). Focusing on the region of the α_{c}-relaxation, it is possible to construct a master curve via time-temperature superposition (TTS, cf. Chapter 3), as illustrated in Appendix Figure 6.6. This proves that an actual relaxation process is indeed observed, with the temperature-dependent shift factors providing an activation energy of $82\,kJ\,mol^{-1}$, in good agreement with the NMR results.

6.4 Conclusion

In conclusion, we have found that the well-documented embrittlement of P3HB, i.e. a significant reduction of the strain at break and a slow increase of the shear modulus upon aging at room temperature, can also be achieved by higher-temperature annealing at 60 °C. Under these conditions, SAXS results indicate that the crystalline layer thickness slowly rises, the amorphous layer thickness slowly decreases and its distribution narrows. All methods show that during further aging at 60 °C, the sample keeps changing in the same way, but simply on a much longer timescale.

All these observations are in line with P3HB being a crystal-mobile polymer, where Intracrystalline Chain Diffusion (ICD) enables lamellar thickening during primary as well as secondary crystallization, as established by our recent publications [47, 48]. While we lack a model to explain the mechanistic connection between embrittlement and the observed morphology changes, it can be hypothesized that the glass transition temperature in the increasingly small amorphous domains, being generally close to room temperature, increases due to confinement effects, leading to brittle rather than elastic contributions to the overall mechanical response. Another possibility would be that during aging, densification of the material leads to the formation of small micro-cracks, making the material more sensitive to fracture.

In summary, in contrast to the recent claim of Xia et al. [142], we have identified P3HB as a crystal-mobile polymer. While the possible relation between the observed ICD, the lamellar thickening and the embrittlement remains an open question, we anticipate the development of more focused strategies to improve the mechanical properties of this fascinating material, e.g. by copolymerization with monomers that do not fit the crystals and thus limit lamellar thickening, in analogy to similar strategies that are well-established for, e.g., poly(ethylene).

6.5 Experimental details

This section is different from the Experimental Method Chapter (Chapter 3). The section here contains only the instrumental parameters and sample treatments for the purposes of data reproduction.

Tensile testing

Stress-strain measurements were performed with a Linkam tensile-stage TST350 (Tadworth, UK) equipped with a 200 N load cell. Due to the low nucleation rate at $120\,°C$ [138], a direct melt crystallization leads to millimeter-sized spherulites, which does not allow for further tensile testing. For this reason, P3HB films were prepared by cold crystallization, where a low-temperature crystal nucleation step at $25\,°C$ for $1\,min$ is included before isothermally crystallizing the sample at $120\,°C$ for $7\,min$. P3HB films with a thickness of about $200\,μm$ were punched into a dumbbell-shaped specimen with a gauge length of $5\,mm$ and gauge width of $2\,mm$. The experiment was performed at room temperature ($26\pm2\,°C$) at a constant cross-head speed of $5\,μm\,s^{-1}$ and with a pre-load of $0.2\,N$. All measurements were carried out within $5\,min$ after sample preparation or thermal treatment to avoid physical aging or annealing effects. The results for the ultimate properties were averaged over at least 5 samples.

Dynamic mechanical analysis

The shear modulus was measured with a rheometer Ares G2 equipped with a heating chamber from TA instruments using a sample in stripe geometry (sample length between clamps $20\,mm$, width $10\,mm$, thickness $1.5\,mm$) at a constant strain of 0.1%. Real-time aging experiments were conducted at $10\,rad\,s^{-1}$ at $60\,°C$ and frequency sweeps were conducted from 0.1 to $100\,rad\,s^{-1}$ in a temperature range between -10 and $150\,°C$.

Samples were prepared by both isothermal crystallization at $120\,°C$ for 1 hour (for aging experiments) and non-isothermal crystallization upon cooling with around $5\,K\,min^{-1}$ (for frequency sweeps) in a rectangular molds (MeltPrep device) and always installed in the rheometer at room temperature.

Small-angle X-ray scattering (SAXS)

SAXS measurements were performed on a Kratky compact camera (Anton Paar GmbH, Graz, Austria) equipped with an X-ray optics (AXO Dresden GmbH, Germany), a temperature-controlled sample holder, and a 1D detector Mythen2 R 1K (Dectris, Switzerland). As the camera has a slit focus, the data had to be deconvoluted. This was achieved by applying the desmearing algorithm by Strobl [190].

The P3HB samples were quenched from the melt state ($190\,°C$) to $120\,°C$ at estimated cooling rate of $5\,K\,min^{-1}$ for isothermal crystallization in the Kratky camera. The exposure time for each measurement was $10\,min$.

The analysis of the SAXS data is based on the interface distribution function (IDF or K"(z)), introduced originally by Ruland [191]. The detailed analysis procedure is described in our previous publications [47, 50]. The examples can also be found in Chapter 3.

Proton low-resolution NMR-FID

[1]H time-domain nuclear magnetic resonance (NMR) experiments at low field ($B_0 \approx$ 0.5 T) were performed on a Bruker minispec mq20 spectrometer with a proton frequency of about 20 MHz ($B_0 \approx 0.47$ T) using a static probe head. Temperature regulation via a regulated air flow is provided by a BVT3000 unit with an accuracy of about ± 1 K and a gradient of up to 0.5 K across the sample. The 90° and 180° pulse lengths ranged from 1.5 to 1.8 µs and 3.5 to 3.7 µs, respectively; the recycle delay (RD), i.e., the time between successive scans was set to 1.5 to 4 s, which is about 5 times longer than [1]H T_1 relaxation time. To overcome problems with the dead time of about 15 µs, we compared free induction decay (FID) signals detected directly after a 90° pulse with signals after a magic-sandwich echo (MSE). The latter avoids the dead time but features some loss of intensity, meaning that shape parameters are taken from the MSE-FIDs while component amplitudes are taken from the FIDs.

The samples were heated to 180 °C for 5 min as a compromise between the removal of thermal history and thermal degradation, and cooled to 120 °C for isothermal crystallization. The step-wise heating for the measurement, as shown in Appendix Figure 6.2, was carried out with a rate of about 5 K min^{-1}, with an additional 10 min of equilibrium time before each NMR-FID measurement.

For a detailed analysis of FID measurement, refer to our previous publications [67, 72, 73]. An example of the analysis of sample can also be found in Chapter 3.

^{13}C MAS NMR

All ^{13}C spectra and data were recorded on 400 MHz Bruker Avance III spectrometers with ^{13}C Larmor frequency of 100.6 MHz using double- and triple-resonance magic-angle-spinning (MAS) probes at a spinning frequency of 10,000 ±3 Hz. The pulse lengths on the ^{1}H and ^{13}C channels were around 3 µs. The transmitter power used for ^{1}H and ^{13}C was around 40 and 140 W, respectively, corresponding to pulse lengths of around 3 µs on both channels. Cross-polarization (CP) spectra rely on ^{1}H-^{13}C dipolar polarization transfer, which is less efficient for more mobile chains. We used short contact times of 0.01 ms to polarize exclusively the crystalline component. In contrast, ^{13}C direct polarization (DP) with a short RD of around 1 s measures the mobile/amorphous signals.

Slow molecular rotations: Rotor-synchronized ^{13}C centerband-only detection of exchange (CODEX) was performed using the triple-resonance probe at 10 kHz MAS; high-power proton decoupling (SPINAL64) [202] was used during the evolution and acquisition of the ^{13}C signal. The $\pi/2$ pulses for ^{1}H and ^{13}C were set to 3.0 and

3.4-3.6 µs, respectively. The required recoupled evolution time ($N\tau_r$) was set to 0.3 ms with a $\tau_r = 100$ µs and N being integer. The recycle delay and contact times were 4-8 s and 1.7 ms, respectively.

The detailed analysis of CODEX and ^{13}C spectra measurement refers to the references [73, 75, 76].
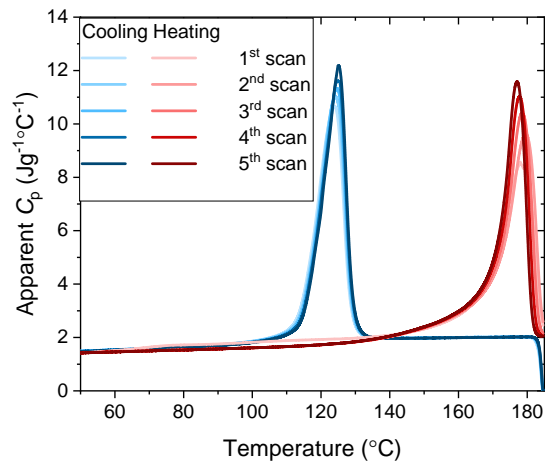
6.6 Appendix

Figure 6.1: Changes of the melting temperature (peak position) of P3HB over 5 repeated DSC cooling and heating scans at $10\,\mathrm{K\,min^{-1}}$ in the temperature range from -20 to 185 °C. The in-between isothermal steps at -20 and 185 °C lasted for 2 minutes. The figure is adapted from the reference [76].
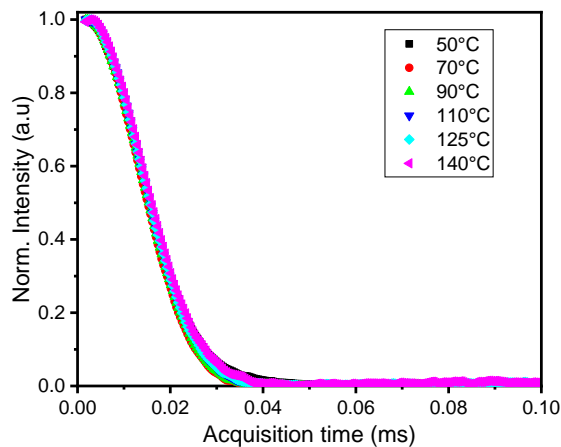
Figure 6.2: Normalized crystalline components of ^{1}H NMR-FID at different temperatures after subtraction of fitted amorphous components of P3HB, isothermally crystallized for 1 h at 140 °C. The figure is reproduced from the reference [76].
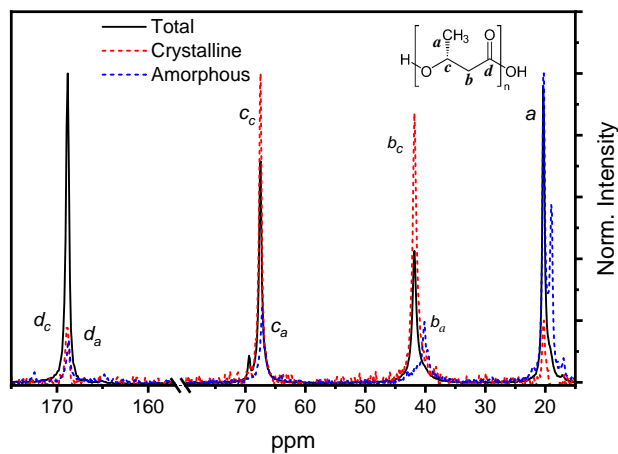
Figure 6.3: Comparison of selective ^{13}C MAS spectra of P3HB ($T_c = 140$ °C). The ^{13}C assignment is displayed in the inset; crystalline and amorphous resonances are assigned with subscripts c and a. The figure is adapted from the reference [76].
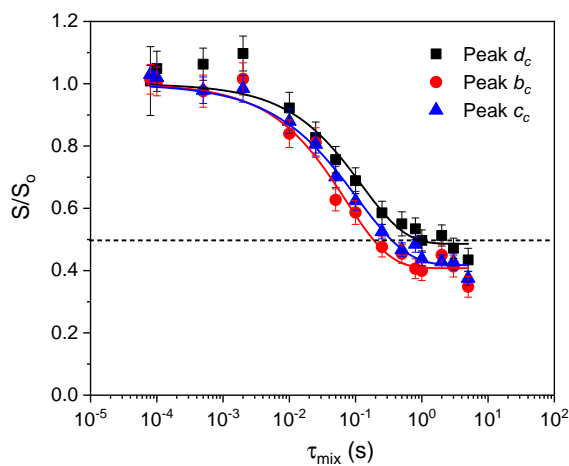
Figure 6.4: The normalized CODEX signal of all the crystalline peaks versus τ_{mix} to probe the timescale of monomer jumps. The sample was crystallized and measured at 120 °C. The solid line refers to the fit according to the reference [75]. The dashed line indicates where 0.5 is. Peaks b_{c}, c_{c} and d_{c} refer to the corresponding peaks in Appendix Figure 6.3. The figure is adapted from the reference [76].
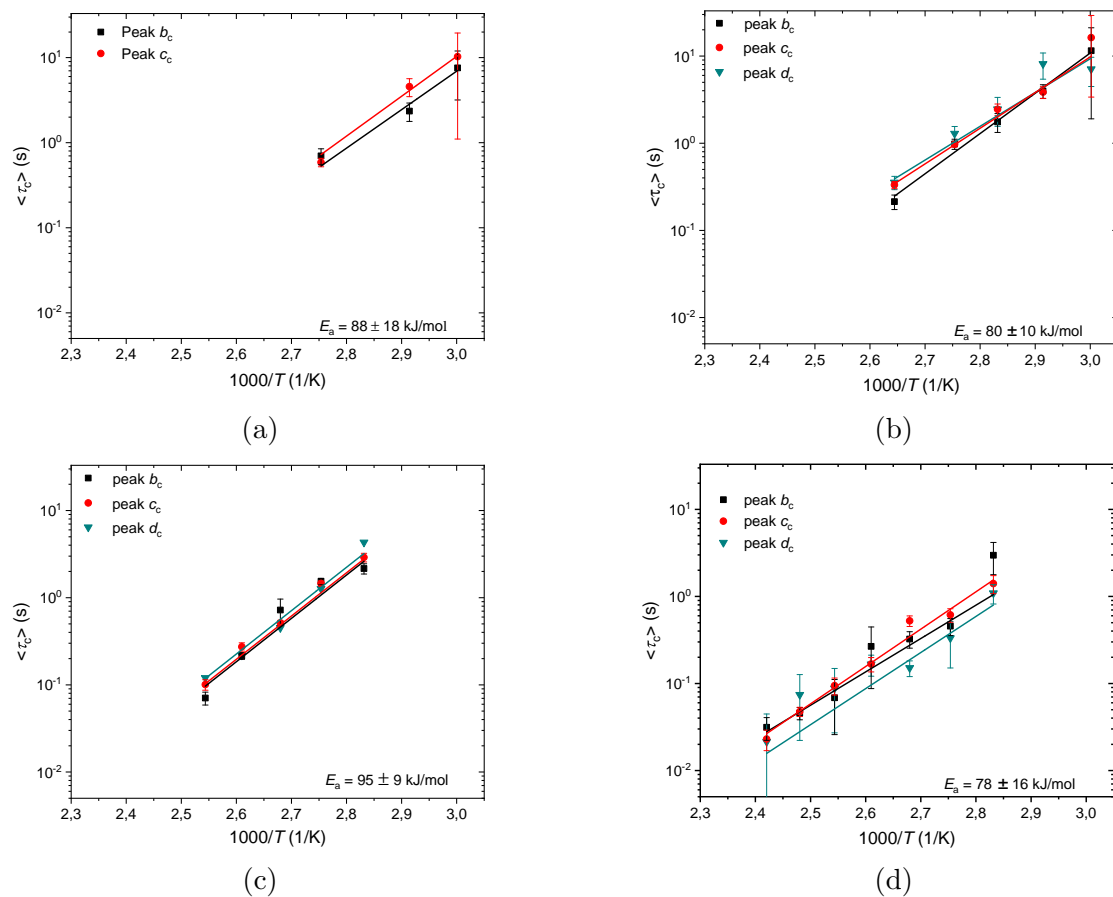
Figure 6.5: Arrhenius plots of $\langle \tau_c \rangle$ in P3HB isothermally crystallized at (a) 90 °C, (b) 105 °C, (c) 120 °C, and (d) 140 °C. We refer to E_a as "apparent" value, as we only cover a small temperature range which might overlook other complicated processes [73]. The figures are adapted from the reference [76].

(a)

(b)
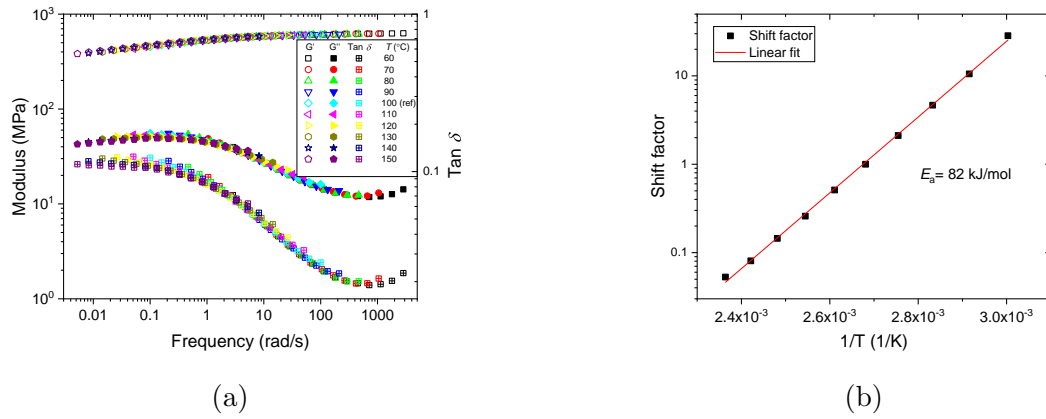
Figure 6.6: (a) Master curves ($T_{ref} = 100\,°C$) of the storage and loss moduli (G' and G'', resp.) and tanδ of a compression-molded plate of isothermally crystallized P3HB ($T_c = 120\,°C$) constructed from frequency sweeps between 0.1 and $100\,rad\,s^{-1}$ measured at different temperatures, where the maximum of the latter two corresponds to the α_c-relaxation. (b) Arrhenius plot of the temperature-dependent horizontal shift factors from mastering. The slope provides an apparent activation energy of around $82\,kJ\,mol^{-1}$, which is comparable with the activation energy of the α_c-relaxation probed by CODEX NMR experiments. The reliability of this approach is discussed in Appendix Figure 6.7. The figures are adapted from the reference [76].

(a)

(b)

(c)
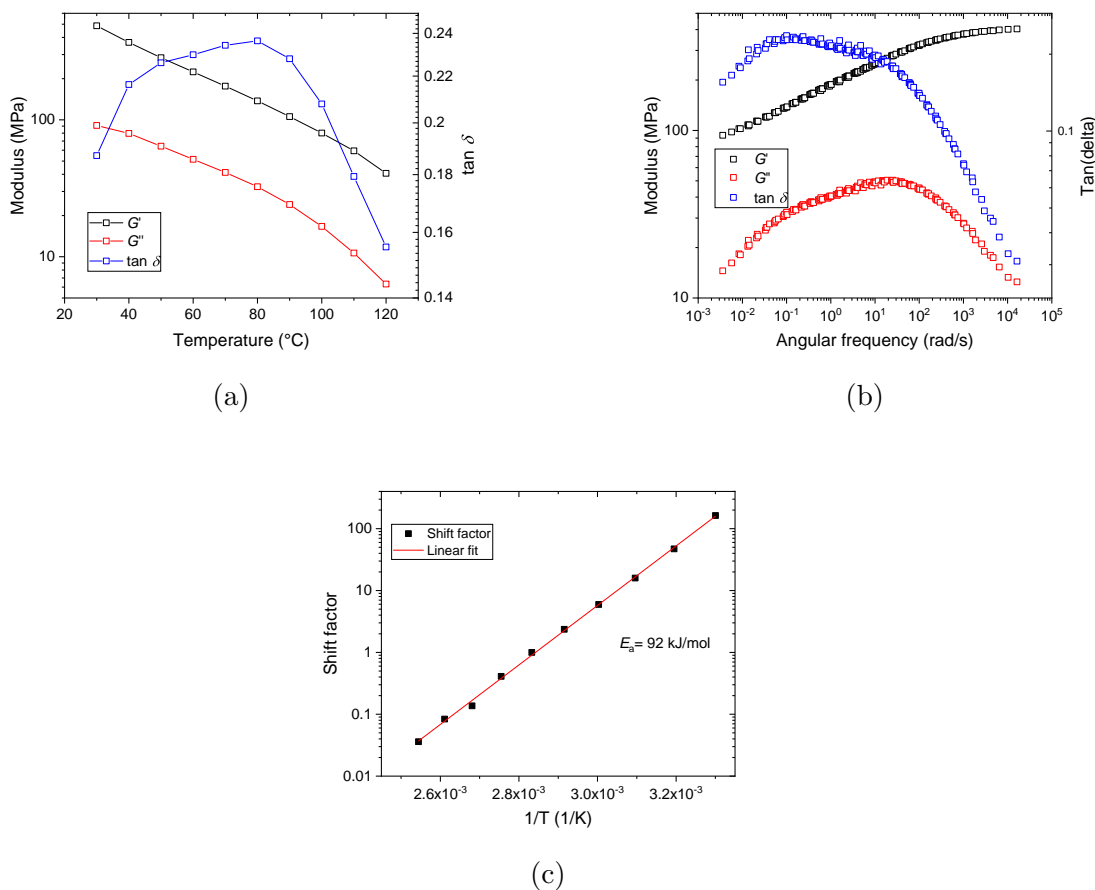
Figure 6.7: Rheology results of non-isothermally crystallized HDPE as a reference. (a) Temperature sweep with a frequency of $0.1\,\text{rad}\,\text{s}^{-1}$ at $0.1\,\%$ strain. (b) Master curves ($T_{\text{ref}} = 80\,°\text{C}$) covering the range of the α_{c}-relaxation. (c) Arrhenius plot of the shift factor provides an apparent activation energy of $92\,\text{kJ}\,\text{mol}^{-1}$, which corresponds well with literature values [52, 74, 203]. This demonstrates the reliability of this approach to determine the activation energy of the non-isothermally crystallized P3HB. The figures are adapted from the reference [76].

Chapter 7

Semicrystalline morphology, intracrystalline chain diffusion and mechanical modulus of a series of selected aliphatic polyesters

7.1 Introduction

A-B aliphatic polyesters are the most successful candidates to replace commodity plastics due to their similar mechanical and thermal properties to commodity plastics and their degradability, they are, however, not yet widely studied in terms of their semicrystalline morphology and α_c-relaxation (cf. Chapter 4). The α_c-relaxation is commonly attributed to helical jumps of the chains within the crystals [52], or Intracrystalline Chain Diffusion (ICD). The characteristic timescale of ICD is $\langle \tau_c \rangle$. There are even fewer investigations on different aliphatic polyesters with the purpose of understanding the role of functional groups for ICD and semicrystalline morphology (cf. Chapter 1). The functional groups can be the CH_3 group as a side chain, the CH_2 group in monomer, etc.

From the experimental observation by Boyd, in terms of different crystallinity (X_c), semicrystalline polymers are divided into three classes: high-crystallinity polymer ($X_c > 60\%$), medium-crystallinity polymer ($60 \geq X_c > 30\%$) and low crystallinity polymer. High-crystallinity polymer possesses α_c-relaxation, while medium- and low-crystallinity polymers show no sign of α_c-relaxation [204]. The observation is limited by the types of semicrystalline polymers, e.g. PE, PP and a few commercially available plastics. In addition, from our previous studies [47, 48] and Chapters 5 and 6, we find that the semicrystalline polymer with measurable ICD always possesses the specific morphological features: the average crystalline layer thickness (d_c) is greater than the average amorphous layer (d_a), the distribution width of crystalline layer thickness (σ_c), is greater than the distribution width of amorphous layer thickness,

σ_a. As pointed out by the previous chapters, a measurable ICD refers to its characteristic timescale ($\langle \tau_c \rangle$) up to 1 s. We also called the polymers with measurable ICD crystal-mobile polymers. The semicrystalline polymer with no measurable ICD ($\langle \tau_c \rangle$ > 1 s) shows different morphological features: $d_c \leq d_a$, $\sigma_c \leq \sigma_a$. These polymers are called crystal-fixed polymers. To check whether the experimental observation from Boyd and the findings from our studies are, in general, valid, we expand our investigations further into a series of selected A-B aliphatic polyesters with similar chemical structures.

In the following study, to test the generality of the experimental observation from Boyd and the findings from our previous studies, the semicrystalline morphology and α_c-relaxation (ICD) of the series of A-B aliphatic polyesters with similar chemical structures were investigated by the combination of SAXS and NMR techniques. Through the comparison among the polyesters, we develop the hypotheses to understand the influence of chemical structures of monomers on ICD, semicrystalline morphology and thermal properties of the polyesters. Additionally, we investigated the crystallinity-dependent mechanical modulus of different polyesters by the combination of NMR and mechanical measurements. A relationship between the crystallinity and shear modulus of all different polyesters is summarized.

At the end of this chapter, it is an appendix (Section 7.7) containing all the necessary raw data to support the main text.

7.2 Materials

We selected this series of A-B aliphatic polyesters based on the material availability. Poly Glycolic Acid (PGA) was purchased from Polysciences Europe GmbH (Germany). The molecular weight (M_w) is above $100 \, \text{kg mol}^{-1}$. Poly-L-Lactide Acid (PLLA) was provided by Corbion (Amsterdam, Netherlands) in the form of pellets (Grade: L175), with M_w of $120 \, \text{kg mol}^{-1}$. Poly-3-hydroxybutyrate (P3HB) was supplied by Mr. Haenggi from Biomer (Germany), in the form of pellets (P338) from T26 powder. Poly-4-hydroxybutyrate (P4HB) was synthesized by Prof. Manfred Zinn from HES-SO Valais-Wallis university (Switzerland). Polyvalerolactone (PVL) was synthesized by Dr. Svenja Stuermer from university Hamburg, with M_w=$190 \, \text{kg mol}^{-1}$, PDI=2. Poly ω-pentadecalactone (PPDL) was provided by Dr. Felix Scheliga from university Hamburg, M_w=$439 \, \text{kg mol}^{-1}$, PDI=4.92. To facilitate reading, we summarize molecular weight of each polyesters and thermal properties either measured in our lab or data from the literature in Table 7.1.

In addition, the high density polyethylene (HDPE) and polybutylene succinate (PBS) used in this chapter as benchmark materials were provided by Total (Grade: Lumicene® mPE M5510EP) with $M_n = 27\,700 \, \text{g mol}^{-1}$, PDI = 2.8 and by PTT MCC Biochem Co., Ltd. (Grade: FZ91) with $M_n = 40\,850 \, \text{g mol}^{-1}$, $M_w = 143\,400 \, \text{g mol}^{-1}$.

Table 7.1: The molecular weight (M_n and M_w), polydispersity (PDI), glass transition temperature (T_g), melting temperature (T_m) and enthalpy of melting of different polyesters ($\Delta H_{m,100}$). T_m was determined based on the maximum of melting peak position according to the second heating scan of each polyester at $10\,\mathrm{k\,min^{-1}}$ by DSC. The raw DSC data are illustrated in Appendix Figure 7.1. $\Delta H_{m,100}$ was calculated by NMR crystallinity in Appendix Figure 7.15 and melting enthalpy measured by DSC in Appendix Figure 7.2. '*' literature values, '-' data is not available, 'a' data is provided by the suppliers.

Polyesters	M_n kg mol⁻¹	M_w kg mol⁻¹	PDI	T_g^* °C	T_m °C	$\Delta H_{m,100}^*$ J g⁻¹	$\Delta H_{m,100}$ J g⁻¹
PGA	-	100ᵃ	-	40 [83]	223	139 [97], 180, 202 [95], 183 [84]	129.3
PLLA	-	120ᵃ	-	50-60 [83]	175	104.5 [117]	-
P3HB	-	-	-	0-40 [127–129, 205]	174	146 [138]	-
P4HB	310	848	2.73	-51 [206]	52	-	96.9 ±7.2
PVL	95	190	2	-66 [162]	58	182 [154]	143.3 ±4.7
PPDL	89	439	4.92	-23, 33 [161]	95	227 [160], 233, 264 [161]	211.7

7.3 Results

7.3.1 The crystallinity of different polyesters

To check the generality of the experimental observation from Boyd, firstly, we need to characterize the crystallinity (X_c) of the aliphatic polyesters listed in Table 7.1. To reliably measure the crystallinity, we performed SAXS measurement on all the polyesters at their corresponding isothermal crystallization temperatures. After the determination of the average crystalline layer thickness (d_c) and amorphous layer thickness (d_a) of the polyesters by using the 1D stack model to analyze SAXS data (cf. Chapter 3), the crystallinity of the polyesters was calculated according to Equation 7.1. The sum of d_a and d_c is long period, LP. The results are shown in Figure 7.1. PLLA and P3HB both possess a crystallinity above 60%. The crystallinity of PGA, P4HB, PVL and PPDL scatters between 30 and 60%. No clear dependence of X_c

on N_{cc} is seen. The definition of N_{cc} can be found in the caption of Figure 7.1. According to the definition of polymer category by Boyd, we find that the polyesters in Table 7.1 fall into two classes of polymers: high-crystallinity polymers (PLLA and P3HB) and medium-crystallinity polymers (PGA, P4HB, PVL and PPDL).
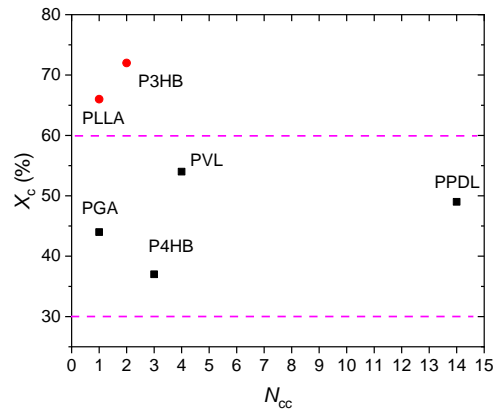
$$X_c = d_c/(d_c + d_a) \cdot 100\% \tag{7.1}$$

Figure 7.1: SAXS crystallinity (X_c) of different polyesters measured at the corresponding isothermal crystallization temperatures by SAXS. N_{cc} is the number of carbon-carbon bonds along the backbone of polyester in each repeating monomer unit, e.g. P4HB has 3 carbon-carbon bonds along the backbone in each monomer; PLLA has 1 carbon-carbon bond along backbone, which is the same as PGA. Two magenta dashed lines are only to illustrate clearly where 30 and 60% are.

7.3.2 The semicrystalline morphology of different aliphatic polyesters

To check the generality of the findings from our previous studies [47, 48] about the characteristic of semicrystalline morphology of polymers, d_a, d_c, their distribution width σ_a, σ_c and LP of all the polyesters are studied.

Medium-crystallinity polyesters (PGA, P4HB, PVL and PPDL): LP d_c, d_a and their corresponding distribution width σ_c and σ_a of medium-crystallinity polyesters are illustrated in Figure 7.2 (a)-(d). To facilitate the comparison, only the corresponding results obtained at the end of the isothermal crystallization process of PGA, P4HB, PVL and PPDL at different temperatures are shown in Figure 7.2 (a)-(d). The semicrystalline morphology of different polyesters during the course of the isothermal crystallization process at different temperatures can be found in Appendix Figures 7.3, 7.4 and 7.5. In addition, Appendix Figures 7.3 and 7.4 contain the information of the crystal thickening rate of these four polyesters during crystallization, which will be compared separately in detail in the discussion section. As shown in Figure 7.2 (a)-(d), d_c of all four polyesters increases with isothermal crystallization temperatures (T_c) individually, and so does d_a of all polyesters, with the exception of PGA, of which d_a fluctuates with T_c. PGA, P4HB and PPDL show greater d_a value than d_c value, while d_a of PVL is slightly smaller than d_c of PVL. The distribution width of amorphous layer thickness (σ_a) of 4 polyesters is, not exceptionally, broader than that of crystalline layer thickness (σ_c). Please note that PGA possesses polymorphism, this study focuses only on its α form crystal [88, 89]. Polymorphism of the other three polyesters has not been reported (cf. Chapter 4).

High-crystallinity polyesters (PLLA and P3HB): LP, d_c, d_a and their corresponding distribution width σ_c and σ_a of high-crystallinity polyesters at the end of the crystallization process are shown in Figure 7.2 (e)-(f). The change of LP, d_c, d_a and their corresponding distribution width σ_c and σ_a during crystallization at different temperatures can be found in Appendix Figures 7.6 and 7.7. d_c value of both polyesters increases with crystallization temperatures, while d_a value of both polyesters does not vary significantly with crystallization temperatures. LP of both polyesters, which is the sum of d_a and d_c, consequently increases with crystallization temperatures. At all crystallization temperatures, both polyesters show a greater d_c value than d_a value, and a broader distribution width of crystalline layer thickness (σ_c) than that of amorphous layer thickness (σ_a). We are aware of the presence of polymorphism of both polyesters [111, 134, 135, 208], and present in this study only the semicrystalline morphology of α form crystal of both polyesters.

Additionally, we notice that different polyesters have different d_c values, as summarized in Figure 7.3. PGA has the smallest d_c value, while PLLA has the greatest d_c value. d_c value of polyesters possessing similar crystal unit cell (P4HB, PVl, PCL, PPDL, HDPE cf. Chapter 4) increases with increasing of N_{cc}. This trend of d_c is discussed in detail in the discussion section below.
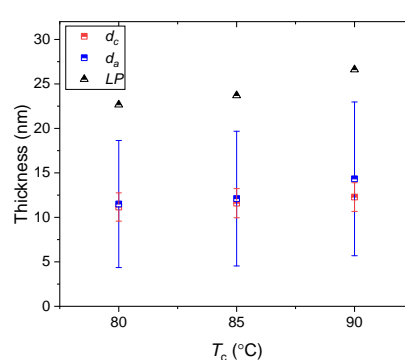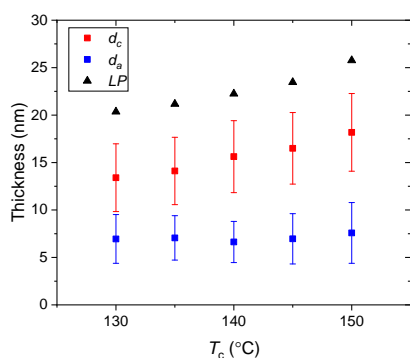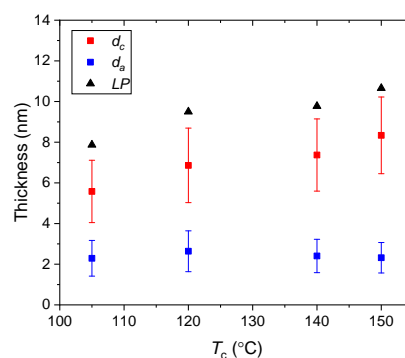
(a) PGA

(b) P4HB

(c) PVL

(d) PPDL
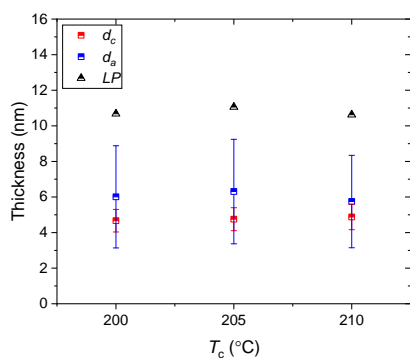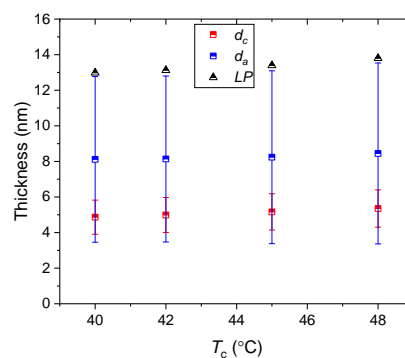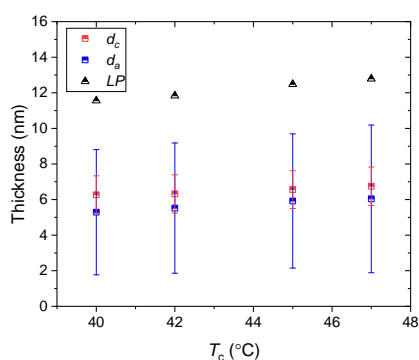
(e) PLLA

(f) P3HB

Figure 7.2: d_c, d_a and LP of four medium-crystallinity polyesters measured at the corresponding isothermal crystallization temperatures ((a) PGA, (b) P4HB, (c) PVL and (d) PPDL), based on the last points in Appendix Figures 7.3 and 7.4. d_c, d_a and LP of PLLA (e) and P3HB (f) at different isothermal crystallization temperatures, based on the last points in Appendix Figures 7.6. The error bars are the distribution width of d_a (in blue) and d_c (in red). The detailed SAXS analysis is illustrated in Appendix Figures 7.8, 7.9, 7.10, 7.11, 7.12 and 7.13. The assignment of d_c and d_a was based on ^{1}H NMR-FID measurement in Appendix Figure 7.15 or the trend of change of d_c and d_a during crystallization (Appendix Figure 7.5 (a)). P3HB and PLLA are known to have more than 50 % crystallinity, according to our study in Chapter 6 and the reference [207].
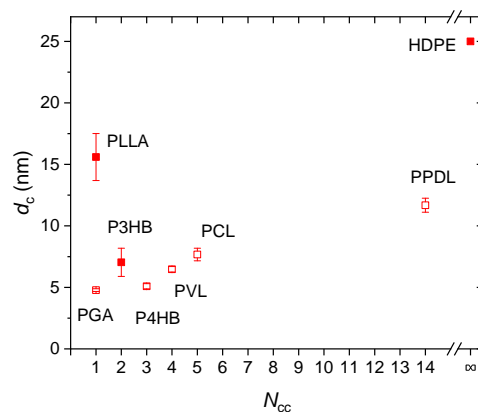
Figure 7.3: The summary of d_c of different polyesters from Figure 7.2. d_c is the average value of each polyester at all measured isothermal crystallization temperatures, its standard deviation is illustrated by the corresponding error bar. PCL data is reproduced and modified from the reference [47]. HDPE data is added into the plot as a reference, which is obtained from our SAXS measurement on Total Lumicene® M5510 at $123\,°C$ ($T_c = 123\,°C$, for $150\,min$). The open dots are polymers either with no measurable ICD or no information of ICD available from the literature. The solids dots are the polymers with known ICDs.

7.3.3   ICD of different aliphatic polyesters

To further confirm the generality of the experimental observation from Boyd and the findings from our previous studies, the direct measurement of the timescale of ICD ($\langle \tau_c \rangle$) by NMR on these polyesters is necessary. The NMR experiments described in this chapter were conducted by Afiq Anuar from the solid-state NMR group headed by Prof. Kay Saalwächter. We provide here a sufficient description of the NMR results to support our argument.

The temperature-dependent ^{1}H NMR-Free Induction Decay (FID) measurements were performed to examine the presence of fast ICD ($\langle \tau_c \rangle < 200\,\mu s$) in the crystalline fraction of the polyesters listed in Table 7.1. Besides fast ICD, the ^{1}H NMR-FID measurements also enable us to determine the crystallinity (X_c), which we discuss separately further in the discussion section below. PLLA and P3HB were excluded from ^{1}H NMR-FID measurements because it is known that these two polyesters have measurable ICDs from Chapter 6 and the reference [122]. If $\langle \tau_c \rangle < 200\,\mu s$, the shape of the crystalline components of FID curves would change with temperatures [72]. However, the crystalline components of the FID curves of each polyester, measured at different temperatures, are overlapping (Appendix Figure 7.19). This independence of the shape of the curves on temperature indicates the absence of ICD on the timescale up to $200\,\mu s$ at all measured temperatures.
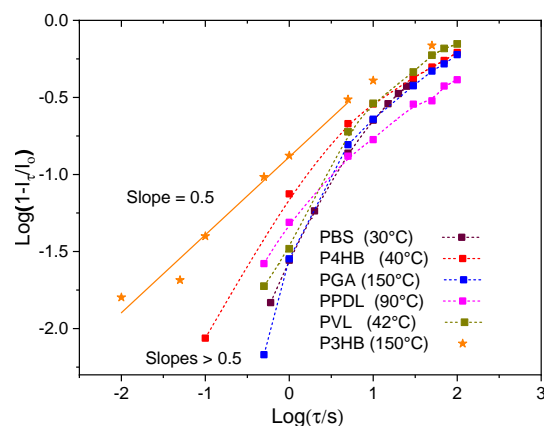

Figure 7.4: [13]C T_1-relaxation measurement plot of $\log(1 - I_\tau/I_0)$ of the selected crystalline peaks (Appendix Figure 7.16) of isothermally crystallized PGA, P4HB, PVL and PPDL measured by ^{13}C NMR spectra measurement versus waiting time in logarithmic scale ($\log(\tau)$). The temperatures in the brackets in the legend are the measurement temperatures. The crystallization conditions refer to Experimental details section 7.6. The data from PBS and P3HB are illustrated here as examples of typical crystal-fixed and crystal-mobile polymers, respectively. The solid line is a linear fit with a slope of 0.5. The dashed lines are guides to the eye.

As no fast ICD is present in PGA, P4HB, PVL and PPDL, we performed ^{13}C T_1-relaxation to prolong the possible experiment time to observe slow ICD, $\langle \tau_c \rangle$ up to 1 s. This measurement probes the presence of diffusive long-range ICDs in samples, which is based on the detection of monomer exchange between crystalline and amorphous regions. Therefore, prior to ^{13}C T_1-relaxation measurements, it is necessary to distinguish between ^{13}C NMR signals in crystalline and amorphous regions, which was achieved by ^{13}C NMR spectra measurement (Appendix Figure 7.16). Figure 7.4 shows the results of ^{13}C T_1-relaxation measurement of the selected crystalline peaks of PGA, P4HB, PVL and PPDL according to the ^{13}C NMR spectra measurement (Appendix Figure 7.16). A special way of representing the results of ^{13}C T_1-relaxation measurement is adopted in Figure 7.4, below is a brief explanation. In a rigid semicrystalline system, the ^{13}C T_1-relaxation of polymer chains in the crystalline regions exhibits a slow exponential decay ($\tau > 10$ s), which means that the intensity of the magnetization (I_τ) of the selected crystalline peak (Appendix Figure 7.16) decays exponentially with waiting time, τ. If there is the presence of the diffusive crystalline chains, I_τ of the selected crystalline peak decays linearly with $\sqrt{\tau}$ when τ is short, e.g. around less than 1 s [74], according to Equation 7.2

$$\frac{I_\tau}{I_o} = 1 - \frac{\sqrt{2D}}{d_c}\sqrt{\tau} \tag{7.2}$$

where D is the diffusion coefficient and d_c is the crystalline layer thickness, I_τ is the intensity of magnetization of the selected crystalline peak measured at waiting time (τ), which is normalized by its initial value I_o. In order to more clearly observe the presence of a diffusive chain mode, Equation 7.2 is rearranged as

$$\log(1 - \frac{I_\tau}{I_o}) = \frac{1}{2}\log(\tau) + \log\frac{\sqrt{2D}}{d_c} \tag{7.3}$$

Then, if there are diffusive crystalline chains, $\log(1 - \frac{I_\tau}{I_o})$ of the selected crystalline peaks has a linear dependence on $\log(\tau)$ with a slope of 0.5. We consider Equation 7.3 to be an improved version of the analysis used in Chapter 5 for PBS. Therefore, instead of showing the relaxation of the intensity of magnetization versus measurement time, we plotted $\log(1 - \frac{I_\tau}{I_o})$ versus $\log(\tau)$ in Figure 7.4. A 0.5 slope is seen from isothermally crystallized P3HB (star symbol), which is the reference polymer that has the measurable ICD based on the results from Chapter 6. In contrast, no 0.5 slope is observed from the other polyesters (P4HB, PGA, PPDL, and PVL) in Figure 7.4, which means the absence of ICD up to 1 s. PBS is added to the plot as the reference polymer with no measurable ICD [67]. The presence of even slower ICD in the crystalline region is more difficult to be probed by NMR measurements, although they might exist. A quantitative comparison of ICD might be possible by SAXS measurement (crystal thickening rate), which is discussed separately in the following section.

In addition, we notice different chemical structures have different influences on ICD, which is also discussed in detail in the following section.

7.3.4   Mechanical modulus of different aliphatic polyesters at room temperature

Mechanical properties are crucial to determine whether these polyesters have potential for applications or not. Our focus is on the mechanical modulus, which can only be understood in depth with detailed characterization of semicrystalline morphology and ICD [33, 61]. Figure 7.5 shows the storage shear modulus (G') of all the polyesters from Table 7.1 at 30 °C, as 30 °C is the most relevant application temperature. G' of each polyester at other temperatures refers to Appendix Figure 7.17. In Figure 7.5, G' of all polyesters scatters between PGA and P4HB, showing no clear trend among different polyesters. G' of HDPE is added to Figure 7.5 as a benchmark. It is difficult to explain G' at 30 °C alone because all polyesters have different T_g and T_m, as shown in Table 7.1, which also play important roles for G'. To further understand the influence of semicrystalline morphology and ICD on mechanical modulus, we compare G' of different polyesters at temperatures above T_g. The details are presented in the discussion section below.
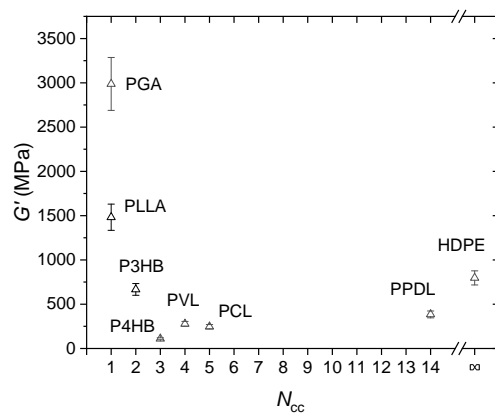
Figure 7.5: The shear modulus of different polymers at room temperature. The samples were isothermally crystallized in different temperatures and measured at a frequency of $10\,\mathrm{rad\,s^{-1}}$, a strain of 0.1% and at 30 °C. The detailed crystallization conditions are stated in the caption of Appendix Figure 7.17. We used 10% as the error bar of the measurement results. PCL data was reproduced from the reference [32].

7.4 Discussion

7.4.1 Is the experimental observation from Boyd and the findings from our previous studies also valid for A-B polyesters?

This work was motivated by the experimental observation from Boyd: high-crystallinity polymers possess α_c relaxation, while medium- and low-crystallinity polymers show no sign of α_c relaxation [204], and by our previous studies: the semicrystalline polymers with measurable ICD show the specific morphological features ($\sigma_a < \sigma_c$) and belongs to high-crystallinity polymers, but the semicrystalline polymers with no measurable ICD demonstrate different morphological features ($\sigma_c < \sigma_a$) and belong to medium-crystallinity polymers [47, 48]. In this section, we discuss the generality of the experimental observation and the findings from our previous studies based on the results obtained above. Before that, we compare our results with the available literature values, in order to rationalize their reliability.

Figure 7.2 (a)-(d) shows the semicrystalline morphology (d_a, d_c, σ_a, σ_c) of medium-crystallinity polyesters. Our d_c and d_a values of PGA and PPDL are comparable with literature values. These literature values were obtained either based on the analysis of a 1D correlation function of SAXS [91,98,157], or the combination of LP obtained by SAXS and the crystallinity by DSC [93]. d_c and d_a values of P4HB are not yet correctly revealed. Keridou et al. reported that LP of P4HB was around 10 nm and d_c was around 8 nm by using the analysis of the 1D correlation function of SAXS data [150, 151]. We further clarify the reason why our results are more reliable than those from Keridou and co-workers for such a low T_g and low T_m material in the following section. To our best knowledge, the semicrystalline morphology of PVL is not available from the literature (cf. Chapter 4). The distribution width σ_a and σ_c of all four polyesters are also not reported yet (cf. Chapter 4). Our NMR results show no sign of measurable ICD from PGA, P4HB, PVL and PPDL.

No ICD studies on these four polyesters have been reported yet (cf. Chapter 4).

Figure 7.2 (e)-(f) illustrates the semicrystalline morphology of high-crystallinity aliphatic polyesters. These d_c and d_a values of PLLA and P3HB are comparable to the literature values. Cho et al. reported d_c and d_a of α form crystal of PLLA based on the analysis of the interface distribution function of SAXS data [121]. They stated no observation of crystal thickening. Heo et al. used the 1D correlation function approach to analyze SAXS data and determined d_c and d_a of α form crystal of P3HB [139]. No observation of crystal thickening was claimed within around 1 h of measurement time at isothermal crystallization temperatures. The distribution widths, σ_a and σ_c of PLLA and P3HB have not yet been reported (cf. Chapter 4).

It is known that PLLA and P3HB have measurable ICD from the study in Chapter 6 and the reference [122].

All of our results are comparable with the available literature values. In addition,

our study provides complete information about the semicrystalline morphology and ICD of all of the aliphatic polyesters described in Chapter 4.

These results confirm that the generality of the experimental observation from Boyd can be well extended into all of our aliphatic polyesters, as all medium-crystallinity polymers (PGA, P4HB, PVL and PPDL) do not have measurable ICD, while PLLA and P3HB (high-crystallinity polymers) do have measurable ICD. The results also enable us to expand our findings from our previous studies into aliphatic polyesters. The aliphatic polyesters with measurable ICD (PLLA and P3HB) show the typical morphological features: $\sigma_c > \sigma_a$, and belong to high-crystallinity polymers, while the aliphatic polyesters without the measurable ICD (PGA, P4HB, PVL and PPDL) demonstrate different morphological features: $\sigma_a > \sigma_c$, and belong to medium-crystallinity polymers.

7.4.2   How is ICD of aliphatic polyesters affected by the CH$_3$ group?

We find a pair of aliphatic polyesters with and without CH$_3$ as a side chain (PLLA and PGA) in our work, they possess measurable and no measurable ICD [122], respectively. It is not uncommon in our work to notice this type of pair. Another similar pair is P3HB and P4HB. P3HB has the CH$_3$ group as a side chain and shows the measurable ICD (cf. Chapter 6). P4HB does not have the CH$_3$ group as a side chain, neither does P4HB have ICD. ICD measurement on PGA and P4HB is not yet studied in the literature, this type of comparison, which directly compares a polyester with its counterpart having the CH$_3$ group as a side chain, is therefore not yet reported.

Based on these two pairs from our work, we hypothesize that the CH$_3$ group as a side chain can facilitate the ICD of aliphatic polyesters. Song and co-workers reported that helical chain conformation is important for gaining ICD according to the comparison between PLLA and PCL [55]. However, it is difficult to separate the influence of CH$_3$ and helical chain conformation on ICD. For instance, both PLLA and P3HB, in our comparison, adopt helical chain conformation in the crystals [111, 134]. The presence of the CH$_3$ group as a side chain possibly favors helical chain conformation in polymer crystals [209]. It is also true for Isotactic Polypropylene (i-PP). I-PP shows helical chain conformation [210], while PE, its no CH$_3$ side group counterpart, adopts planar chain conformation [159]. However, it is well known PE does possess measurable ICD [74], which is somewhat contradictory to the importance of helical chain conformation for ICD. Therefore, we tend to stress the importance of the CH$_3$ group as a side chain for promoting ICD of polyesters. The reason that planar PE shows measurable ICD while planar aliphatic polyesters do not is discussed in the next section. Certainly, we admit a few deficiencies in our hypothesis and experiments. Firstly, our hypothesis is only based on a rather limited amount of pairs due to the material availability. More samples with the CH$_3$ group as a side chain should be investigated in the future to verify the hypothesis. Secondly, a direct

comparison between P3HB and Polypropiolactone (PPL) instead of P4HB will be more convincing. We are still working on the detailed characterization of PPL due to its complexity of polymorphism.

7.4.3 How is thermal properties, ICD and semicrystalline morphology of polyesters affected by the number of CH$_2$ groups in the monomer?

From the above-mentioned results, we find that the ester group and its concentration have important effects on many properties of the polyester samples, i.e. melting temperature (T_m) and enthalpy of melting ($\Delta H_{m,100}$), ICD and semicrystalline morphology. In this discussion section, we start with a short summary of the observations from the above-mentioned results and the comparison of the results with the available literature values; then we provide our hypothesis of the influence of the ester group and its concentration on the corresponding properties of the polyesters.

As listed in Table 7.1 and visualized in Figure 7.6 (a), T_m increases with N_{cc} (the definition of N_{cc} refers to the caption of Figure 7.1, $1/N_{cc}$ is proportional to the concentration of ester group in an aliphatic polyester), from P4HB to HDPE, while T_m of PGA, PLLA and P3HB is significantly higher than that of the other polyesters and does not follow any trend, which is often reported in the literature without explanations [155, 211]. $\Delta H_{m,100}$ of P4HB, PVL, PPDL and HDPE decreases linearly with $1/N_{cc}$ (the concentration of ester groups), as shown in Figure 7.6 (b). This dependence was suggested by Pepels and co-workers based on rather few available literature values [212]. $\Delta H_{m,100}$ of PGA, PLLA and P3HB is much higher than the dashed line, which has not yet been compared and reported in the literature. According to our NMR measurements, no measurable ICD in PPDL, PVL, P4HB or PGA up to the timescale of 1 s (Figure 7.4) is found, which is not reported elsewhere, although if there is a presence of ICD in which polymer is a long-standing scientific question [52]. Some molecular criteria regarding ICD have been proposed by Gedde [51], noting that aliphatic polyesters did not possess ICD due to the large size of the monomer. As observed from SAXS measurement, d_c of P4HB, PVL, PPDL and HDPE increases with N_{cc} (Figure 7.3). A similar observation is reported for the aliphatic polyesters with large N_{cc} without explanations [212]. We also observe that d_c of HDPE, PPDL, PVL and P4HB demonstrates different linear dependence on time in logarithmic scale during isothermal crystallization (Appendix Figure 7.3 and 7.4), as summarized in Figure 7.7. The crystal thickening rate of each polymer (the slope in Figure 7.7) follows such an order: HDPE≫PPDL>PCL>PVL≈P4HB. The linear dependence is mainly reported and discussed by researchers dealing with HDPE [66, 213, 214]. The characterization of d_c of polyesters is not widely carried out (cf. Chapter 4), not to mention the revelation of the dependence of d_c on time and the corresponding comparison among different polyesters [48] (cf. Chapter 4).

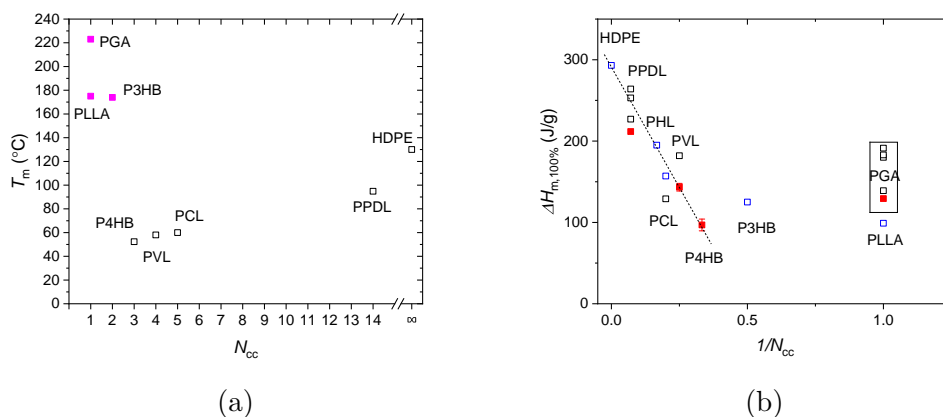Based on all these observations, we suggest discussing separately about non-PE-

Figure 7.6: (a) Melting temperatures of different polyesters and HDPE. Pink dots are not PE-like polyesters. Black dots are PE-like polyesters and HDPE. (b) $\Delta H_{\mathrm{m,100}}$ of different polyesters. The red dots are results measured by our group based on DSC melting enthalpy/crystallinity (NMR). The hollow dots are the literature values. As $\Delta H_{\mathrm{m,100}}$ involves mostly the crystallinity measurement, which is difficult to be precisely determined, we used blue color to indicate relatively reliable values from the literature. The dashed line is to guide the eyes. $\Delta H_{\mathrm{m,100}}$ of PHL (poly (7-heptalactone)) was reproduced from the reference [215]. The black box separates the literature values of $\Delta H_{\mathrm{m,100}}$ of PGA from that of PLLA.

like polyesters (PGA, PLLA, P3HB) and PE-like polyesters (P4HB, PVL, PPDL) on which our main focus is. This is because PGA, PLLA and P3HB possess crystal lattice constants different from HDPE and PE-like polyesters [89, 111, 134, 149, 158, 159, 216]. Additionally, the extra hydrogen bonding between chains exists in PGA and P3HB [91, 92, 136], which leads to a rather high melting temperature compared with other PE-like polyesters. Lastly, PGA, PLLA and P3HB do not follow linear dependence of $\Delta H_{\mathrm{m,100}}$ on $1/N_{\mathrm{cc}}$ like other PE-like polyesters and PE. This dependence is due to the energy penalty by the inclusion of ester groups in PE crystal [53, 212, 217]. Therefore, it is reasonable to discuss these two groups separately. Due to the lack of systematic trend from our experiments on non PE-like polyesters, there is no further discussion on these three polyesters in this section, other than merely on PE-like polyesters and PE.

For PE-like polyesters, we hypothesize that their ICD has the dependence on N_{cc} (interpreted also as inverse content of ester group in monomer), i.e. ICD is faster when N_{cc} increases, ICD slows down when N_{cc} decreases. Below is the explanation. It is well recognized that the slope of crystal thickening is the product of reciprocal of the energy barrier per unit length and kT according to Equation 7.4 [66], where t is time, k is Boltzmann constant, l is crystalline layer thickness at t, t_0 is the time when a crystal with certain thickness is initially born, A is a fitting parameter and the slope of crystal thickening is equal to $(kT)/C$, and C is the energy barrier per

unit length of d_c.

$$l = \frac{kT}{C} log \frac{2.3A}{\frac{kT}{C}} + \frac{kT}{C} log(t - t_0) \qquad (7.4)$$

Equation 7.4 is one of the solutions to Equation 7.5 [66], which phenomenologically describes the dependence of d_c on time.

$$\frac{dl}{dt} = Ae^{-\frac{Cl}{kT}} \qquad (7.5)$$

$\frac{kT}{C}$, the crystal thickening slope, is therefore able to qualitatively distinguish difference among different levels of ICD. Schulz et al. showed that polymers with different ICD levels demonstrate different crystal thickening slopes [48]. The reason that ICD slows down from HDPE to PPDL is the formation of the layered structure of ester groups in crystals of polyesters [51, 53]. Once this layered structure is disturbed, a measurable ICD reappears [54]. The slope becomes smaller and smaller from PPDL to PVL because the number of layered structures per unit length of d_c in crystal increases. ICD slows down further when N_{cc} decreases until it is too slow to be distinguished between PVL and P4HB. Our hypothesis also rationalizes the experimental observations that both d_c and T_m increase with N_{cc}, which was observed by Pepels and co-workers who investigated a series of polyesters with different N_{cc} greater than 14 [212]. Fast ICD can lead to large d_c [48], therefore we see the trend in Figure 7.3. As the polymer crystals are stabilized by d_c (larger d_c, higher T_m according to the Gibbs-Thomson equation), T_m should rise with ICD or N_{cc} as well. Of course, we are also fully aware of the deficiencies of our hypotheses. Choosing similar crystallization temperatures for all polyesters will be ideal because the crystal thickening slope also depends on temperature [66]. There are not enough data points from SAXS measurement of P4HB, so it is difficult to tell the difference in the slope between P4HB and PVL. To confirm our hypothesis further, a polyester with an even larger N_{cc} (> 14) should be investigated.
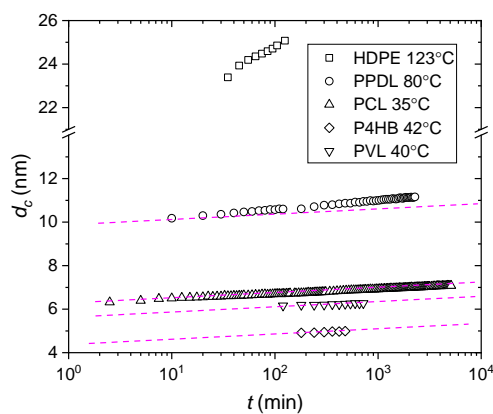
Figure 7.7: d_c of HDPE, PPDL, PCL, PVL and P4HB changes during the isothermal crystallization process in the secondary crystallization phase according to their Porod parameter. The dashed magenta line is the slope of PCL, which is shifted to ease the comparison. PCL data was reproduced from the reference by Schulz and co-workers [48].

7.4.4 What determines shear modulus at a temperature above T_g?

It is well known that for a given semicrystalline polymer, its mechanical modulus, at a temperature above T_g and below T_m, depends on its crystallinity [28, 29, 33]. The dependence is mostly reported by researchers working on PE. We discuss our experimental observations based on aliphatic polyesters here to check the generality of the observation from PE.

The crystallinity (X_c) of PPDL, PVL, P4HB and PGA changes with temperature according to temperature-dependent ^{1}H NMR-FID measurement (Appendix Figure 7.15, confirmed by SAXS and WAXS measurements shown in Appendix Figures 7.20 and 7.21). Although this observation is not yet reported for these polyesters, it is not unexpected for polymers with no measurable ICD due to insertion crystallization [47, 67, 157]. This observation allows us to explore the dependence of the storage shear modulus (G') on X_c of polyesters by simply changing temperatures. We see a linear dependence of G' in logarithmic scale on X_c (G' increases exponentially with X_c) for all polyesters with no measurable ICD in Figure 7.8 (b), which is similar to the observations from PE [28, 29]. Due to the relatively large deviation around the line and the limited range of X_c, the analysis of the exact dependence of G' on X_c can be complicated and is out of the scope of our study. We only intend to demonstrate this trend. Therefore, we consider the semicrystalline morphology ($d_c = 7.9\,\text{nm}, d_a = 1\,\text{nm}$) of P4HB reported by Keridou and co-workers [150, 151] to be questionable for such a low-modulus semicrystalline polymer without measurable ICD. On the other side, G' of polymers with measurable ICD clearly deviates from the trend. This is not contradictory to the generality of the experimental observations from PE. It means when we compare G' of polymers with different levels of ICD, apart from crystallinity, the perturbation frequency should also be taken into account. When the timescale of the perturbation is similar to or slower than that of ICD of a crystal-mobile polymer, its G' is below the trend because the semicrystalline polymer becomes soft due to an α_c-relaxation corresponding to ICD. The examples of frequency-dependent G' of crystal-mobile polymers (HDPE and P3HB) are shown in Appendix Figure 7.22 and Appendix Figures in Chapter 6.

Additionally, Figure 7.8 (a), based on the combination of SAXS and DMA results in Figure 7.2 and Appendix Figure 7.17, respectively, shows no dependence of shear modulus (G') on crystalline layer thickness (d_c). This observation does not agree with the references [30, 31], which claimed that the mechanical modulus was dependent on both d_c and X_c. We know that it is not easy to separate the influence of d_c from X_c if PE is the only sample for this investigation. Our different polyesters provide the possibility to show that there is no influence of d_c on G'.

Put together from the above observations, we complement the general observation from PE that G' relies largely on X_c above T_g, by also taking into account polymer classification (crystal-mobile and crystal-fixed polymers) [29, 33].
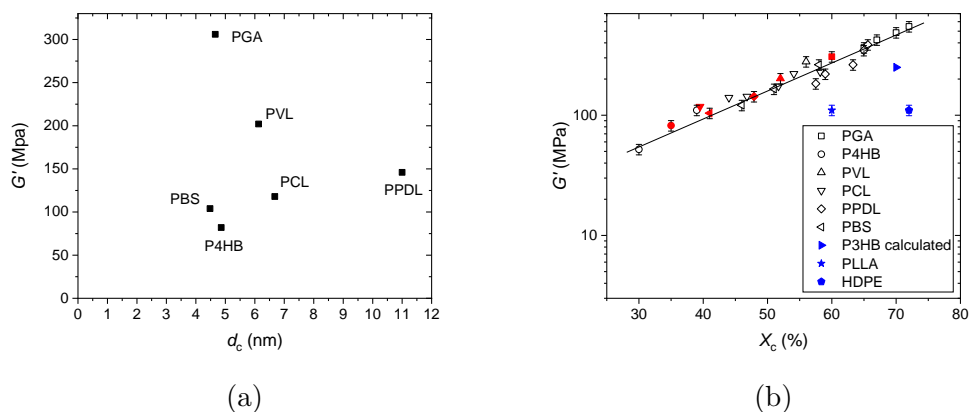
Figure 7.8: (a) Shear modulus (G') vs. d_c of different polyesters. Both modulus and d_c were measured at the corresponding crystallization temperatures. (b) G' vs. X_c (NMR crystallinity) of different polyesters. The red dots represent the measurements at the corresponding isothermal crystallization temperatures. The black dots are measured during a heating or cooling process. The blue dots are from polymers with measurable ICD. PLLA was measured at 130 °C (T_c= 130 °C, 3 h). HDPE was measured at 123 °C (T_c= 123 °C, 2 h). G' from P3HB was calculated from the dynamic Young's modulus. The measurement was performed by Dr. Katalee Jariyavidyanont. The sample was isothermally crystallized P3HB at 140 °C for 40 min. Appendix Figure 7.22 shows a clear dependence of G' of P3HB on frequency. The solid line is as a guide to the eye.

7.5 Summary

In conclusion, with our study of semicrystalline morphology and intracrystalline chain diffusion (ICD) of PGA, P4HB, PVL, PPDL, PLLA and P3HB, we expand the generality of the experimental observations from Boyd to A-B aliphatic polyesters, namely: A-B aliphatic polyesters also follow the observations that high-crystallinity polymers (PLLA and P3HB) possess ICD, while medium-crystallinity polymers (PGA, P4HB, PVL and PPDL) do not show measurable ICD. Due to the presence and absence of ICD, high-crystallinity polyesters show the morphological features: $\sigma_c > \sigma_a$ and medium-crystallinity polyesters show different morphological features: $\sigma_c < \sigma_a$ which also extends the generality of the studies to more polymers.

The broad range of polyesters involved in this study enables us to investigate the influence of chemical structures on ICD of polyesters. On one side, the direct comparison of two pairs of polyesters (PLLA vs. PGA, P3HB vs. P4HB) with and without the CH_3 group as a side chain confirms our first hypothesis that the presence of the CH_3 group as a side chain facilitates ICD of aliphatic polyesters. Therefore, PLLA and P3HB show measurable ICD, while PGA and P4HB do not, according to NMR T_1-relaxation measurement. On the other side, the comparison among P4HB, PVL, PCL, PPDL and HDPE confirms the second hypothesis that ICD slows down when the concentration of ester groups in monomer (inversely proportional to N_{cc}) increases. The systematic increase of N_{cc} from P4HB to HDPE leads to the systematic increase of ICD, which was qualitatively revealed by a systematic increase of the crystal thickening slope of d_c during crystallization and verified by NMR measurements. More importantly, the second hypothesis is not only further supported by the observation of an increase of d_c and T_m from P4HB to HDPE, but also provides an explanation for this increase of d_c and T_m, which is a long-standing observation from the literature without explanations. An increase of ICD (an increase of N_{cc}) is the reason that leads to larger d_c and consequently higher T_m.

With the combination of melting enthalpy measured by DSC and crystallinity by ^{1}H NMR-FID, we extrapolated the measured value of melting enthalpy to the value of a 100% crystalline sample to obtain $\Delta H_{m,100}$. $\Delta H_{m,100}$ from HDPE to P4HB decrease linearly with $1/N_{cc}$, which is due to the penalty of inclusion of the ester group in the crystal. This linear dependence gives us confidence in most of our $\Delta H_{m,100}$ values; meanwhile the dependence also provides guidance to identify reliable $\Delta H_{m,100}$ values.

By measuring the storage shear modulus (G') of the polyesters with different d_c, we excluded the dependence of G' on d_c. We combined temperature-dependent crystallinity measurement and modulus measurement of medium-crystallinity polyesters to report a linear dependence of G' in logarithmic scale on crystallinity (exponential dependence) in the hope of expanding the generality of the dependence of mechanical modulus on the crystallinity observed from PE. The influence of ICD on mechanical modulus should also be taken into account when such a general dependence is explored among polymers with rather different levels of ICD.

With the understanding of the influence of certain chemical structures on in-

tracrystalline chain diffusion of polyesters, we immediately raise a follow-up question: what are the other chemical structures having an influence on the ICD of polyesters and how? Although polyesters are promising materials for the replacement of commodity plastics because of their biodegradability and environmentally friendly monomer source, their relatively inferior mechanical properties (poor balance between elongation at break and modulus), which is highly relevant to ICD, still hinder wide applications of polyesters. The good balance between elongation at break and modulus is usually achieved by the polymers with fast ICD, for instance, PE. Synthesis of polyesters with fast ICD may be a solution to improve the corresponding mechanical properties, which needs to be guided by an understanding of the molecular criteria for the presence of fast ICD.

7.6 Experimental details

This section is different from the Experimental Method Chapter (Chapter 3). All the critical instrumental parameters and sample treatments are reported here with the purposes of data reproduction.

SAXS: SAXS measurements were performed on a Kratky compact camera (Anton Paar GmbH, Graz, Austria) equipped with an X-ray optics (AXO Dresden GmbH, Germany), a temperature-controlled sample holder, and a 1D detector Mythen2 R 1K (Dectris, Switzerland). Samples were heated and cooled in-situ, and illuminated by copper K_α radiation. The exposure time of each measurement was 10 minutes. All samples were heated 20-30 K above their melting temperatures for 10 min and cooled to different isothermal crystallization temperatures with an estimated cooling rate of $5\,\text{K}\,\text{min}^{-1}$.

NMR ^{13}C MAS Spectroscopy: All ^{13}C spectra and data were recorded on a 400 MHz Bruker Avance III spectrometer with a ^{13}C Larmor frequency of 100.6 MHz using double- and triple-resonance MAS probes at a spinning frequency of 10 Hz. Due to the limited available temperature range of the spectrometer, PGA was heated to 250 °C on one hot stage for 10 min and moved to another hot stage of 150 °C immediately for isothermal crystallization for 5 min. Then the sample was cooled to room temperature and transferred to NMR instrument for the measurement. Other polyesters were thermally treated in the instrument. They were heated 20-30 K above their melting temperatures for 10 min and cooled to different isothermal crystallization temperatures. The cooling rate was estimated to be $5\,\text{K}\,\text{min}^{-1}$. Appendix Table 7.1 lists the detailed crystallization conditions, except for the crystallization condition of PGA.

NMR Proton Low-Resolution: ^{1}H time-domain NMR experiments at low field ($B_0 \approx 0.5\,\text{T}$) were performed on a Bruker minispec mq20 spectrometer with a proton frequency of about 20 MHz ($B_0 \approx 0.47\,\text{T}$) using a static probe head with wide temperature range realized by heated or cooled air flow. All samples, except for PGA, were heated 20-30 K above their melting temperatures for 10 min to remove the thermal history and then cooled to different temperatures for isothermal crystallization with an estimated cooling rate of $5\,\text{K}\,\text{min}^{-1}$. PGA was heated up to 250 °C for 10 min in the oven and transferred immediately to the minispec, which was set to 200 °C for isothermal crystallization for 1 h. The stepwise heating for the measurement was carried out at a rate of $\approx 5\,\text{K}\,\text{min}^{-1}$, with an additional 10 min of equilibrium time before each NMR-FID measurement. Appendix Table 7.1 lists the detailed crystallization conditions, except for the thermal treatment of PGA.

DMA: The shear modulus was measured with a rheometer Ares G2 equipped with a heating chamber from TA instruments using a sample in stripe geometry (sample length between clamps 20 mm, width 10 mm, thickness 1.5 mm) at different temperatures but constant frequency of $10\,\text{rad}\,\text{s}^{-1}$ and 0.1% strain. To prepare the samples with stripe geometry, all of them were heated 20-30 K above their melting temperatures for 10 minutes in a rectangular mold (MeltPrep device) and cooled to

different temperatures for isothermal crystallization. The cooling rate was estimated to be $5\,\mathrm{K\,min^{-1}}$.

7.7 Appendix

Polymer	T_c °C	X_c %	ΔH $J\,g^{-1}$	$\Delta H_{m,100}$ $J\,g^{-1}$
PGA	200	60	77.6	129.3

(a) PGA. T_c= 200 °C, 1 h.

Polymer	T_c °C	X_c %	ΔH $J\,g^{-1}$	$\Delta H_{m,100}$ $J\,g^{-1}$
PPDL	80	47.9	101.4	211.7

(b) PPDL, T_c=80 °C, 1 h.

Polymer	T_c °C	X_c %	ΔH $J\,g^{-1}$	$\Delta H_{m,100}$ $J\,g^{-1}$
	40	35	36.1	
P4HB	42	40.1	35.7	96.9 ±7.2
	45	36.5	36	

(c) P4HB, T_c=45 °C, 4 h. T_c=42 °C, 2.5 h. T_c= 40 °C, 2 h.

Polymer	T_c °C	X_c %	ΔH $J\,g^{-1}$	$\Delta H_{m,100}$ $J\,g^{-1}$
	40	52.8	75.3	
PVL	42	54.6	75.9	143.3 ±4.7
	45	48.8	72.4	

(d) PVL, T_c=40 °C, 1 h. T_c=42 °C, 100 min, T_c=45 °C, 200 min.

Table 7.1: NMR crystallinity (X_c) and melting enthalpy (ΔH) of medium-crystallinity polyesters measured by [1] NMR-FID and DSC, respectively, at different isothermal crystallization temperatures. $\Delta H_{m,100}$ is calculated based on $\frac{\Delta H}{X_c}$.
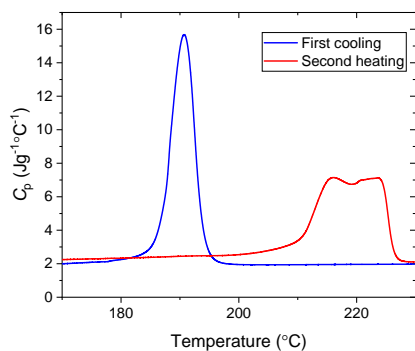
(a) PGA
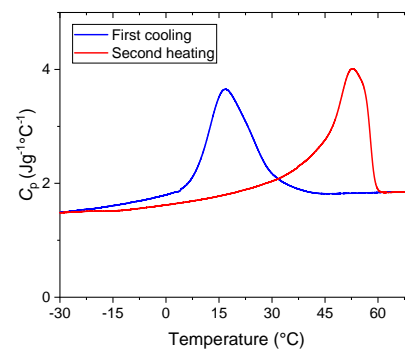
(b) P4HB
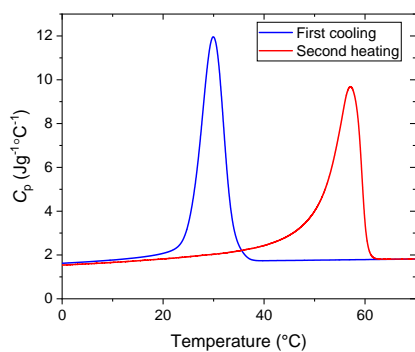
(c) PVL
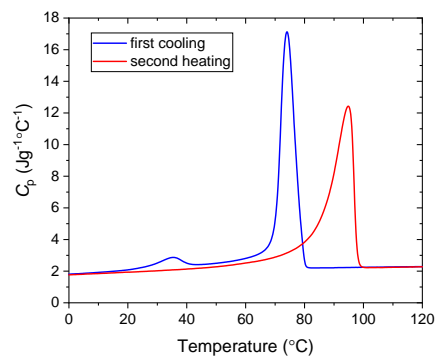
(d) PPDL
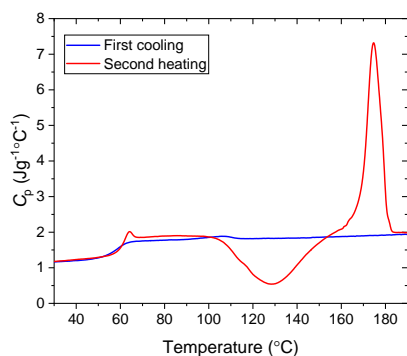
(e) PLLA
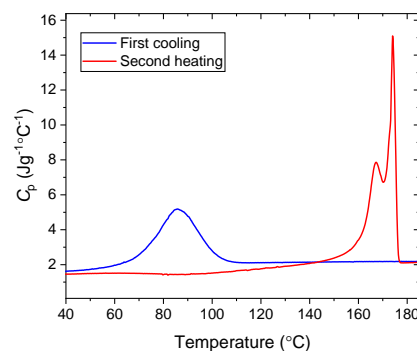
(f) P3HB

Figure 7.1: The first cooling and second heating scans of different polyesters at rate of $10 \, \mathrm{K \, min^{-1}}$ measured by DSC
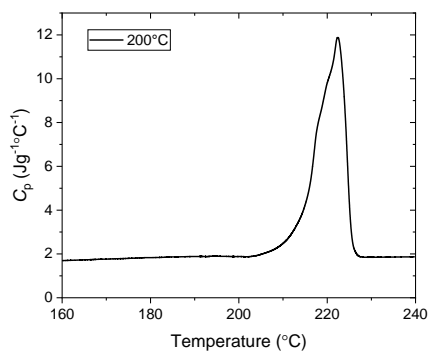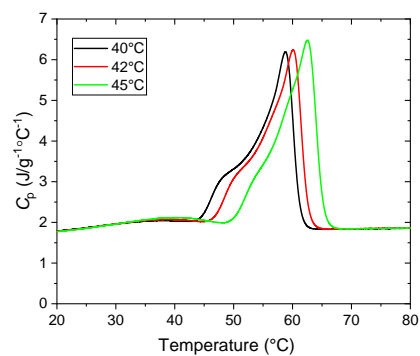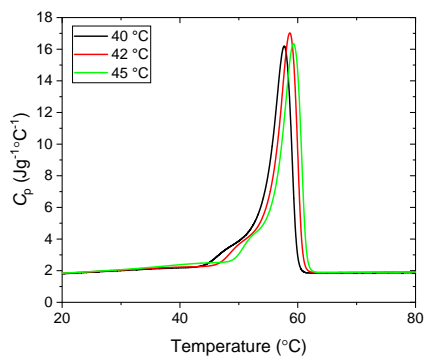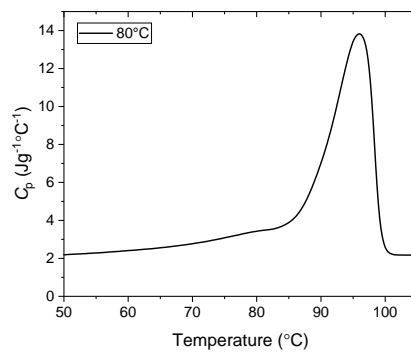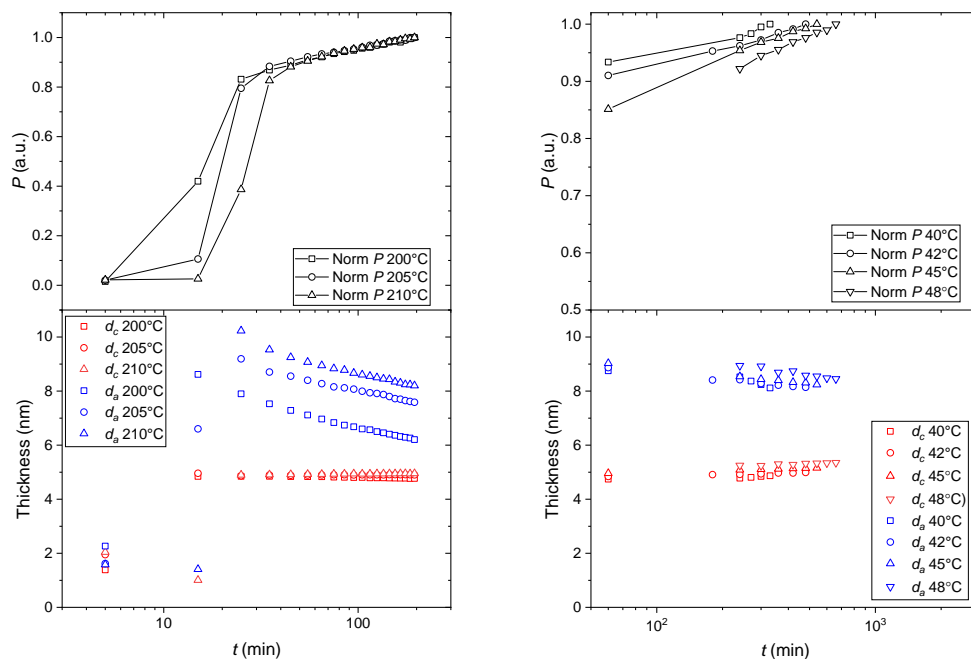
Figure 7.2: The heating scans of medium-crystallinity polyesters after isothermal crystallization at rate of $10\,\mathrm{K\,min^{-1}}$ measured by DSC. The crystallization conditions refer to Appendix Table 7.1.
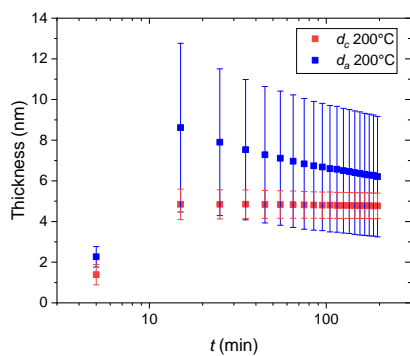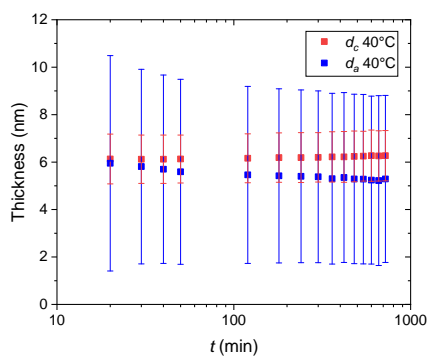
(a) PGA   (b) P4HB

Figure 7.3: The normalized Porod constant (P), d_a and d_c of 4 medium-crystallinity polyesters during the isothermal crystallization process at different temperatures. To ease the reading, σ_a and σ_c are omitted, which are found as examples in Appendix Figure 7.5.
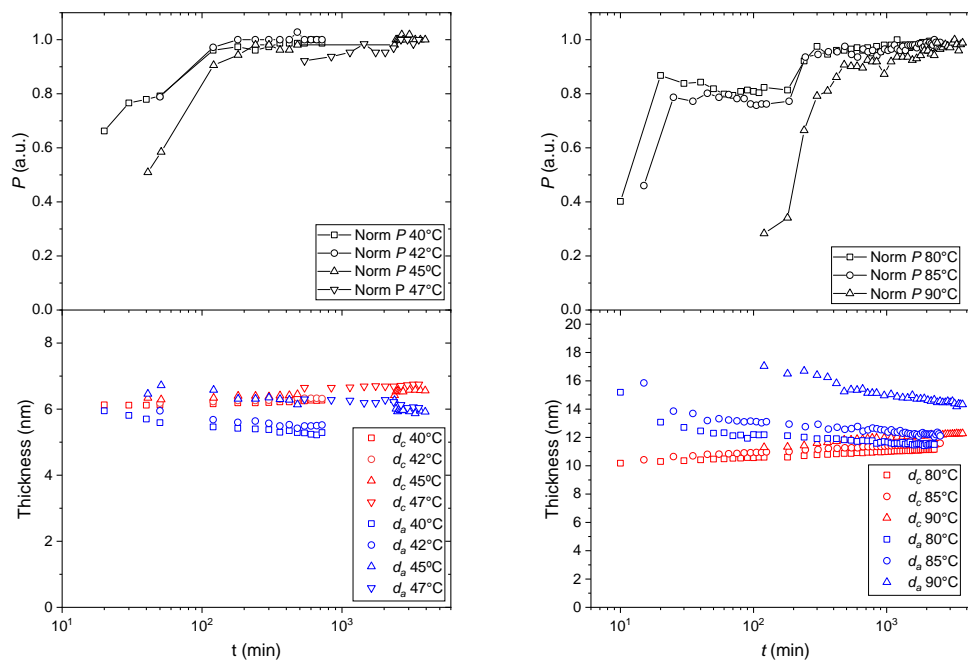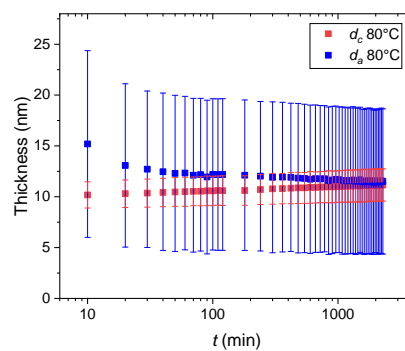
(a) PVL

(b) PPDL

Figure 7.4: The normalized Porod constant (P), d_a and d_c of 4 medium-crystallinity polyesters during the isothermal crystallization process at different temperatures. To ease the reading, σ_a and σ_c are omitted, which are found as examples in Appendix figure 7.5.
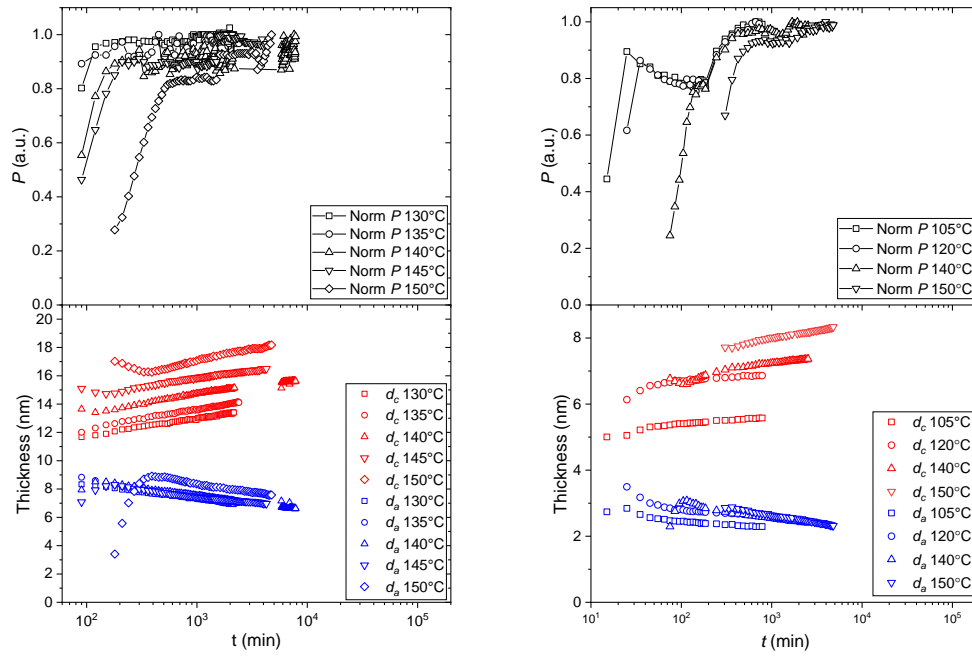
(a) PGA
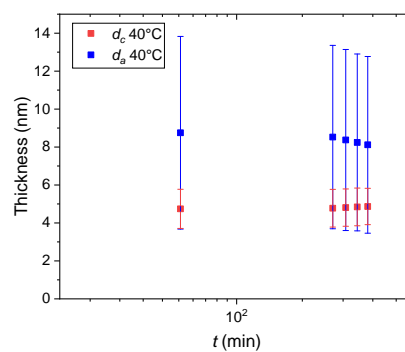
(b) P4HB

(c) PVL

(d) PPDL

Figure 7.5: The selected examples of d_c and d_a of PGA, P4HB, PVL and PPDL during the isothermal crystallization with their distribution width σ_a and σ_c
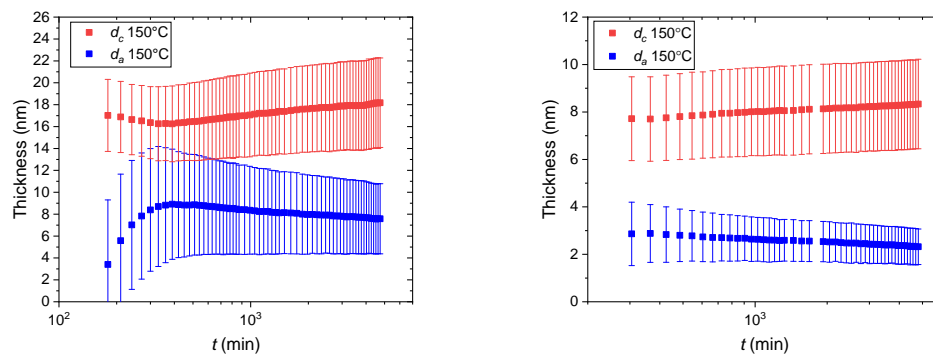
(a) PLLA

(b) P3HB

Figure 7.6: The normalized Porod constant (P), d_a and d_c of 2 high-crystallinity polyesters during the isothermal crystallization process at different temperatures. The initial increase of d_a and decrease of d_c are because of unstable fitting procedure. To ease the reading, σ_a and σ_c are omitted, which are found Appendix Figure 7.7.

(a) PLLA

(b) P3HB

Figure 7.7: The selected examples of d_c and d_a of PLLA and P3HB during the isothermal crystallization with their distribution width σ_a and σ_c. The initial increase of d_a and decrease of d_c are because of unstable fitting procedure.
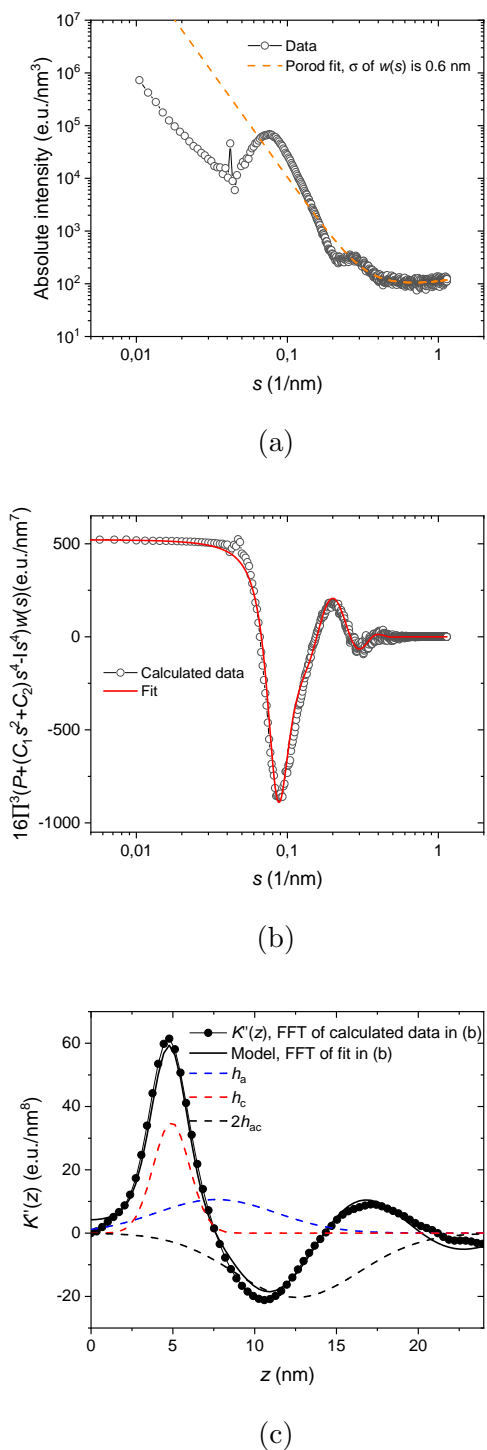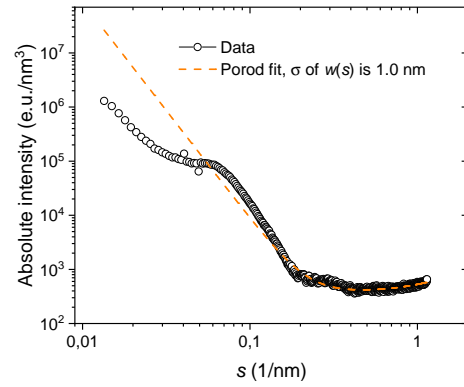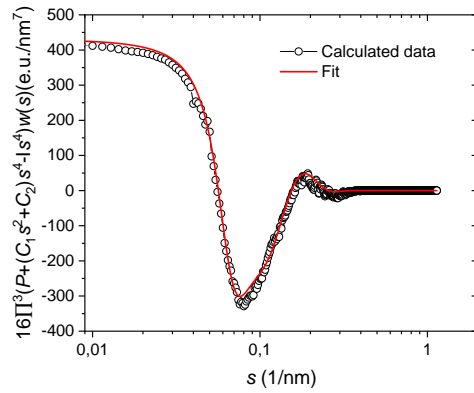
(a)

(b)

(c)

Figure 7.8: (a) I_{abs} and Porod fit of PGA, T_c=200 °C for 175 min (b) $(-I_{abs} + Ps^{-4} + c_1s^2 + c_2)s^4w(s)$ and the fit according to our solution [50], (c) The cosine transformation of the fit and $(-I_{abs} + Ps^{-4} + c_1s^2 + c_2)s^4w(s)$ in (b) and its decomposition in three contributions (dashed lines) h_c, h_a and $2h_{ac}$

(a)

(b)
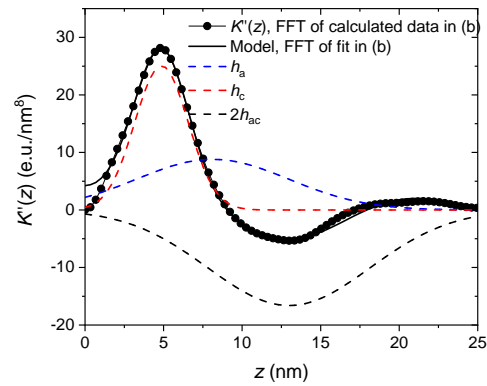
(c)

Figure 7.9: (a) I_{abs} and Porod fit of P4HB, T_c=40 °C for 330 min (b) $(-I_{abs} + Ps^{-4} + c_1 s^2 + c_2)s^4 w(s)$ and the fit according to our solution [50], (c) The cosine transformation of the fit and $(-I_{abs} + Ps^{-4} + c_1 s^2 + c_2)s^4 w(s)$ in (b) and its decomposition in three contributions (dashed lines) h_c, h_a and $2h_{ac}$
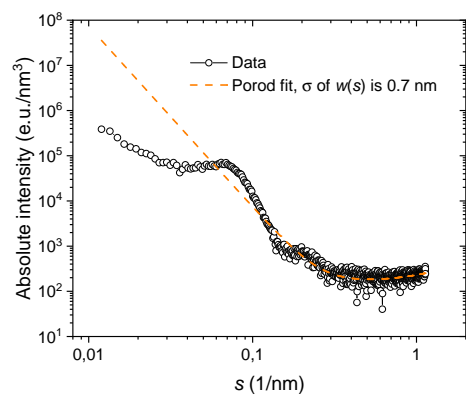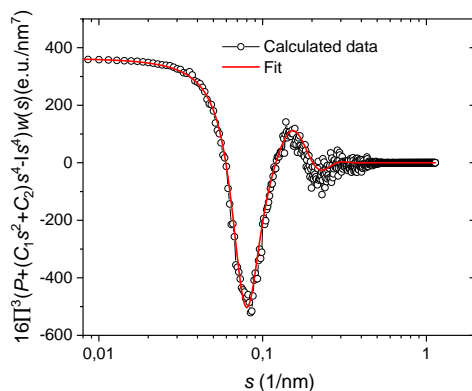
(a)

(b)

(c)

Figure 7.10: (a) I_{abs} and Porod fit of PVL, $T_{\mathrm{c}}{=}40\,^{\circ}\mathrm{C}$ for $12\,\mathrm{h}$ (b) $(-I_{\mathrm{abs}}{+}Ps^{-4}{+}c_1s^2{+}c_2)s^4w(s)$ and the fit according to our solution [50], (c) The cosine transformation of the fit and $(-I_{\mathrm{abs}} + Ps^{-4} + c_1s^2 + c_2)s^4w(s)$ in (b) and its decomposition in three contributions (dashed lines) h_{c}, h_{a} and $2h_{\mathrm{ac}}$

(a)

(b)
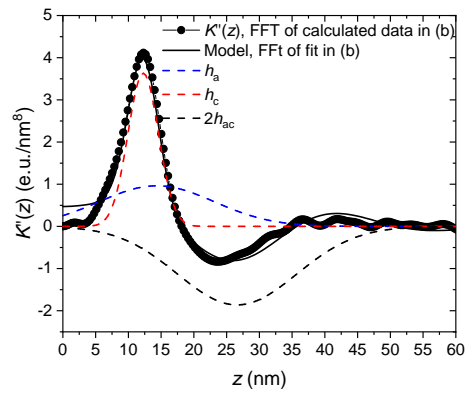
(c)

Figure 7.11: (a) I_{abs} and Porod fit of PPDL, T_{c}=90 °C for 3720 min (b) (-$I_{\mathrm{abs}} + Ps^{-4} + c_1 s^2 + c_2)s^4 w(s)$ and the fit according to our solution [50], (c) The cosine transformation of the fit and $(-I_{\mathrm{abs}} + Ps^{-4} + c_1 s^2 + c_2)s^4 w(s)$ in (b) and its decomposition in three contributions (dashed lines) h_{c}, h_{a} and $2h_{\mathrm{ac}}$
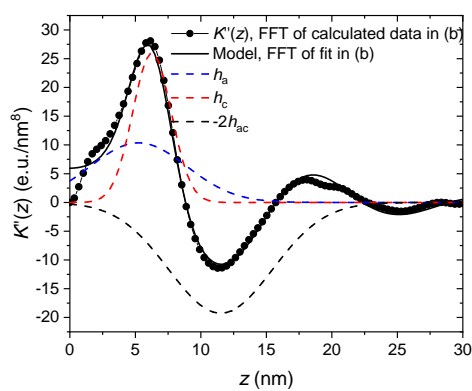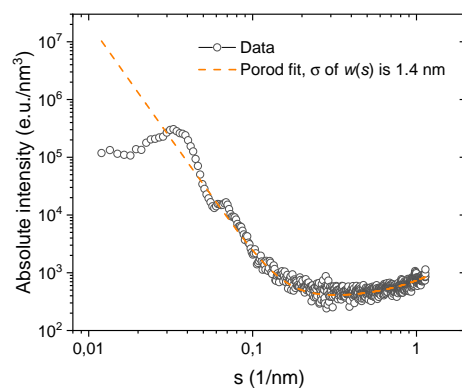
(a)
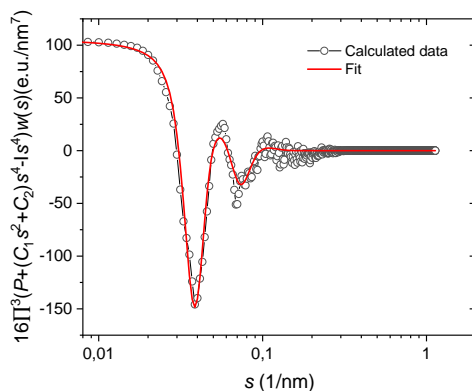
(b)
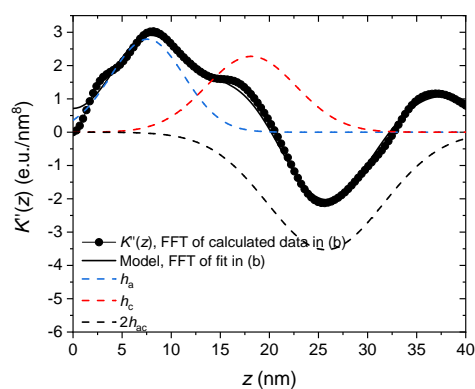
(c)

Figure 7.12: (a) I_{abs} and Porod fit of PLLA, T_{c}=150 °C for 4800 min (b) (-$I_{\mathrm{abs}} + Ps^{-4} + c_1 s^2 + c_2)s^4 w(s)$ and the fit according to our solution [50], (c) The cosine transformation of the fit and $(-I_{\mathrm{abs}} + Ps^{-4} + c_1 s^2 + c_2)s^4 w(s)$ in (b) and its decomposition in three contributions (dashed lines) h_{c}, h_{a} and $2h_{\mathrm{ac}}$
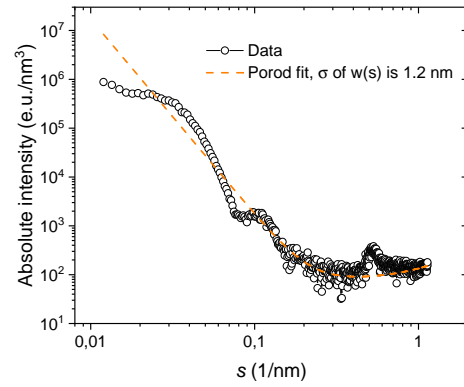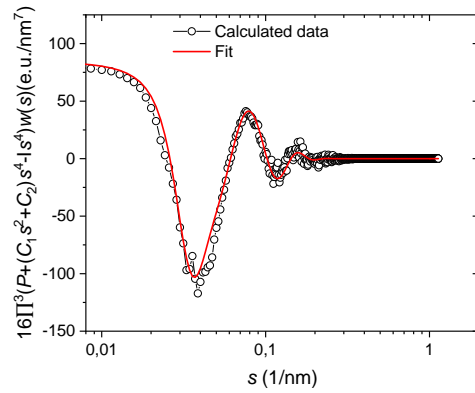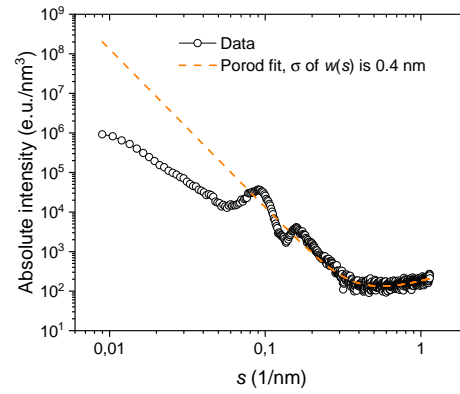
(a)
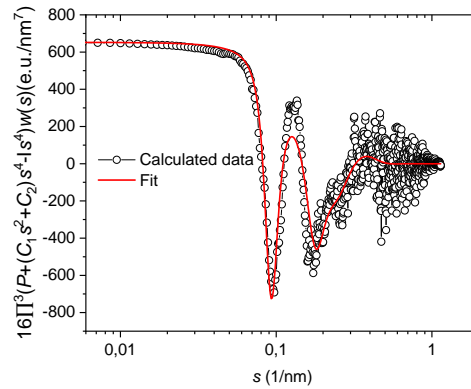
(b)
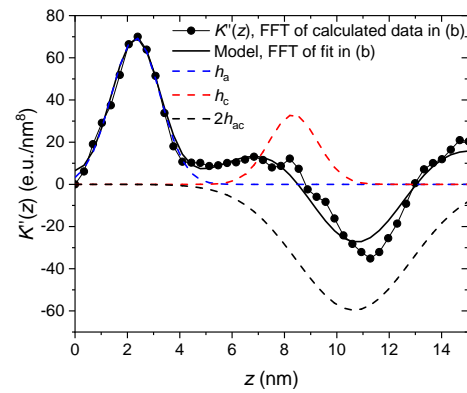
(c)

Figure 7.13: (a) I_{abs} and Porod fit of P3HB, T_{c}=150 °C for 72 h (b) ($-I_{\text{abs}} + Ps^{-4} + c_1 s^2 + c_2)s^4 w(s)$ and the fit according to our solution [50], (c) The cosine transformation of the fit and ($-I_{\text{abs}} + Ps^{-4} + c_1 s^2 + c_2)s^4 w(s)$ in (b) and its decomposition in three contributions (dashed lines) h_{c}, h_{a} and $2h_{\text{ac}}$
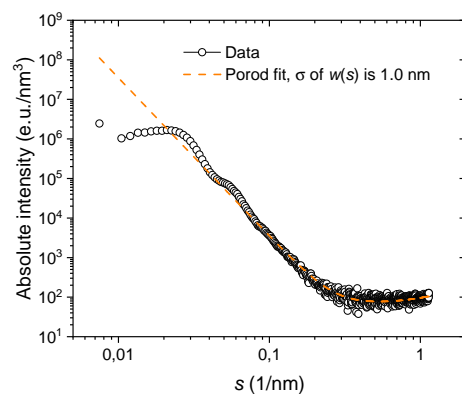
(a)
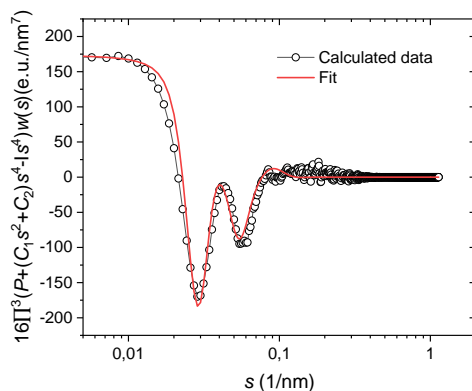
(b)
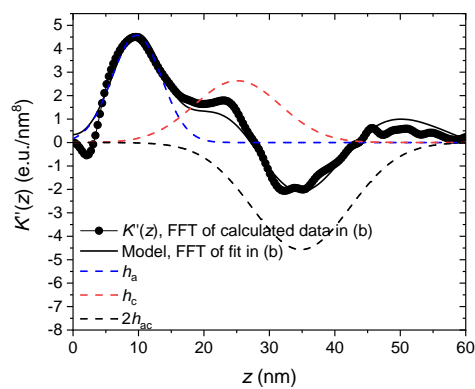
(c)

Figure 7.14: (a) I_{abs} and Porod fit of P3HB, T_c=123 °C for 150 min (b) ($-I_{abs} + Ps^{-4} + c_1 s^2 + c_2)s^4 w(s)$ and the fit according to our solution [50], (c) The cosine transformation of the fit and $(-I_{abs} + Ps^{-4} + c_1 s^2 + c_2)s^4 w(s)$ in (b) and its decomposition in three contributions (dashed lines) h_c, h_a and $2h_{ac}$
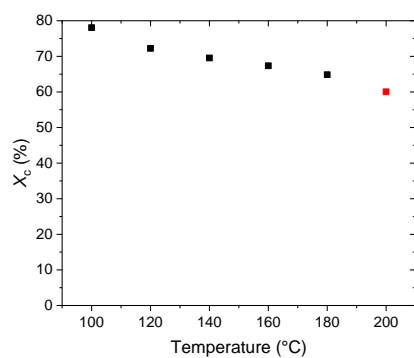
(a) PGA
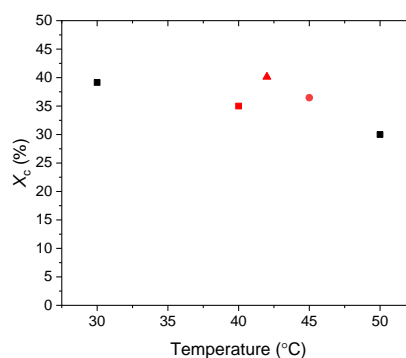
(b) P4HB
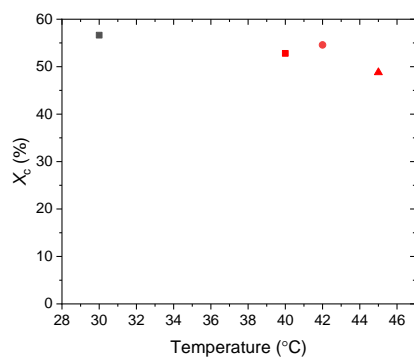
(c) PVL
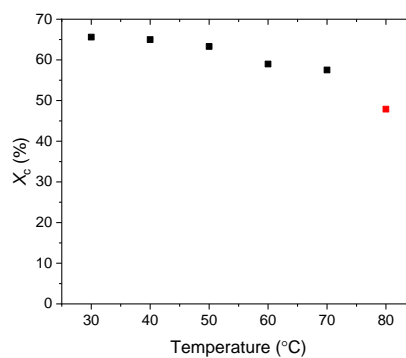
(d) PPDL

Figure 7.15: The crystallinity (X_c) of PGA, P4HB, PVl and PPDL vs. temperature measured by NMR-FID. The red dots were measured at different isothermal crystallization temperatures. The black dots were measured during cooling or heating process. The crystallization conditions refer to Appendix Table 7.1.

(a) PGA

(b) P4HB

(c) PVL
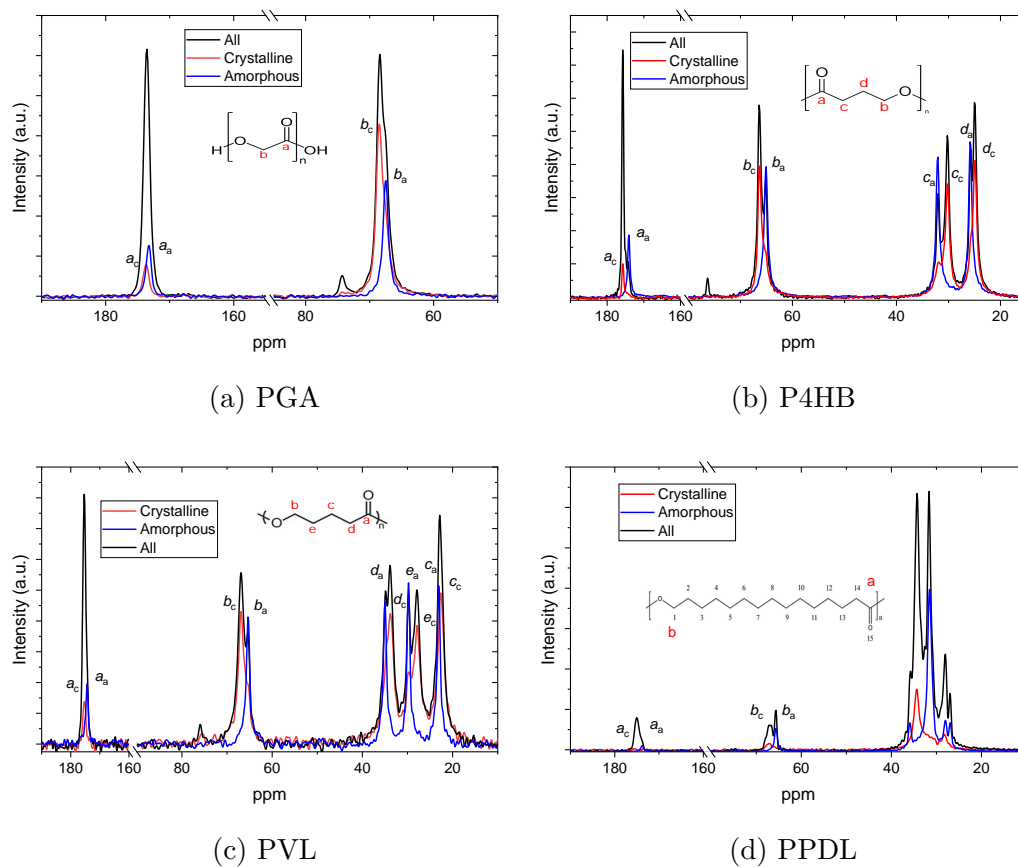
(d) PPDL

Figure 7.16: Comparison of ^{13}C spectra of PGA (a), P4HB (b), PVL (c) and PPDL (d): the amorphous (subscripts a) and crystalline (subscripts c) contributions of ^{13}C spectra are in blue and red, respectively, the total contribution (amorphous and crystalline) is in black. The inset in each figure shows the assignment of the ^{13}C peaks.

(a) PGA

(b) P4HB

(c) PVL

(d) PPDL

(e) HDPE
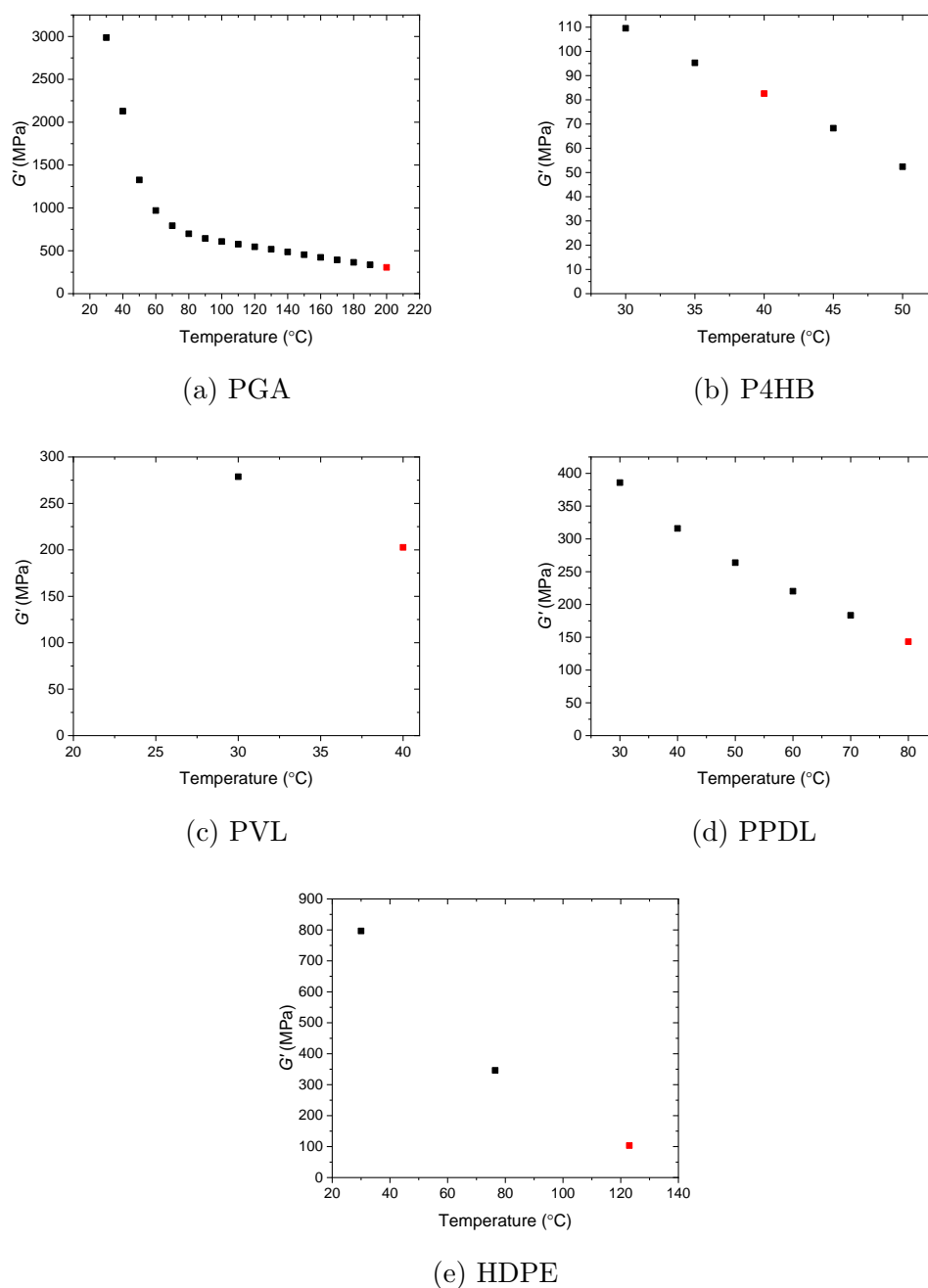
Figure 7.17: The dependence of G' of different polyesters on temperature measured at the frequency of 10 Hz and the strain of 0.1 %. The red dots were measured at different isothermal crystallization temperatures. The black dots were measured during a cooling or heating process. The crystallization conditions refer to Appendix Table 7.1. PPDL was crystallized for 90 min instead of 60 min at 80 °C. HDPE was crystallized at 123 °C for 2 h.
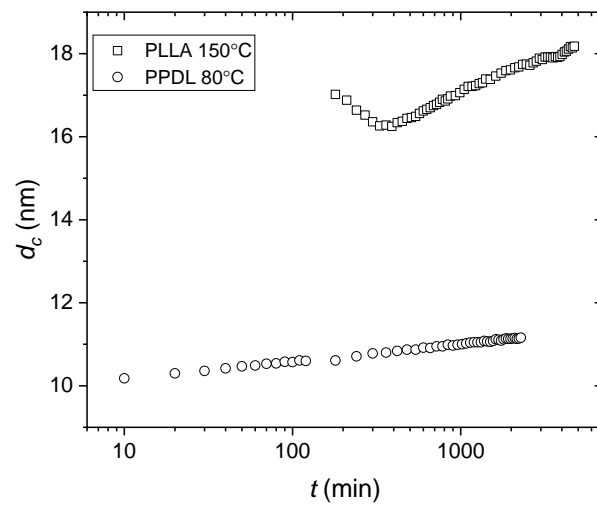
Figure 7.18: The difference of crystal thickening of PPDL and PLLA

(a) PGA

(b) P4HB

(c) PVL

(d) PPDL
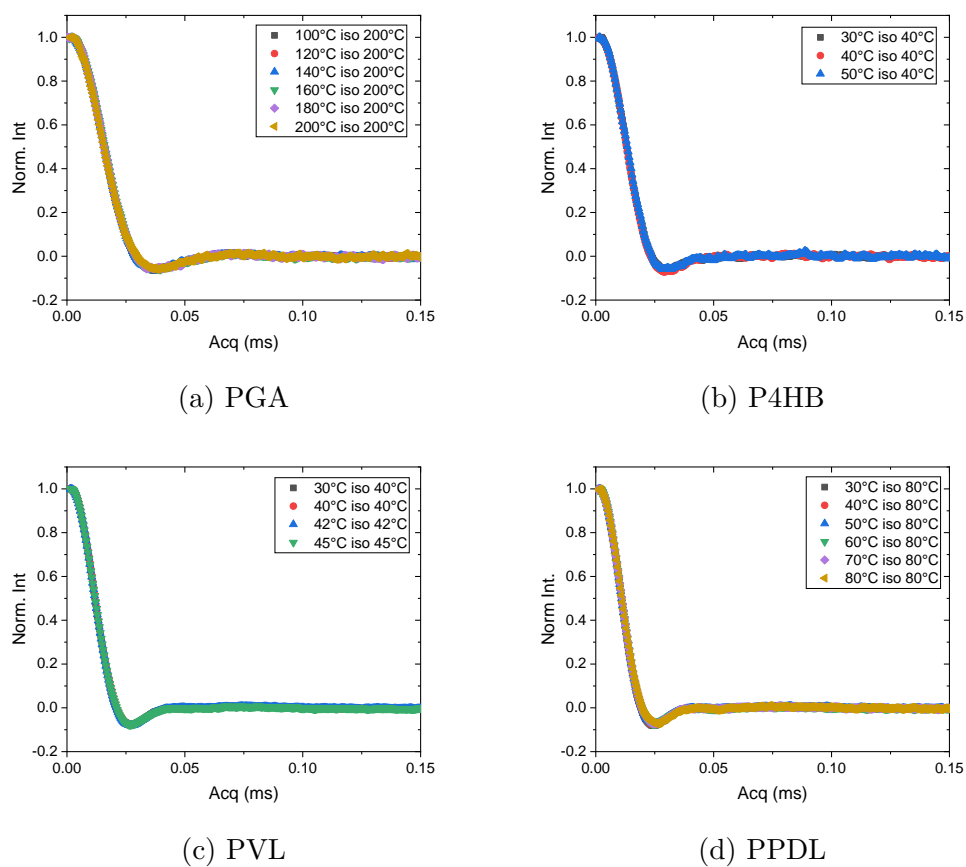
Figure 7.19: The crystalline component of ^{1}H NMR-FID measurement of medium-crystallinity polyesters. No change in crystalline line shape with temperatures in these polymers is observed, indicating no ICD in the fast timescale. The first temperature in the legend refers to measurement temperature. The second temperature refers to crystallization temperatures.
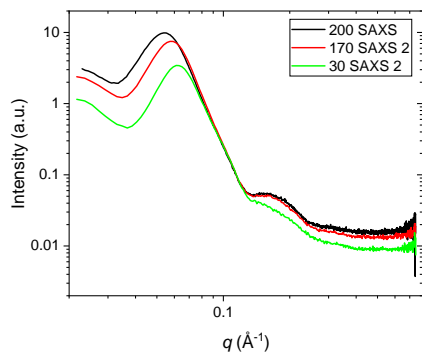
(a) PGA SAXS
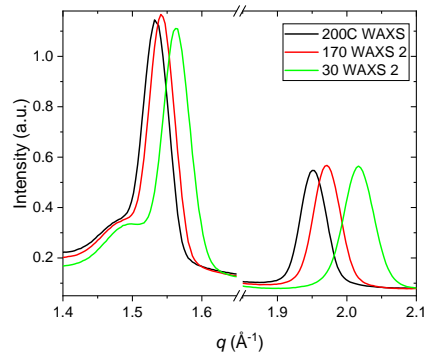
(b) PGA WAXS
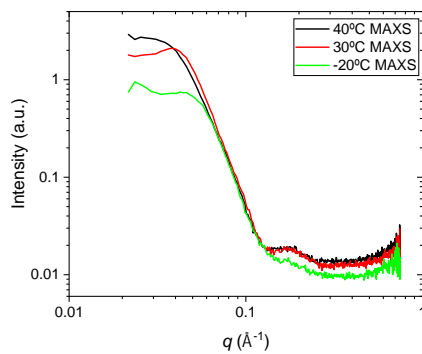
(c) P4HB SAXS
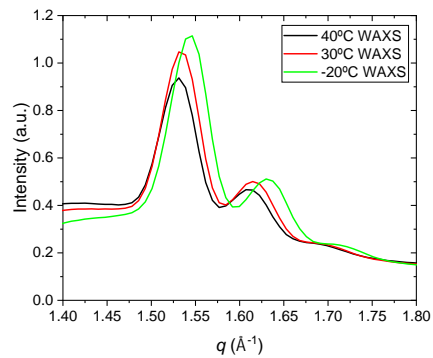
(d) P4HB SAXS

Figure 7.20: SAXS and WAXS of PGA (T_c= 200 °C, 2 h) and P4HB (T_c= 40 °C, 2 h) at different temperatures. SAXS and WAXS experiments were carried out in micro-focus instrument.

(a) PVL SAXS

(b) PVL WAXS

(c) PPDL SAXS

(d) PPDL WAXS
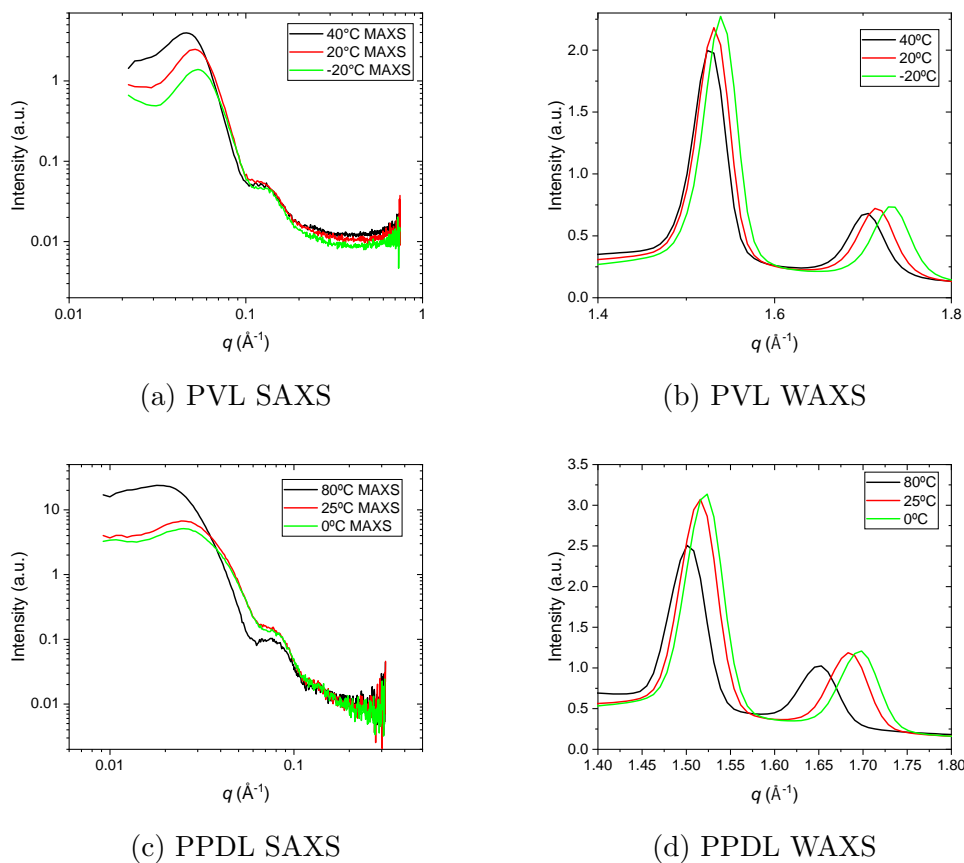
Figure 7.21: SAXS and WAXS of PVL (T_c= 40 °C, 1 h) and PPDL (T_c= 80 °C, 1 h) at different temperatures. SAXS and WAXS experiments were carried out in micro-focus instrument.
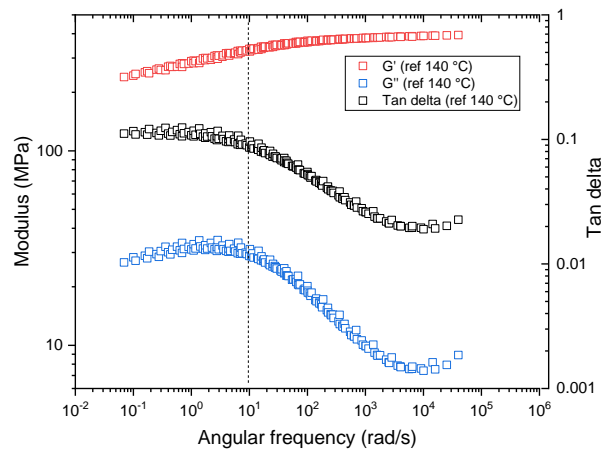
Figure 7.22: The master curve of P3HB at a reference temperature of $140\,^{\circ}\mathrm{C}$, measured by DMA (Ares G2). The sample was non-isothermally crystallized, measured at a strain of 0.1%.

Chapter 8

Summary and outlook

The main motivation of this work was to check whether our proposals from previous studies [47, 48] regarding the dependence of the morphological features of semicrystalline polymers (d_c, d_a, σ_c and σ_a) on Intracrystalline Chain Diffusion (ICD) are also valid in aliphatic polyesters. d_c and d_a are the average crystalline and amorphous layer thickness, σ_c and σ_a are the distribution width of d_c and d_a. We proposed that the semicrystalline polymers possessing measurable ICD (crystal-mobile polymers) show typical morphological features: $d_\text{c} > d_\text{a}$, $\sigma_\text{c} > \sigma_\text{a}$, while the semicrystalline polymers possessing no measurable ICD (crystal-fixed polymers) demonstrate another typical morphological features: $d_\text{c} < d_\text{a}$, $\sigma_\text{c} < \sigma_\text{a}$. The measurable ICD refers to $\langle \tau_\text{c} \rangle$ (the monomer jump correlation time, which is the average residence time of a monomer in a given crystal raster position) up to 1 s measured by NMR. If $\langle \tau_\text{c} \rangle$ is longer than 1 s, it is not measurable by NMR. The detailed investigations on two commercially available polyesters, PBS (Poly Butylene Succinate) and P3HB (Poly-3-hydroxybutyrate), reveal that PBS is a crystal-fixed polymer and P3HB is a crystal-mobile polymer. Their morphological features are the same as predicted by our proposals. Through further investigations of all the other aliphatic polyesters in this work, on one side, we confirm the generality of our proposals regarding semicrystalline morphology and ICD in the polyesters. On the other side, we also confirm the robustness of our two methodologies (NMR and SAXS) and the consistency between them in terms of crystallinity (X_c).

With the reliable determination of the crystallinity (X_c) of all the samples in a broad temperature range (from room temperature to crystallization temperature, T_c), it is quantitatively proved that crystal-fixed polymers show temperature-dependent X_c. X_c decreases when temperature increases, and vice versa, due to the formation of insertion crystallization during cooling and the melting of the corresponding crystals formed by insertion crystallization during heating. The process of the formation and the melting of the crystals is temperature-reversible. To make use of the temperature-dependent X_c further, we also reveal that the shear modulus (G') of all crystal-fixed polymers investigated in this study has an exponential dependence on X_c above T_g. However, the crystal-mobile polymers from this work do not follow this dependence,

but show lower G' due to the presence of an α_c-relaxation process corresponding to ICD.

In addition, this work was also motivated by a long-standing question: whether there are molecular criteria for the presence of ICD in polymers or not. Therefore, a series of aliphatic polyesters with similar chemical structures were studied. These samples differ from each other by the number of CH_2 groups along the main chain (N_{cc}) or by the presence or absence of the CH_3 group as a side chain. Firstly, we observe that the aliphatic polyesters with CH_3 group as side chain possess measurable ICD, while their counterparts without the CH_3 group as a side chain do not. However, further investigations are needed, as it is rather difficult to distinguish whether it is the CH_3 group or chain conformation or the combination of both that leads to the measurable ICD. Secondly, although the aliphatic polyesters containing no CH_3 group as a side chain, with different N_{cc}, do not have measurable ICD, we observe that these polyesters demonstrate different crystal thickening slopes (determined from a plot of d_c versus crystallization time at an isothermal crystallization temperature). We consider the difference in crystal thickening slope as qualitative evidence of different ICDs in the timescale of $\langle \tau_c \rangle$ larger than $1\,\mathrm{s}$. The greater the slope is, the faster ICD is. The slope increases with N_{cc}. The extreme case is PE (possesses very fast ICD), of which N_{cc} is infinite. As a result of the dependence of ICD ($\langle \tau_c \rangle > 1\,\mathrm{s}$) of the polyesters on N_{cc}, d_c has the dependence on N_{cc} as well. The polymer crystals are stabilized by d_c (larger d_c, higher stability). Therefore, the larger N_{cc} is, the higher the melting temperature (T_m) is. Apart from T_m and d_c, we also notice that the enthalpy of melting ($\Delta H_{m,100}$) is inversely proportional to $1/N_{cc}$.

In conclusion, this work successfully proves the generality of our proposals regarding semicrystalline morphology and ICD in aliphatic polyesters. An exponential dependence of G' of the polyesters without measurable ICD on crystallinity is demonstrated. We hypothesize that N_{cc} and CH_3 are likely to be the molecular criteria for ICD, with which the dependence of d_c and T_m on N_{cc} can be reasonably explained.

A few scientific questions from our study still open for future work. The robustness of the molecular criteria on ICD of aliphatic polyesters from our hypothesis needs to be further confirmed. Regarding the hypothesis about the effect of N_{cc} on ICD, it can be checked by investigating another one or two aliphatic polyesters with rather large N_{cc} (much more than 15) by NMR, SAXS and DMA measurement. It is also meaningful to include the new samples into the study, to check the dependence of d_c, T_m and $\Delta H_{m,100}$ on N_{cc}. To verify the hypothesis about the effect of the CH_3 group as a side chain on ICD, β form crystal of Polyglycol Acid (PGA), which forms helical chain conformation can be a good candidate for the study (its α form does not possess measurable ICD). In general, the molecular criteria of ICD for aliphatic polyesters are our research direction in the future. With the understanding of the criteria, the synthesis of aliphatic polyesters can be guided to adjust their mechanical properties. The combination of large elongation at break and high modulus is usually one of the preferred mechanical properties for many applications, which are often achieved

by crystal-mobile polymers (PE, PP (Polypropylene), etc.). To replace commodity plastic in many applications, aliphatic polyesters are supposed to demonstrate similar mechanical properties. However, due possibly to rather slow ICD or the absence of ICD, aliphatic polyesters show always short elongation at break. In order to expand the applications of aliphatic polyesters, the synthesis of aliphatic polyesters with fast ICD is, very likely, a solution. Of course, we have to admit that the exact mechanism leading to short elongation at break is quite complex and can be the combination of several factors, but ICD is an important one of them.

Bibliography

[1] Joris Mercelis. *Beyond Bakelite: Leo Baekeland and the Business of Science and Invention.* The MIT Press, Cambridge, Massachusetts London, England, 2020.

[2] D. B. Malpass. *Introduction to Industrial Polyethylene: Properties, Catalysts, and Processes.* Scrivener Publishing LLC Co-published by John Wiley & Sons, Salem, Massachusetts (LLC) Hoboken, New Jersey (Wiley), 2010.

[3] D. B. Malpass and Elliot I. Band. *Introduction to Industrial Polypropylene ; Properties, Catalysts Processes.* Scrivener Publishing LLC Co-published by John Wiley & Sons, Inc., Salem, Massachusetts (LLC) Hoboken, New Jersey (Wiley), 2012.

[4] N. Wyeth and R. Roseveare. Biaxially oriented poly(ethylene terephthalate)bottle (u.s. patent no.3733309a), 1973.

[5] Sten Gustaf Thulin. Bag with handle of weldable plastic material (u.s. patent no.3180557a), 1965.

[6] R. Geyer, J.R. Jambeck, and K.L. Law. Production, use, and fate of all plastics ever made. *Law Sci. Adv*, 3:e1700782–+, 2017.

[7] David K. A. Barnes, Francois Galgani, Richard C. Thompson, and Morton Barlaz. Accumulation and fragmentation of plastic debris in global environments. *Philosophical Transactions of the Royal Society B: Biological Sciences*, 364(1526):1985–1998, 2009.

[8] Balint Simon. What are the most significant aspects of supporting the circular economy in the plastic industry? *Resources, Conservation and Recycling*, 141:299–300, 2019.

[9] Wanda Sikorska, Marta Musioł, Barbara Zawidlak-Wegrzynska, and Joanna Rydz. End-of-life options for (bio)degradable polymers in the circular economy. *Advances in Polymer Technology*, 2021(1):6695140, 2021.

[10] Manuel Häußler, Marcel Eck, Dario Rothauer, and Stefan Mecking. Closed-loop recycling of polyethylene-like materials. *Nature*, 590(7846):423–427, 2021.

[11] Amnat Jarerat, Yutaka Tokiwa, and Hideo Tanaka. Production of poly(l-lactide)-degrading enzyme by amycolatopsis orientalis for biological recycling of poly(l-lactide). *Applied Microbiology and Biotechnology*, 72(4):726–731, 2006.

[12] Sophie Grima, Véronique Bellon-Maurel, Pierre Feuilloley, and Françoise Silvestre. Aerobic biodegradation of polymers in solid-state conditions: A review of environmental and physicochemical parameter settings in laboratory simulations. *Journal of Polymers and the Environment*, 8(4):183–195, 2000.

[13] Md Salatul Islam Mozumder, Linsey Garcia-Gonzalez, Heleen De Wever, and Eveline I. P. Volcke. Poly(3-hydroxybutyrate) (phb) production from co2: Model development and process optimization. *Biochemical Engineering Journal*, 98:107–116, 2015.

[14] Jan-Georg Rosenboom, Robert Langer, and Giovanni Traverso. Bioplastics for a circular economy. *Nature Reviews Materials*, 7(2):117–137, 2022.

[15] Shuliang Chen, Xin Zhang, Mingyang He, and Jinchun Li. Degradation of pga, prepared by reactive extrusion polymerization, in water, humid, and dry air, and in a vacuum. *Journal of Materials Research*, 35(14):1846–1856, 2020.

[16] Katsuyuki Mukai, Kenji Yamada, and Yoshiharu Doi. Kinetics and mechanism of heterogeneous hydrolysis of poly[(r)-3-hydroxybutyrate] film by pha depolymerases. *International Journal of Biological Macromolecules*, 15(6):361–366, 1993.

[17] M. B. Tekman, B. A. Walther, C. Peter, L. Gutow, and M. Bergmann. Impacts of plastic pollution in the oceans on marine species, biodiversity and ecosystems. Report, Alfred Wegener Institut, Zentrum für Polar- und Meeresforschung, 2022.

[18] Iteb Boughattas, Sabrine Hattab, Nesrine Zitouni, Marouane Mkhinini, Omayma Missawi, Noureddine Bousserrhine, and Mohamed Banni. Assessing the presence of microplastic particles in tunisian agriculture soils and their potential toxicity effects using eisenia andrei as bioindicator. *Science of The Total Environment*, 796:148959, 2021.

[19] Eddie F. Gómez and Frederick C. Michel. Biodegradability of conventional and bio-based plastics and natural fiber composites during composting, anaerobic digestion and long-term soil incubation. *Polymer Degradation and Stability*, 98(12):2583–2591, 2013.

[20] Irena Wojnowska-Baryła, Katarzyna Bernat, and Magdalena Zaborowska. Plastic waste degradation in landfill conditions: The problem with microplastics, and their direct and indirect environmental effects. *International Journal of Environmental Research and Public Health*, 19(20):13223, 2022.

[21] Pinjing He, Liyao Chen, Liming Shao, Hua Zhang, and Fan Lü. Municipal solid waste (msw) landfill: A source of microplastics? -evidence of microplastics in landfill leachate. *Water Research*, 159:38–45, 2019.

[22] Rui M. S. Cruz, Victoria Krauter, Simon Krauter, Sofia Agriopoulou, Ramona Weinrich, Carsten Herbes, Philip B. V. Scholten, Ilke Uysal-Unalan, Ece Sogut, Samir Kopacic, Johanna Lahti, Ramune Rutkaite, and Theodoros Varzakas. Bioplastics for food packaging: Environmental impact, trends and regulatory aspects. *Foods*, 11(19):3087, 2022.

[23] S. M. Satti and A. A. Shah. Polyester-based biodegradable plastics: an approach towards sustainable development. *Letters in Applied Microbiology*, 70(6):413–430, 2020.

[24] Ardra Nandakumar, Jo-Ann Chuah, and Kumar Sudesh. Bioplastics: A boon or bane? *Renewable and Sustainable Energy Reviews*, 147:111237, 2021.

[25] Xiaoying Zhao, Katrina Cornish, and Yael Vodovotz. Narrowing the gap for bioplastic use in food packaging: An update. *Environmental Science & Technology*, 54(8):4712–4732, 2020.

[26] Mohammad Peydayesh, Massimo Bagnani, and Raffaele Mezzenga. Sustainable bioplastics from amyloid fibril-biodegradable polymer blends. *ACS Sustainable Chemistry & Engineering*, 9(35):11916–11926, 2021.

[27] Katrin Molina-Besch and Hannah Keszleri. Exploring the industrial perspective on biobased plastics in food packaging applications – insights from sweden. *Sustainable Production and Consumption*, 35:72–84, 2023.

[28] Z. Bartczak and M. Kozanecki. Influence of molecular parameters on high-strain deformation of polyethylene in the plane-strain compression. part i. stress–strain behavior. *Polymer*, 46(19):8210–8221, 2005.

[29] F.J. Stadler, J. Kaschta, and H. Münstedt. Dynamic-mechanical behavior of polyethylenes and ethene-/alpha-olefin-co-polymers. part i. alpha '-relaxation. *Polymer*, 46(23):10311–10320, 2005.

[30] J. Molnár, A. Hertner-Horváth, and A. Menyhárd. Prediction of tensile modulus from calorimetric melting curves of polylactic acid with pronounced cold crystallization ability. *Polymer Testing*, 95:107112, 2021.

[31] Ali Zarbali, Ilies Djaffar, and Alfréd Menyhárd. Prediction of tensile modulus based on parameters of crystalline structure in polyethylene terephthalate with cold crystallization ability. *Heliyon*, 10(4):e26122, 2024.

[32] Zefan Wang, Mareen Schaller, Albrecht Petzold, Kay Saalwächter, and Thomas Thurn-Albrecht. How entanglements determine the morphology of semicrystalline polymers. *Proceedings of the National Academy of Sciences*, 120(27):e2217363120, 2023.

[33] S. Humbert, O. Lame, R. Seguela, and G. Vigier. A re-examination of the elastic modulus dependence on crystallinity in semi-crystalline polymers. *Polymer*, 52(21):4899–4909, 2011.

[34] Yongfeng Men, Jens Rieger, Hans Friedlich Endeler, and Dieter Lilge. Mechanical alpha-process in polyethylene. *Macromolecules*, 36(13):4689–4691, 2003.

[35] Xiaoliang Tang, Wei Chen, and Liangbin Li. The tough journey of polymer crystallization: Battling with chain flexibility and connectivity. *Macromolecules*, 52(10):3575–3591, 2019.

[36] Kay Saalwächter, Thomas Thurn-Albrecht, and Wolfgang Paul. Recent progress in understanding polymer crystallization. *Macromolecular Chemistry and Physics*, n/a(n/a):2200424, 2023.

[37] J.D. Hoffman and J.I. Lauritzen. Crystallization of bulk polymers with chain folding: Theory of growth of lamellar spherulites. *Journal of Research of the National Bureau of Standards*, A 65(4):297–336, 1961.

[38] D.M. Sadler and G.H. Gilmer. Rate-theory model of polymer crystallization. *Physical Review Letters*, 56(25):2708–2711, 1986.

[39] David M. Sadler. New explanation for chain folding in polymers. *Nature*, 326:174–177, 1987.

[40] S. Stepanow. Kinetic mechanism of chain folding in polymer crystallization. *Physical Review e*, 90(3):032601–+, 2014.

[41] E. Robelin-Souffache and J. Rault. Origin of the long period and crystallinity in quenched semicrystalline polymers 1. *Macromolecules*, 22(9):3581–3594, 1989.

[42] M. Hikosaka. Unified theory of nucleation of folded-chain crystals and extended-chain crystals of linear-chain polymers. *Polymer*, 28(8):1257–1264, 1987.

[43] X.M. Jiang, G. Reiter, and W.B. Hu. How chain-folding crystal growth determines the thermodynamic stability of polymer crystals. *Journal of Physical Chemistry B*, 120(3):566–571, 2016.

[44] A. Keller, M. Hikosaka, S. Rastogi, A. Toda, P. J. Barham, and G. Goldbeck-Wood. An approach to the formation and growth of new phases with application to polymer crystallization - effect of finite-size, metastability, and ostwald rule of stages. *Journal of Materials Science*, 29(10):2579–2604, 1994.

[45] G. Strobl. From the melt via mesomorphic and granular crystalline layers to lamellar crystallites: A major route followed in polymer crystallization? *Eur. Phys. J. E*, 3:165–183, 2000.

[46] G. Strobl. Colloquium: Laws controlling crystallization and melting in bulk polymers. *Reviews of Modern Physics*, 81(3):1287–1300, 2009.

[47] M. Schulz, A. Seidlitz, R. Kurz, R. Barenwald, A. Petzold, K. Saalwachter, and T. Thurn-Albrecht. The underestimated effect of intracrystalline chain dynamics on the morphology and stability of semicrystalline polymers. *Macromolecules*, 51(21):8377–8385, 2018.

[48] Martha Schulz, Mareen Schäfer, Kay Saalwächter, and Thomas Thurn-Albrecht. Competition between crystal growth and intracrystalline chain diffusion determines the lamellar thickness in semicrystalline polymers. *Nature Communications*, 13(1):119, 2022.

[49] Martha Schulz. *Einfluss intrakristalliner Dynamik auf Morphologie und Schmelzverhalten teilkristalliner Polymere [Kumulative Dissertation]*. Dissertation, 2021.

[50] Anne Seidlitz and Thomas Thurn-Albrecht. *Small-Angle X-ray Scattering for Morphological Analysis of Semicrystalline Polymers*, pages 151–164. 2016.

[51] Ulf W. Gedde. *Polymer physics*. Chapman and Hall, London [u.a.], 1. ed edition, 1995.

[52] W.G. Hu and K. Schmidt-Rohr. Polymer ultradrawability: the crucial role of alpha-relaxation chain mobility in the crystallites. *Acta Polymerica*, 50(8):271–285, 1999.

[53] Stephanie F. Marxsen, Manuel Häuβler, Stefan Mecking, and Rufina G. Alamo. Isothermal step thickening in a long-spaced aliphatic polyester. *Polymer*, 191:122282, 2020.

[54] Mark P. F. Pepels, Leon E. Govaert, and Rob Duchateau. Influence of the main-chain configuration on the mechanical properties of linear aliphatic polyesters. *Macromolecules*, 48(16):5845–5854, 2015.

[55] Yu Song, Ziwen Ma, Peng Yang, Xiaoye Zhang, Xiujuan Lyu, Ke Jiang, and Wenke Zhang. Single-molecule force spectroscopy study on force-induced melting in polymer single crystals: The chain conformation matters. *Macromolecules*, 52(3):1327–1333, 2019.

[56] S. Koltzenburg, M. Maskos, and O. Nuyken. *Polymer Chemistry*. Springer, Berlin, Heidelberg, Germany, 2017.

[57] J. Scheiers and T. E. Long. *Modern Polyesters: Chemistry and Technology of Polyesters and Copolyesters.* John Wiley & Sons Ltd, Chichester, 2003.

[58] Bernhard Rieger, Andreas Künkel, Geoffrey W. Coates, Robert Reichardt, Eckhard Dinjus, and Thomas A. Zevaco. *Synthetic Biodegradable Polymers.* Advances in Polymer Science. Springer, Heidelberg, Dordrecht, London, New York, 2012.

[59] Andrzej Hofman, Ryszard Szymański, Stanislaw Słomkowski, and Stanislaw Penczek. Structure of active species in the cationic polymerization of beta-propiolactone and epsilon-caprolactone. *Die Makromolekulare Chemie*, 185(4):655–667, 1984.

[60] Hans R. Kricheldorf, J. Michael Jonte, and Ruth Dunsing. Polylactones, 7a) the mechanism of cationic polymerization of beta-propiolactone and epsilon-caprolactone. *Die Makromolekulare Chemie*, 187(4):771–785, 1986.

[61] Gert Strobl. *The physics of polymers. Concepts for understanding their structures and behavior.* Springer, Berlin [u.a.], 3., rev. and expanded ed. edition, 2007.

[62] K. J. Fritzsching, K. Mao, and K. Schmidt-Rohr. Avoidance of density anomalies as a structural principle for semicrystalline polymers: The importance of chain ends and chain tilt. *Macromolecules*, 50(4):1521–1540, 2017.

[63] G. Strobl and T.Y. Cho. Growth kinetics of polymer crystals in bulk. *European Physical Journal e*, 23(1):55–65, 2007.

[64] Muhammad Tariq. *Thermodynamics and kinetics of interface-induced crystallization.* Dissertation, 2021.

[65] Herve Marand, Jiannong Xu, and Srivatsan Srinivas. Determination of the equilibrium melting temperature of polymer crystals: Linear and nonlinear hoffman-weeks extrapolations. *Macromolecules*, 31(23):8219–8229, 1998.

[66] J. J. Weeks. Melting temperature and change of lamellar thickness with time for bulk polyethylene. *J Res Natl Bur Stand A Phys Chem*, 67A(5):441–451, 1963.

[67] Qiang Yu, Afiq Anuar, Albrecht Petzold, Jens Balko, Kay Saalwächter, and Thomas Thurn-Albrecht. The semicrystalline morphology of polybutylene succinate supports a general scheme based on intracrystalline dynamics. *Macromolecular Chemistry and Physics*, n/a(n/a):2200459, 2023.

[68] R.J. Roe. *Methods of X-ray and neutron scattering in polymer science / Ryong-Joon Roe.* Topics in polymer science. Oxford Univ. Press, New York, 2000.

[69] W. Ruland. X-ray determination of crystallinity and diffuse disorder scattering. *Acta Crystallographica*, 14(11):1180–1185, 1961.

[70] J. Keeler. *Understanding NMR Spectroscopy*. Wiley, Chichester, 2nd edition, 2010.

[71] Dennis A. Torchia. The measurement of proton-enhanced carbon-13 t1 values by a method which suppresses artifacts. *Journal of Magnetic Resonance (1969)*, 30(3):613–616, 1978.

[72] Kerstin Schäler, Matthias Roos, Peter Micke, Yury Golitsyn, Anne Seidlitz, Thomas Thurn-Albrecht, Horst Schneider, Guenter Hempel, and Kay Saalwächter. Basic principles of static proton low-resolution spin diffusion nmr in nanophase-separated materials with mobility contrast. *Solid State Nuclear Magnetic Resonance*, 72:50–63, 2015.

[73] R. Kurz, A. Achilles, W. Chen, M. Schäfer, A. Seidlitz, Y. Golitsyn, J. Kressler, W. Paul, G. Hempel, T. Miyoshi, T. Thurn-Albrecht, and K. Saalwächter. Intracrystalline jump motion in poly(ethylene oxide) lamellae of variable thickness: A comparison of nmr methods. *Macromolecules*, 50(10):3890–3902, 2017.

[74] K. Schmidt-Rohr and H.W. Spiess. Chain diffusion between crystalline and amorphous regions in polyethylene detected by 2d exchange c-13 nmr. *Macromolecules*, 24(19):5288–5293, 1991.

[75] E.R. DeAzevedo, W.G. HU, T.J. Bonagamba, and K. Schmidt-Rohr. Centerband-only detection of exchange: Efficient analysis of dynamics in solids by nmr. *J. Am. Chem. Soc*, 121(36):8411–8412, 1999.

[76] Afiq Anuar, Qiang Yu, Katalee Jariyavidyanont, Albrecht Petzold, René Androsch, Thomas Thurn-Albrecht, and Kay Saalwächter. Poly-3-hydroxybutyrate, a crystal-mobile biodegradable polyester. *Macromolecules*, 0(0):null, 2024.

[77] Y.F. Yao, R. Graf, H.W. Spiess, D.R. Lippits, and S. Rastogi. Morphological differences in semicrystalline polymers: Implications for local dynamics and chain diffusion. *Physical Review e*, 76(6):060801–+, 2007.

[78] M. Rubinstein and R. H. Colby. *Polymer Physics*. Oxford University Press, Oxford, 2004.

[79] Alejandro J. Müller and Rose Mary Michell. *Differential Scanning Calorimetry of Polymers*, book section 5, pages 72–99. John Wiley & Sons, Inc, 2016.

[80] L. C. Sawyer, D. T. Grubb, and G. F. Meyers. Polymer microscopy, 2008.

[81] Wallace H. Carothers, G. L. Dorough, and F. J. van Natta. Studies of polymerization and ring formation. x. the reversible polymerization of six-membered cyclic esters. *Journal of the American Chemical Society*, 54(2):761–772, 1932.

[82] Kazuyuki Yamane, Hiroyuki Sato, Yukio Ichikawa, Kazuhiko Sunagawa, and Yoshiki Shigaki. Development of an industrial production technology for high-molecular-weight polyglycolic acid. *Polymer Journal*, 46(11):769–775, 2014.

[83] Yoshito Ikada and Hideto Tsuji. Biodegradable polyesters for medical and ecological applications. *Macromolecular Rapid Communications*, 21(3):117–132, 2000.

[84] Chitoshi Nakafuku and Hitomichi Yoshimura. Melting parameters of poly(glycolic acid). *Polymer*, 45(11):3583–3585, 2004.

[85] C. C. Chu. Hydrolytic degradation of polyglycolic acid: Tensile strength and crystallinity study. *Journal of Applied Polymer Science*, 26(5):1727–1734, 1981.

[86] Jiapeng Zhang, Bowen Xie, Zhenhao Xi, Ling Zhao, Lian Cen, and Ying Yang. A comparable study of polyglycolic acid's degradation on macrophages' activation. *Materials Science and Engineering: C*, 109:110574, 2020.

[87] Peter B. Maurus and Christopher C. Kaeding. Bioabsorbable implant material review. *Operative Techniques in Sports Medicine*, 12(3):158–160, 2004.

[88] Deyu Niu, Hai Wang, Ye Ma, Pengwu Xu, Jiaxuan Li, Weijun Yang, Tianxi Liu, Kohji Tashiro, Pieter Jan Lemstra, and Piming Ma. A β-form crystal modification of poly(glycolic acid): Formation, stabilization, and β–α transition. *Macromolecules*, 56(16):6316–6327, 2023.

[89] Yôzô Chatani, Kazuaki Suehiro, Yasuo Ôkita, Hiroyuki Tadokoro, and Kiyoshi Chujo. Structural studies of polyesters. i. crystal structure of polyglycolide. *Die Makromolekulare Chemie*, 113(1):215–229, 1968.

[90] J. E. Mark. *Polymer Data Handbook*. Oxford University Press, Inc., New York u.a., 2$^{\text{nd}}$ edition, 2009.

[91] Fumita Nishimura, Hiromichi Hoshina, Yukihiro Ozaki, and Harumi Sato. Isothermal crystallization of poly(glycolic acid) studied by terahertz and infrared spectroscopy and saxs/waxd simultaneous measurements. *Polymer Journal*, 51(2):237–245, 2019.

[92] Harumi Sato, Mai Miyada, Shigeki Yamamoto, Kummetha Raghunatha Reddy, and Yukihiro Ozaki. C–h$\cdots$o (ether) hydrogen bonding along the (110) direction in polyglycolic acid studied by infrared spectroscopy, wide-angle x-ray diffraction, quantum chemical calculations and natural bond orbital calculations. *RSC Advances*, 6(20):16817–16823, 2016.

[93] Chengtao Yu, Jianna Bao, Qing Xie, Guorong Shan, Yongzhong Bao, and Pengju Pan. Crystallization behavior and crystalline structural changes of poly(glycolic acid) investigated via temperature-variable waxd and ftir analysis. *CrystEngComm*, 18(40):7894–7902, 2016.

[94] Yongxuan Chen, Kefeng Xie, Yucheng He, and Wenbing Hu. Fast-scanning chip-calorimetry measurement of crystallization kinetics of poly(glycolic acid). *Polymers*, 13(6):891, 2021.

[95] K. Chujo, H. Kobayashi, J. Suzuki, S. Tokuhara, and M. Tanabe. Ring-opening polymerization of glycolide. *Die Makromolekulare Chemie*, 100(1):262–266, 1967.

[96] D. K. Gilding and A. M. Reed. Biodegradable polymers for use in surgery—polyglycolic/poly(actic acid) homo- and copolymers: 1. *Polymer*, 20(12):1459–1464, 1979.

[97] D. Cohn, H. Younes, and G. Marom. Amorphous and crystalline morphologies in glycolic acid and lactic acid polymers. *Polymer*, 28(12):2018–2022, 1987.

[98] H. Montes de Oca, I. M. Ward, R. A. Chivers, and D. F. Farrar. Structure development during crystallization and solid-state processing of poly(glycolic acid). *Journal of Applied Polymer Science*, 111(2):1013–1018, 2009.

[99] H. Montes de Oca, I. M. Ward, P. G. Klein, M. E. Ries, J. Rose, and D. Farrar. Solid state nuclear magnetic resonance study of highly oriented poly(glycolic acid). *Polymer*, 45(21):7261–7272, 2004.

[100] H. Montes de Oca and I. M. Ward. Structure and mechanical properties of pga crystals and fibres. *Polymer*, 47(20):7070–7077, 2006.

[101] Sokei Sekine, Hideyuki Akieda, Isao Ando, and Tetsuo Asakura. A study of the relationship between the tensile strength and dynamics of as-spun and drawn poly(glycolic acid) fibers. *Polymer Journal*, 40(1):10–16, 2008.

[102] T. Angelin Swetha, V. Ananthi, Abhispa Bora, Nallathambi Sengottuvelan, Kumar Ponnuchamy, Govarthanan Muthusamy, and A. Arun. A review on biodegradable polylactic acid (pla) production from fermentative food waste - its applications and degradation. *International Journal of Biological Macromolecules*, 234:123703, 2023.

[103] Erwin T. H. Vink, Karl R. Rábago, David A. Glassner, and Patrick R. Gruber. Applications of life cycle assessment to natureworks™ polylactide (pla) production. *Polymer Degradation and Stability*, 80(3):403–419, 2003.

[104] Masoud Razavi, Wenwen Zhang, Hossein Ali Khonakdar, Andreas Janke, Liang-bin Li, and Shi-Qing Wang. Inducing nano-confined crystallization in plla and pet by elastic melt stretching. *Soft Matter*, 17(6):1457–1462, 2021.

[105] Lebo Xu, Kaitlyn Crawford, and Christopher B. Gorman. Effects of temperature and ph on the degradation of poly(lactic acid) brushes. *Macromolecules*, 44(12):4777–4782, 2011.

[106] Imania Ghaffar, Muhammad Rashid, Muhammad Akmal, and Ali Hussain. Plastics in the environment as potential threat to life: an overview. *Environmental Science and Pollution Research*, 29(38):56928–56947, 2022.

[107] Katarzyna Krasowska and Aleksandra Heimowska. Degradability of polylactide in natural aqueous environments. *Water*, 15(1):198, 2023.

[108] James Lunt. Large-scale production, properties and commercial applications of polylactic acid polymers. *Polymer Degradation and Stability*, 59(1):145–152, 1998.

[109] N A Weir, F J Buchanan, J F Orr, and G R Dickson. Degradation of poly-l-lactide. part 1: in vitro and in vivo physiological temperature degradation. *Proceedings of the Institution of Mechanical Engineers, Part H: Journal of Engineering in Medicine*, 218(5):307–319, 2004.

[110] Moataz A. Elsawy, Ki-Hyun Kim, Jae-Woo Park, and Akash Deep. Hydrolytic degradation of polylactic acid (pla) and its composites. *Renewable and Sustainable Energy Reviews*, 79:1346–1352, 2017.

[111] P. De Santis and A. J. Kovacs. Molecular conformation of poly(s-lactic acid). *Biopolymers*, 6(3):299–306, 1968.

[112] Katalee Jariyavidyanont, Andreas Janke, Qiang Yu, Thomas Thurn-Albrecht, and René Androsch. Lamellar morphology of disorder $\alpha\prime$-crystals of poly(l-lactic acid). *Crystal Growth & Design*, 2024.

[113] Kaewkan Wasanasuk and Kohji Tashiro. Crystal structure and disorder in poly(l-lactic acid) δ form ($\alpha\prime$ form) and the phase transition mechanism to the ordered α form. *Polymer*, 52(26):6097–6109, 2011.

[114] B. Eling, S. Gogolewski, and A. J. Pennings. Biodegradable materials of poly(l-lactic acid): 1. melt-spun and solution-spun fibres. *Polymer*, 23(11):1587–1593, 1982.

[115] L. Cartier, T. Okihara, Y. Ikada, H. Tsuji, J. Puiggali, and B. Lotz. Epitaxial crystallization and crystalline polymorphism of polylactides. *Polymer*, 41(25):8909–8919, 2000.

[116] René Androsch, Maria Laura Di Lorenzo, and Christoph Schick. Crystal nucleation in random l/d-lactide copolymers. *European Polymer Journal*, 75:474–485, 2016.

[117] Katalee Jariyavidyanont, Mengxue Du, Qiang Yu, Thomas Thurn-Albrecht, Christoph Schick, and René Androsch. Bulk enthalpy of melting of poly (l-lactic acid) (plla) determined by fast scanning chip calorimetry. *Macromolecular Rapid Communications*, n/a(n/a):2200148, 2022.

[118] Hideki Abe, Yoshihiro Kikkawa, Yoshio Inoue, and Yoshiharu Doi. Morphological and kinetic analyses of regime transition for poly[(s)-lactide] crystal growth. *Biomacromolecules*, 2(3):1007–1014, 2001.

[119] Hideki Abe, Mariko Harigaya, Yoshihiro Kikkawa, Takeharu Tsuge, and Yoshiharu Doi. Crystal growth and solid-state structure of poly(lactide) stereocopolymers. *Biomacromolecules*, 6(1):457–467, 2005.

[120] Hideto Tsuji and Yoshito Ikada. Properties and morphologies of poly(l-lactide): 1. annealing condition effects on properties and morphologies of poly(l-lactide). *Polymer*, 36(14):2709–2716, 1995.

[121] Tai-Yon Cho and Gert Strobl. Temperature dependent variations in the lamellar structure of poly(l-lactide). *Polymer*, 47(4):1036–1043, 2006.

[122] Wei Chen, Wenxuan Zhou, Yuta Makita, Shijun Wang, Shichen Yuan, Takashi Konishi, and Toshikazu Miyoshi. Characterization of the slow molecular dynamics of poly(l-lactic acid) in α and $\alpha\prime$ phases, in a glassy state, and in a complex with poly(d-lactic acid) by solid-state nmr. *Macromolecular Chemistry and Physics*, 219(3):1700451, 2018.

[123] W. Chen, D. Reichert, and T. Miyoshi. Helical jump motions of poly(l-lactic acid) chains in the alpha phase as revealed by solid-state nmr. *Journal of Physical Chemistry B*, 119(12):4552–4563, 2015.

[124] D. Byrom. Polymer synthesis by microorganisms: technology and economics. *Trends in Biotechnology*, 5(9):246–250, 1987.

[125] Xiaoyan Tang and Eugene Y. X. Chen. Chemical synthesis of perfectly isotactic and high melting bacterial poly(3-hydroxybutyrate) from bio-sourced racemic cyclic diolide. *Nature Communications*, 9(1):2345, 2018.

[126] Mariane I. Alves, Karine L. Macagnan, Amanda A. Rodrigues, Dener A. de Assis, Matheus M. Torres, Patrícia D. de Oliveira, Lígia Furlan, Claire T. Vendruscolo, and Angelita da S. Moreira. Poly(3-hydroxybutyrate)-p(3hb): Review of production process technology. *Industrial Biotechnology*, 13(4):192–208, 2017.

[127] C. Schick, A. Wurm, and A. Mohamed. Vitrification and devitrification of the rigid amorphous fraction of semicrystalline polymers revealed from frequency-dependent heat capacity. *Colloid & Polymer Sci*, 279(8):800–806, 2001.

[128] A. Czerniecka, A. Magoń, J. Schliesser, B. F. Woodfield, and M. Pyda. Heat capacity of poly(3-hydroxybutyrate). *The Journal of Chemical Thermodynamics*, 73:76–84, 2014.

[129] Zhiyong Wei, Lian Liu, and Min Qi. Synthesis and characterization of homo- and co-polymers of (r,s)-β-butyrolactone and γ-butyrolactone or β-valerolactone initiated with cyclic tin alkoxide. *Reactive and Functional Polymers*, 66(12):1411–1419, 2006.

[130] Amin Cao, Naoki Asakawa, Naoko Yoshie, and Yoshio Inoue. Phase structure and biodegradation of the bacterial poly(3-hydroxybutyric acid)/chemosynthetic poly(3-hydroxypropionic acid) blend. *Polymer Journal*, 30(9):743–752, 1998.

[131] G. Q. Chen, Q. Wu, Y. K. Jung, and S. Y. Lee. *3.21 - PHA/PHB*, pages 217–227. Academic Press, Burlington, 2011.

[132] Lorena R. Lizarraga-Valderrama, Rinat Nigmatullin, Caroline Taylor, John W. Haycock, Frederik Claeyssens, Jonathan C. Knowles, and Ipsita Roy. Nerve tissue engineering using blends of poly(3-hydroxyalkanoates) for peripheral nerve regeneration. *Engineering in Life Sciences*, 15(6):612–621, 2015.

[133] G. J. M. de Koning. *Embrittlement and Rejuvenation of Bacterial Poly[(R)-3-hydroxybutyrate]*, volume 575 of *ACS Symposium Series*, book section 13, pages 188–201. American Chemical Society, 1994.

[134] M. Yokouchi, Y. Chatani, H. Tadokoro, K. Teranishi, and H. Tani. Structural studies of polyesters: 5. molecular and crystal structures of optically active and racemic poly (β-hydroxybutyrate). *Polymer*, 14(6):267–272, 1973.

[135] Tadahisa Iwata, Masahiro Fujita, Yoshihiro Aoyagi, Yoshiharu Doi, and Tetsuro Fujisawa. Time-resolved x-ray diffraction study on poly[(r)-3-hydroxybutyrate] films during two-step-drawing: generation mechanism of planar zigzag structure. *Biomacromolecules*, 6(3):1803–1809, 2005.

[136] Harumi Sato, Rumi Murakami, Adchara Padermshoke, Fuminobu Hirose, Kenichi Senda, Isao Noda, and Yukihiro Ozaki. Infrared spectroscopy studies of ch· · ·o hydrogen bondings and thermal behavior of biodegradable poly(hydroxyalkanoate). *Macromolecules*, 37(19):7203–7213, 2004.

[137] Ahmed Mohamed El-Hadi Abdel Ghaffar. *Development of a biodegradable material based on poly (3-hydroxybutyrate) PHB*. Thesis, 2002.

[138] P. J. Barham, A. Keller, E. L. Otun, and P. A. Holmes. Crystallization and morphology of a bacterial thermoplastic: poly-3-hydroxybutyrate. *Journal of Materials Science*, 19(9):2781–2794, 1984.

[139] Kyuyoung Heo, Jinhwan Yoon, Kyeong Sik Jin, Sangwoo Jin, Harumi Sato, Yukihiro Ozaki, Michael M. Satkowski, Isao Noda, and Moonhor Ree. Structural evolution in microbial polyesters. *The Journal of Physical Chemistry B*, 112(15):4571–4582, 2008.

[140] Toan Van Nguyen, Toshiteru Nagata, Kosei Noso, Kenshiro Kaji, Hiroyasu Masunaga, Taiki Hoshino, Takaaki Hikima, Shinichi Sakurai, Kenta Yamamoto, Yuta Miura, Takashi Aoki, Hideki Yamane, and Sono Sasaki. Effect of the 3-hydroxyhexanoate content on melt-isothermal crystallization behavior of microbial poly(3-hydroxybutyrate-co-3-hydroxyhexanoate). *Macromolecules*, 54(18):8738–8750, 2021.

[141] Hsiu-Jung Chiu and Jiang-Wen You. Lamellar morphology of poly(3-hydroxybutyrate)/poly(ethylene oxide) blends as studied via small angle x-ray scattering. *Journal of Polymer Research*, 10(2):79–85, 2003.

[142] Zhijie Xia, Haoyuan Zhao, Yusong Wang, Yiming Ma, Xiaoliang Wang, Lingpu Meng, Daoliang Wang, Junfang Sheng, and Wei Chen. Chain dynamics and crystalline network structure of poly[r-3-hydroxybutyrate-co-4-hydroxybutyrate] as revealed by solid-state nmr. *Soft Matter*, 17(15):4195–4203, 2021.

[143] C. R. Deeken, D. C. Chen, M. Lopez-Cano, D. P. Martin, and A. Badhwar. Fully resorbable poly-4-hydroxybutyrate (p4hb) mesh for soft tissue repair and reconstruction: A scoping review. *Front Surg*, 10:1157661, 2023.

[144] K. N. Houk, Arash Jabbari, H. K. Hall, and Carlos Alemán. Why δ-valerolactone polymerizes and γ-butyrolactone does not. *The Journal of Organic Chemistry*, 73(7):2674–2678, 2008.

[145] David P. Martin and Simon F. Williams. Medical applications of poly-4-hydroxybutyrate: a strong flexible absorbable biomaterial. *Biochemical Engineering Journal*, 16(2):97–105, 2003.

[146] Luciano F. Boesel, Sylvaine Le Meur, Linda Thöny-Meyer, and Qun Ren. The effect of molecular weight on the material properties of biosynthesized poly(4-hydroxybutyrate). *International Journal of Biological Macromolecules*, 71:124–130, 2014.

[147] S. L. Sendelbeck and C. L. Girdis. Disposition of a 14c-labeled bioerodible polyorthoester and its hydrolysis products, 4-hydroxybutyrate and cis,trans-

1,4-bis(hydroxymethyl)cyclohexane, in rats. *Drug Metab Dispos*, 13(3):291–5, 1985.

[148] Xinyu Mu, Lin Yang, Yong Shen, Zhenbo Ning, Ni Jiang, Zhibo Li, and Zhihua Gan. Distinct degradation behaviors of semi-crystalline poly (4-hydroxybutyrate) containing a nucleating agent under enzymatic or alkaline conditions. *Polymer Degradation and Stability*, 203, 2022.

[149] Fengyu Su, Tadahisa Iwata, Kumar Sudesh, and Yoshiharu Doi. Electron and x-ray diffraction study on poly(4-hydroxybutyrate). *Polymer*, 42(21):8915–8918, 2001.

[150] I. Keridou, L. J. Del Valle, L. Funk, P. Turon, L. Franco, and J. Puiggali. Non-isothermal crystallization kinetics of poly(4-hydroxybutyrate) biopolymer. *Molecules*, 24(15):2840+, 2019.

[151] I. Keridou, L. J. Del Valle, L. Funk, P. Turon, I. Yousef, L. Franco, and J. Puiggali. Isothermal crystallization kinetics of poly(4-hydroxybutyrate) biopolymer. *Materials (Basel)*, 12(15):2488+, 2019.

[152] Madeleine Aubin and Robert E. Prud'homme. Preparation and properties of poly(valerolactone). *Polymer*, 22(9):1223–1226, 1981.

[153] Yukiko Furuhashi, Pawel Sikorski, Edward Atkins, Tadahisa Iwata, and Yoshiharu Doi. Structure and morphology of the aliphatic polyester poly(?-valerolactone) in solution-grown, chain-folded lamellar crystals. *Journal of Polymer Science Part B: Polymer Physics*, 39(21):2622–2634, 2001.

[154] A. A. Yevstropov, B. V. Lebedev, T. G. Kulagina, and N. K. Lebedev. The calorimetric study in the 13·8–340°k range of δ-valerolactone, its polymer, and of the δ-valerolactone polymerization. *Polymer Science U.S.S.R.*, 24(3):628–636, 1982.

[155] Maria L. Focarete, Mariastella Scandola, Ajay Kumar, and Richard A. Gross. Physical characterization of poly(?-pentadecalactone) synthesized by lipase-catalyzed ring-opening polymerization. *Journal of Polymer Science Part B: Polymer Physics*, 39(15):1721–1729, 2001.

[156] Jorge Fernandez, Agustin Etxeberria, Aitor Larrañaga Varga, and Jose-Ramon Sarasua. Synthesis and characterization of ω-pentadecalactone-co-ϵ-decalactone copolymers: Evaluation of thermal, mechanical and biodegradation properties. *Polymer*, 81:12–22, 2015.

[157] Jiali Cai, Chen Liu, Minmin Cai, Jie Zhu, Feng Zuo, Benjamin S. Hsiao, and Richard A. Gross. Effects of molecular weight on poly(ω-pentadecalactone) mechanical and thermal properties. *Polymer*, 51(5):1088–1099, 2010.

[158] Massimo Gazzano, Viscardo Malta, Maria Letizia Focarete, Mariastella Scandola, and Richard A. Gross. Crystal structure of poly(ω-pentadecalactone). *Journal of Polymer Science Part B: Polymer Physics*, 41(10):1009–1013, 2003.

[159] G.T. Davis, R.K. Eby, and J.P. Colson. Thermal expansion of polyethylene unit cell - effect of lamella thickness. *Journal of Applied Physics*, 41(11):4316–4326, 1970.

[160] Jiali Cai, Benjamin S Hsiao, and Richard A Gross. Polypentadecalactone prepared by lipase catalysis: crystallization kinetics and morphology. *Polymer International*, 58(8):944–953, 2009.

[161] P. Skoglund and Å Fransson. Thermophysical properties of polypentadecanolactone. *Polymer*, 39(10):1899–1906, 1998.

[162] Boris Lebedev and Alexei Yevstropov. Thermodynamic properties of polylactones. *Die Makromolekulare Chemie*, 185(6):1235–1253, 1984.

[163] Massimiliano Barletta, Clizia Aversa, Muhammad Ayyoob, Annamaria Gisario, Kotiba Hamad, Mehrshad Mehrpouya, and Henri Vahabi. Poly(butylene succinate) (pbs): Materials, processing, and industrial applications. *Progress in Polymer Science*, 132:101579, 2022.

[164] Nicolas Jacquel, Floriane Freyermouth, Françoise Fenouillot, Alain Rousseau, Jean Pierre Pascault, Patrick Fuertes, and René Saint-Loup. Synthesis and properties of poly(butylene succinate): Efficiency of different transesterification catalysts. *Journal of Polymer Science Part A: Polymer Chemistry*, 49(24):5301–5312, 2011.

[165] Tao Zhao, Jinshuo Yu, Xingyang zhang, Wenshuang Han, Shuo zhang, Hongwei Pan, Qingxin Zhang, Xiaoyan Yu, Junjia Bian, and Huiliang Zhang. Thermal, crystallization, and mechanical properties of polylactic acid (pla)/poly(butylene succinate) (pbs) blends. *Polymer Bulletin*, 2023.

[166] Andrew Anstey, Sudhakar Muniyasamy, Murali M. Reddy, Manjusri Misra, and Amar Mohanty. Processability and biodegradability evaluation of composites from poly(butylene succinate) (pbs) bioplastic and biofuel co-products from ontario. *Journal of Polymers and the Environment*, 22(2):209–218, 2014.

[167] Yasushi Ichikawa, Junichiro Washiyama, Yoshihiro Moteki, Keiichi Noguchi, and Kenji Okuyama. Crystal transition mechanisms in poly(tetramethylene succinate). *Polymer Journal*, 27(12):1230–1238, 1995.

[168] G.M. Liu, L.C. Zheng, X.Q. Zhang, C.C. Li, S.C. Jiang, and D.J. Wang. Reversible lamellar thickening induced by crystal transition in poly(butylene succinate). *Macromolecules*, 45(13):5487–5493, 2012.

[169] K. J. Ihn, E. S. Yoo, and S. S. Im. Structure and morphology of poly(tetramethylene succinate) crystals. *Macromolecules*, 28(7):2460–2464, 1995.

[170] Tadakazu Miyata and Toru Masuko. Crystallization behaviour of poly(tetramethylene succinate). *Polymer*, 39(6-7):1399–1404, 1998.

[171] George Z. Papageorgiou and Dimitris N. Bikiaris. Crystallization and melting behavior of three biodegradable poly(alkylene succinates). a comparative study. *Polymer*, 46(26):12081–12092, 2005.

[172] Xiaohong Wang, Jianjun Zhou, and Lin Li. Multiple melting behavior of poly(butylene succinate). *European Polymer Journal*, 43(8):3163–3170, 2007.

[173] J. Xu, B. Heck, H.M. Ye, J. Jiang, Y.R. Tang, J. Liu, B.H. Guo, R. Reiter, D.S. Zhou, and G. Reiter. Stabilization of nuclei of lamellar polymer crystals: Insights from a comparison of the hoffman-weeks line with the crystallization line. *Macromolecules*, 49(6):2206–2215, 2016.

[174] E. S. Yoo and S. S. Im. Melting behavior of poly(butylene succinate) during heating scan by dsc. *Journal of Polymer Science Part B: Polymer Physics*, 37(13):1357–1366, 1999.

[175] Christoph Schick, Akihiko Toda, and René Androsch. The narrow thickness distribution of lamellae of poly(butylene succinate) formed at low melt supercooling. *Macromolecules*, 54(7):3366–3376, 2021.

[176] Martha Schulz, Anne Seidlitz, Albrecht Petzold, and Thomas Thurn-Albrecht. The effect of intracrystalline chain dynamics on melting and reorganization during heating in semicrystalline polymers. *Polymer*, 196:122441, 2020.

[177] Jun Xu and Bao-Hua Guo. *Microbial Succinic Acid, Its Polymer Poly(butylene succinate), and Applications*, volume 14 of *Microbiology Monographs*, pages 347–388. Springer Berlin Heidelberg, Berlin, Heidelberg, 2010.

[178] Rajendran Muthuraj, Manjusri Misra, and Amar Kumar Mohanty. Biodegradable compatibilized polymer blends for packaging applications: A literature review. *Journal of Applied Polymer Science*, 135(24):45726, 2018.

[179] Oluranti Agboola, Rotimi Sadiku, Touhami Mokrani, Ismael Amer, and Odunayo Imoru. *4 - Polyolefins and the environment*, pages 89–133. Woodhead Publishing, 2017.

[180] Z. Zhai, C. Fusco, J. Morthomas, M. Perez, and O. Lame. Disentangling and lamellar thickening of linear polymers during crystallization: Simulation of bimodal and unimodal molecular weight distribution systems. *ACS Nano*, 13(10):11310–11319, 2019.

[181] Yoshito Otake, Tomoko Kobayashi, Hitoshi Asabe, Nobunao Murakami, and Katsumichi Ono. Biodegradation of low-density polyethylene, polystyrene, polyvinyl chloride, and urea formaldehyde resin buried under soil for over 32 years. *Journal of Applied Polymer Science*, 56(13):1789–1796, 1995.

[182] K. Schäler, A. Achilles, R. Bärenwald, C. Hackel, and K. Saalwächter. Dynamics in crystallites of poly(e-caprolactone) as investigated by solid-state nmr. *Macromolecules*, 46(19):7818–7825, 2013.

[183] Munehisa Yasuniwa, Shinsuke Tsubakihara, Tadashi Satou, and Koji Iura. Multiple melting behavior of poly(butylene succinate). ii. thermal analysis of isothermal crystallization and melting process. *Journal of Polymer Science Part B: Polymer Physics*, 43(15):2039–2047, 2005.

[184] D. W. Van Krevelen and K. te Nijenhuis. *Properties of Polymers: Their Correlation with Chemical Structure; Their Numerical Estimation and Prediction from Additive Group Contributions.* Elsevier Science & Technology, Oxford, 4. edition, 2009.

[185] M. A. Kennedy, A. J. Peacock, and L. Mandelkern. Tensile properties of crystalline polymers - linear polyethylene. *Macromolecules*, 27(19):5297–5310, 1994.

[186] Maria Laura Di Lorenzo, René Androsch, and Maria Cristina Righetti. Low-temperature crystallization of poly(butylene succinate). *European Polymer Journal*, 94:384–391, 2017.

[187] Christoph Schick and René Androsch. The origin of annealing peaks in semicrystalline polymers: Enthalpy recovery or melting? *Macromolecules*, 53(20):8751–8756, 2020.

[188] Takashi Fujimaki. Processability and properties of aliphatic polyesters, 'bionolle', synthesized by polycondensation reaction. *Polymer Degradation and Stability*, 59(1):209–214, 1998.

[189] Mareen Schäfer, Shichen Yuan, Albrecht Petzold, Ricardo A. Pérez-Camargo, Alejandro J. Müller, Thomas Thurn-Albrecht, Kay Saalwächter, and Klaus Schmidt-Rohr. Asymmetric co-unit inclusion in statistical copolyesters. *Macromolecules*, 54(2):835–845, 2021.

[190] G.R. Strobl. A new method for evaluating slit-smeared small angle x-ray scattering data. *Acta Crystallographica Section A-Crystal Physics Diffraction Theoretical and General Crystallography*, A 26:367–375, 1970.

[191] W. Ruland. The evaluation of the small-angle scattering of lamellar two-phase systems by means of interface distribution functions. *Colloid and Polymer Science*, 255(5):417–427, 1977.

[192] David A. Gregory, Caroline S. Taylor, Annabelle T. R. Fricker, Emmanuel Asare, Santosh S. V. Tetali, John W. Haycock, and Ipsita Roy. Polyhydroxyalkanoates and their advances for biomedical applications. *Trends in Molecular Medicine*, 28(4):331–342, 2022.

[193] Demetres Briassoulis, Ioanna-Georgia Athanasoulia, and Philippos Tserotas. Phb/pla plasticized by olive oil and carvacrol solvent-cast films with optimised ductility and physical ageing stability. *Polymer Degradation and Stability*, 200:109958, 2022.

[194] Rudolf Hufenus, Felix A. Reifler, María P. Fernández-Ronco, and Manfred Heuberger. Molecular orientation in melt-spun poly(3-hydroxybutyrate) fibers: Effect of additives, drawing and stress-annealing. *European Polymer Journal*, 71:12–26, 2015.

[195] Taku Omura, Tatsuya Goto, Akira Maehara, Satoshi Kimura, Hideki Abe, and Tadahisa Iwata. Thermal degradation behavior of poly[(r)-3-hydroxybutyrate-co-4-hydroxybutyrate]. *Polymer Degradation and Stability*, 183:109460, 2021.

[196] A. El-Hadi, R. Schnabel, E. Straube, G. Müller, and S. Henning. Correlation between degree of crystallinity, morphology, glass temperature, mechanical properties and biodegradation of poly (3-hydroxyalkanoate) phas and their blends. *Polymer Testing*, 21(6):665–674, 2002.

[197] Yuxian An, Lisong Dong, Guang Li, Zhishen Mo, and Zhiliu Feng. Miscibility, crystallization kinetics, and morphology of poly(β-hydroxybutyrate) and poly(methyl acrylate) blends. *Journal of Polymer Science Part B: Polymer Physics*, 38(14):1860–1867, 2000.

[198] H. Verhoogt, B. A. Ramsay, and B. D. Favis. Polymer blends containing poly(3-hydroxyalkanoate)s. *Polymer*, 35(24):5155–5169, 1994.

[199] Yuxian An, Lixia Li, Lisong Dong, Zhishen Mo, and Zhiliu Feng. Non-isothermal crystallization and melting behavior of poly(β-hydroxybutyrate)–poly(vinyl-acetate) blends. *Journal of Polymer Science Part B: Polymer Physics*, 37(5):443–450, 1999.

[200] Jae Shin Choi and Won Ho Park. Effect of biodegradable plasticizers on thermal and mechanical properties of poly(3-hydroxybutyrate). *Polymer Testing*, 23(4):455–460, 2004.

[201] Richard J. Pazur, Philippa J. Hocking, Stéphane Raymond, and Robert H. Marchessault. Crystal structure of syndiotactic poly(β-hydroxybutyrate) from x-ray fiber and powder diffraction analyses and molecular modeling. *Macromolecules*, 31(19):6585–6592, 1998.

[202] B. M. Fung, A. K. Khitrin, and Konstantin Ermolaev. An improved broad-band decoupling sequence for liquid crystals and solids. *Journal of Magnetic Resonance*, 142(1):97–101, 2000.

[203] R. Bärenwald, Y. Champouret, K. Saalwächter, and K. Schäler. Correction to "determination of chain flip rates in poly(ethylene) crystallites by solid-state low-field 1h nmr for two different sample morphologies". *The Journal of Physical Chemistry B*, 118(43):12575–12576, 2014.

[204] Richard H. Boyd. Relaxation processes in crystalline polymers: experimental behaviour - a review. *Polymer*, 26(3):323–347, 1985.

[205] Guo-Qiang Chen. Production and applications of microbial polyhydroxyalka-noates. In Emo Chiellini and Roberto Solaro, editors, *Biodegradable Polymers and Plastics*, pages 155–166. Springer US.

[206] Camila Utsunomia, Qun Ren, and Manfred Zinn. Poly(4-hydroxybutyrate): Current state and perspectives. *Frontiers in Bioengineering and Biotechnology*, 8, 2020.

[207] Katalee Jariyavidyanont, Qiang Yu, Albrecht Petzold, Thomas Thurn-Albrecht, Rainer Glüge, Holm Altenbach, and René Androsch. Young's modulus of the different crystalline phases of poly (l-lactic acid). *Journal of the Mechanical Behavior of Biomedical Materials*, 137:105546, 2023.

[208] J. Puiggali, Y. Ikada, H. Tsuji, L. Cartier, T. Okihara, and B. Lotz. The frustrated structure of poly(l-lactide). *Polymer*, 41(25):8921–8930, 2000.

[209] Otto Vogl and Gary D. Jaycox. Helical polymers. *Polymer*, 28(13):2179–2182, 1987.

[210] B. Lotz, S. Graff, C. Straupe, and J.C. Wittmann. Single-crystals of gamma-phase isotactic polypropylene - combined diffraction and morphological support for a structure with nonparallel chains. *Polymer*, 32(16):2902–2910, 1991.

[211] Jesmy Jose, Ghazaleh Pourfallah, Alcides Lopes Leao, and Suresh S. Narine. Influence of monomeric and polymeric structure on the physical properties of thermoplastic polyesters derived from hydroxy fatty acids. *Polymer International*, 63(11):1902–1911, 2014.

[212] Mark P. F. Pepels, Michael Ryan Hansen, Han Goossens, and Rob Duchateau. From polyethylene to polyester: Influence of ester groups on the physical properties. *Macromolecules*, 46(19):7668–7677, 2013.

[213] E.W. Fischer. Zusammenhänge zwischen der kolloidstruktur kristalliner hochpolymerer und ihrem schmelz- und rekristallisationsverhalten. *Kolloid-Zeitschrift and Zeitschrift fur Polymere*, 231(1-2):458–503, 1969.

[214] Hervé Marand and Zhenyu Huang. Isothermal lamellar thickening in linear polyethylene: correlation between the evolution of the degree of crystallinity and the melting temperature. *Macromolecules*, 37(17):6492–6497, 2004.

[215] Anna Malafronte, Miriam Scoti, Maria Rosaria Caputo, Bo Li, Rachel K. O' Reilly, Andrew P. Dove, Alejandro J. Müller, and Claudio De Rosa. Crystal structure of poly(7-heptalactone). *Macromolecules*, 56(11):4153–4162, 2023.

[216] Yukiko Furuhashi, Tadahisa Iwata, Pawel Sikorski, Edward Atkins, and Yoshiharu Doi. Structure and morphology of the aliphatic polyester poly-β-propiolactone in solution-grown chain-folded lamellar crystals. *Macromolecules*, 33(25):9423–9431, 2000.

[217] Buckley Crist. Thermodynamics of statistical copolymer melting. *Polymer*, 44(16):4563–4572, 2003.

Publications

1. K. Jariyavidyanont, M. Du, Q. Yu, T. Thurn-Albrecht, C. Schick, R. Androsch. Bulk Enthalpy of Melting of Poly (l-lactic acid) (PLLA) Determined by Fast Scanning Chip Calorimetry, *Macromol. Rapid Commun.*: 2200148, 2022

2. K. Jariyavidyanont, R. Zhang, Q. Yu, A. Janke, T. Thurn-Albrecht, C. Schick, R. Androsch. Formation of imperfect crystals in poly(ϵ-caprolactone) at high melt-supercooling, *Materials Letters*: 324, 132704, 2022

3. K. Jariyavidyanont, Q. Yu, A. Petzold, T. Thurn-Albrecht, R. Glüge, H. Altenbach, R. Androsch. Youngs's modulus of the different crystalline phases of poly (L-lactic acid). *Journal of the Mechanical Behavior of Biomedical Materials*: 137, 105546, 2023

4. Q. Yu, A. Anuar, A. Petzold, J. Balko, K. Saalwächter, and T. Thurn-Albrecht. The semicrystalline morphology of polybutylene succinate supports a general scheme based on intracrystalline dynamics. *Macromolecular Chemistry and Physics*: 2200459, 2023.

5. K. Jariyavidyanont, A. Janke, Q. Yu, T. Thurn-Albrecht, R. Androsch. Lamellar Morphology of Disorder α'-Crystals of Poly(L-Lactic Acid). *Crystal Growth & Design*: 24 (4), 1825-1834, 2024

6. A. Anuar, Q. Yu, K. Jariyavidyanont, A. Petzold, R. Androsch, T. Thurn-Albrecht, K. Saalwächter. Poly-3-hydroxybutyrate, a Crystal-Mobile Biodegradable Polyester, *Macromolecules*: recently published, 2024

Erklärung

Hiermit versichere ich, dass ich die vorliegende Arbeit selbständig und ohne Benutzung anderer als der im beigefügten Literaturverzeichnis angegebenen Hilfsmittel angefertigt habe. Alle Stellen, die wörtlich oder sinngemäß aus Veröffentlichungen entnommen wurden, sind als solche kenntlich gemacht.
Ferner habe ich nicht versucht, anderweitig mit oder ohne Erfolg eine Dissertation einzureichen oder mich einer Doktorprüfung zu unterziehen.

Halle (Saale), 26. August 2024

_____   _____
Ort, Datum   Unterschrift

Curriculum vitae

Personal data

Name:	Qiang Yu
Nationality:	Chinese

Education

2002/09-2006/07	Bachelor of Engineering (Polymer science and engineering)
	East China University of Science and Technology
	Shanghai, China
2008/10-2011/03	Master of Science (Applied Polymer Science)
	Martin Luther University Halle-Wittenberg
	Halle (Saale), Germany
Since 2020/02	Ph.D at Institute of Physics
	Martin Luther University Halle-Wittenberg
	(Supervised by Prof. Dr. Thomas Thurn-Albrecht)
	Halle (Saale), Germany

Working Experience

2006/07-2008/09	R&D: Lab engineer (Polymer characterization)
	Shanghai Daikin air conditioning Co., Ltd.
2011/09-2014/05	R&D: Research engineer (Thermoplastic elastomer & Silicone)
	Saint-Gobain Research (Shanghai)
2014/06-2017/04	R&D: Research scientist/lab manager (Fluorinated elastomer)
	Solvay (China) Specialty Polymer
2017/05-2020/01	R&D: Senior application scientist/lab manager (Elastomer)
	Cabot (China) Limited

There are no previous convictions and no preliminary investigation has been initiated.

Halle (Saale), 26. August 2024

_____   _____

Ort, Datum   Unterschrift

Achknowledgement

I would like to express my sincere gratitude to my supervisor, Prof. Dr. Thomas Thurn-Albrecht, for providing me the opportunity to work on this project and taking me in at the beginning (2020. Feb.) of the outbreak of COVID-19 in China. I appreciate all his guidance, advice and patience throughout my PhD. His passion and seriousness for science and education inspired me during my PhD and will influence my future career. I am very grateful to Dr. Albrecht Petzold for his instrumental assistance and numerous scientific discussions, from which I gained a lot.

It is also my pleasure to have the cooperation and help from my colleagues on this project. I want to thank Afiq Anuar for his expertise in the field of NMR and the numerous discussions for me to better understand NMR techniques. I also would like to thank Dr. Katalee Jariyavidyanont for the creative ideas for sample preparation, mechanical measurements and many fruitful scientific discussions.

In addition, it is my honor to receive assistance and cooperation from the students who have worked with me on a small project or written a thesis on several subtopics of this project. I would like to thank Aaron Miller (RISE project) for his contribution to the investigation of PVL. I am very grateful to Lea Ringelhan (Bachelor thesis on PE with carbonyl groups), who has been very tolerant of my German skills. I would also like to thank Sharifa Abdullaeva (Master thesis on the characterization of P4HB and PE) and Venkata Sss Naresh Vulchi (Lab project on the crystallization of PLLA).

This project involves a wide range of techniques and instruments. It was lucky for me to receive a lot of detailed introductions, instructions and experience from my colleagues. I would like to thank Dr. Martha Schulz for the introduction of theoretical and hands-on knowledge of many experimental techniques (Kratky camera, flash DSC, rheometer, etc.) and for helping me to get on track with the project. I really appreciate the introduction of microfocus instrument by Robert Kahl, and I am grateful for his IT assistance (including pigeons desktop) and trouble shooting of the software of Kratky camera. I thank Dr. Oleksandr Dolynchuk for the introduction and guidance on the use of the diffractometer. I am thankful to Marthinus Van Niekerk for the introduction of polarized optical microscope. I am thankful to Katrin Herfurt for the DSC measurements. I would also like to thank Dr. Mareen Schäfer for the introduction of the NMR minispec and its data analysis. I am very grateful to all my current and former colleagues in the Experimental Polymer Physics group for creating such a friendly atmosphere. I would like to say thank you to Dr.

Klaus Schröter, Albrecht Petzold, Oleksandr Dolnchuk, Dr. Rose Mary Michell Uribe, Robert Kahl, Martha Schulz, Dr. Tariq Muhammad, Dr. Jens Balko, Marthinus Van Niekerk, Tonghua Liu, Katrin Herfurt, Tina Bourguignon, Chanel Krebs, Alexander Much, Johann Holz and Anton Sinner. Special thanks go to Ann-Kristin Flieger, who helped me with all my administrative things upon my arrival, provided guidance for the planning of the project and organized useful workshop to improve soft skills.

I thank Prof. Dr. Kay Saalwächter for being my mentor. I really appreciate his time for our regular meetings about the progress of the project, his presence at the project meetings, his scientific advice and his support of this project. I am also thankful to Prof. Dr. René Androsch for providing me with critical scientific instruments for measurements, the cooperation with regular project meetings and scientific papers.

I would like to thank Ann-Kristin Flieger, Afiq Anuar, Markus Flieger, Samira Stahmann and Rose Mary Michell Uribe for proofreading my dissertation.

At last I would like to thank my family. I would like to say Xie Xie to my parents, Yu Duyi and Mi Shufen, for their strong support. Thank you for your understanding that I was not there for you during the pandemic.